Alma Mater Studiorum - Università di Bologna

DOTTORATO DI RICERCA IN

MECCANICA E SCIENZE AVANZATE DELL'INGEGNERIA

Ciclo 35

Settore Concorsuale: 09/A1 - INGEGNERIA AERONAUTICA, AEROSPAZIALE E NAVALE

Settore Scientifico Disciplinare: ING-IND/05 - IMPIANTI E SISTEMI AEROSPAZIALI

DEEP AND NEAR SPACE TRACKING STATIONS IN SUPPORT OF LUNAR AND PLANETARY EXPLORATION MISSIONS

Presentata da: Andrea Togni

Coordinatore Dottorato

Lorenzo Donati

Supervisore

Paolo Tortora

Co-supervisore

Marco Zannoni

Esame finale anno 2023

Author's Note

This thesis is continuously revised to correct all typos that are found during a never-ending revision process. To obtain the most updated version, please feel free to contact the author by sending an e-mail to: `andrea.togni3@unibo.it`.

Summary

The aim of this dissertation is to describe the methodologies required to design, operate, and validate the performance of ground stations dedicated to near and deep space tracking, as well as the models developed to process the signals acquired, from raw data to the output parameters of the orbit determination of spacecraft. In particular, the main focus is given to the employment of accurate dynamical models to evaluate the performance and tracking accuracy of ground stations.

Chapter 1 outlines the topic of orbit determination, the impact of ground stations as both radio science and navigation instruments, and the mechanical and radio-frequency architectures usually employed to make precision tracking activities possible. In particular, as space missions become more accessible to scientists thanks to the miniaturization of payloads and spacecraft, also the development and validation of the ground segments has seen an increase in interest. In this context, the load on the currently active deep space networks is substantial, paving the way for the addition of tracking capabilities to stations originally developed solely for radio-astronomy investigations. Nonetheless, this conversion - and subsequent affiliation to tracking networks - requires the development of validated testing routines for the achievable capabilities and tracking accuracies of said stations. In consideration of this, an overview on the topic is provided, with an analysis of the requirements and architectures of ground stations, how downlink signals are handled before reaching the receiver, and finally how the required observables are generated to complete the orbit determination process.

Chapter 2 describes the theory behind the radio-frequency signals received at the stations, and the processing routines applied to the downlink signals after their digitalization in the receiver. In this chapter, the procedures developed to address the non-linearities and issues usually encountered when performing parametric estimation of stochastic signals are highlighted, with a focus on the generation of radiometric observables for deep space tracking. In particular, this processing is concerned with the estimation and pre-calibration of signal delays introduced by the transmission channels, as a function of the downlink frequency and the thermodynamical parameters of the media the signal passes through during the tracking activities. Raw data are collected and processed to generate the observables, which are the quantities observed at the transmitter and dependent on the trajectories of the target spacecraft and the ground station itself. As these observables are usually the only way of estimating the orbit and the environment in which the spacecraft is navigating, the analysis of the performance, accuracy, and limitations of current estimation methods is discussed, an accurate estimating algorithm is proposed, and models

are introduced to quantify its performance and fitness for radiometric applications.

Chapter 3 presents the acquisition campaign and performance-testing routines implemented for the Italian Space Agency's ASI ground station Sardinia Deep Space Antenna SDSA, affiliated node DSS-69 of the NASA Deep Space Network DSN. SDSA has been employed in several tracking activities since its technical commissioning in 2018, but its radiometric tracking performance has never been fully evaluated when communicating with a spacecraft operating in deep space, or compared to similar deep space antennas. From December 2020 to June 2021, an acquisition campaign of radiometric tracking data has been performed with the objective of testing the station. In this timeframe, SDSA has been systematically tracking the NASA spacecraft Juno at X-band in a three-way configuration, with the uplink signal provided by the Madrid Deep Space Communication Complex Deep Space Communication Complex (DSCC) in Spain. Thanks to the SDSA back end, borrowed from the European Space Agency ESA and installed in a shielded environment, the station was able to record both closed-loop and open-loop data for further processing and comparison. In particular, the same radiometric data was recorded simultaneously in a two-way configuration at the NASA stations, and so it was possible to estimate the noise sources common to both signal paths and isolate the SDSA station contributions to the uncertainties in the Doppler measurements of the spacecraft Juno. To provide nominal values for the antenna performance and compare different operational settings of the ground complex subsystems, Caltech/JPL's orbit determination toolkit MONTE was used to fit the Doppler observables to an accurate dynamical model. The fit residuals were then investigated to obtain stability and performance metrics to evaluate the antenna noise contributions. In this chapter, the results of the tracking activities of the Juno spacecraft with SDSA are presented. The effects on the tracking performance of different antenna sub-systems settings are also discussed, showing the contribution of the active surface control and the pointing strategy to the stability of the Doppler residuals. Additionally, an error budget for Doppler tracking with SDSA is presented and discussed. This model was developed using radiometric tracking data with different mission geometries and transmission paths, and makes it possible to estimate the contribution to the Doppler tracking uncertainties from the antenna hardware. Lastly, the changes in the Doppler residuals are studied to make a general model of the station's frequency stability as a function of time, and an evaluation of the difference in tracking accuracy between SDSA and the NASA antennas of the Madrid complex during the same tracking arcs is presented.

Chapter 4 describes the work performed on the Morehead State University's ground station with a 21-m diameter dish, also known as DSN affiliate node DSS-17. Since this station can only track with a closed-loop receiver and does not store data for later processing, a technical solution is designed and presented to implement an open-loop receiver. In particular, such receiver makes it possible not to lose important data where other means of tracking the downlink signal would fail due to variations in the signal power, strong uncalibrated delays, or unexpected variations in the signal frequency content. Additionally, a very preliminary overview of the tracking performance of DSS-17 is presented using some

of the radiometric measurements from the initial activities of the CAPSTONE spacecraft, which is currently operating in the cislunar space.

Acknowledgements

This dissertation is the product of years of work that required commitment and sacrifices, and none of it would have been possible without the guidance of my mentors Paolo Tortora and Marco Zannoni. I want to thank first of all the team of the Radio Science and Planetary Exploration Laboratory of University of Bologna. Together, we've spent years working side-by-side on deep space missions, discussing methodologies, results, and supporting each other during the difficult times we had to face together. I'm also grateful to the members of the Italian Space Agency working on the Sardinia Deep Space Antenna for these years of fruitful collaboration, during which we shared knowledge and ideas to work together to improve the capabilities of the first Italian deep space antenna. Finally, I need to mention the team of the Space Science Center at the Morehead State University, who welcomed me to Kentucky as a friend and colleague, and with whom I shared incredibly enriching experiences.

Acronyms

AMC	Active Multicoupler
AMPL	Amplifier
ASI	Italian Space Agency
AWGN	Additive White Gaussian Noise
AWVR	Advanced Water Vapor Radiometer
BWG	Beam Waveguide
Caltech	California Institute of Technology
CAPSTONE	Cislunar Autonomous Positioning System Technology Operations and Navigation Experiment
CAWGN	Complex Additive White Gaussian Noise
COTS	Commercial off-the-shelf
CRLB	Cramér-Rao Lower Bound
D.S.	Deep Space
DFT	Discrete Fourier Transform
DISCOS	Development of the Italian Single-dish COntrol System
DSA	Deep Space Antenna
DSCC	Deep Space Communication Complex
DSN	Deep Space Network
DSOC	Deep Space Operation Center
DSS	Deep Space Station
DTFT	Discrete-Time Fourier Transform
DTT	Downlink, Tracking, & Telemetry
EDL	Entry, Descent, and Landing
EDSN	ESA Deep Space Network
EME 2000	Earth Mean Equation at J2000
ESA	European Space Agency
ESOC	European Space Operations Center

ESTRACK	European Space Tracking
FFT	Fast Fourier Transform
FI	Instantaneous Frequency
FOT	Fiber Optic Transmission
FT	Fourier Transform
FTS	Frequency and Timing Subsystem
G/T	Gain-to-Noise-Temperature
GNSS	Global Navigation Satellite System
GRACE	Gravity Recovery and Climate Experiment
HEF	High Efficiency
IDC	IF-to-Digital Converter
IF	Intermediate Frequency
IFMS	Intermediate Frequency and Modem System
IFT	Inverse Fourier Transform
INAF	Italian National Institute of Astrophysics
IOD	Initial Orbit Determination
JPL	Jet Propulsion Laboratory
LER	Lower Equipment Room
LNA	Low-Noise Amplifier
MLE	Maximum Likelihood Estimator
MOC	Mission Operation Center
MONTE	Mission-analysis and Operations Navigation Toolkit Environment
MSE	Mean-Square-Error
MSU	Morehead State University
NASA	National Aeronautics and Space Administration
NPS	Normalized Power Spectrum
OD	Orbit Determination
OLR	Open-Loop Receiver
PDT	Payload Data Transmission
PLL	Phase-Locked Loop
PS	Power Spectrum
RF	Radio-Frequency
RID	RF-to-IF Down-Converter
RMS	Root-Mean-Square

RMSE	Root-Mean-Square-Error
RSR	Radio-Science Recevier
RTLT	Round-Trip Light-Time
RV	Random Variable
SDR	Software Defined Radio
SDSA	Sardinia Deep Space Antenna
SEP	Sun-Earth-Probe
SNR	Signal-to-Noise Ratio
SOD	Statistical Orbit Determination
SPC	Signal Processing Center
SPI	Successive Parabolic Interpolation
SQNR	Signal-to-Quantization-Noise Ratio
SRA	Sequential Ranging Assembly
SRP	Solar Radiation Pressure
STEREO-A	Solar Terrestrial Relations Observatory - A
STFT	Short-Time Fourier Transform
TC	Telecommands
TCM	Trajectory Correction Maneuvers
TDCS	Tropospheric Delay Calibration System
TFD	Time-Frequency Distribution
TFR	Time-Frequency Representation
TM	Telemetry
TOPEX	Ocean Topography Experiment
TTC	Tracking, Telemetry, and Command
TTCP	Telemetry, Tracking, & Control Processor
TTD	Telemetry Tracking Delivery
UA	Uplink Assembly
UHF	Ultra High Frequency
UPL	Uplink
USO	Ultra-Stable Oscillator
VHF	Very High Frequency
VLBI	Very-Long-Baseline Interferometry
WVD	Wigner-Ville Distribution
ZHD	Zenith Hydrostatic Delay
ZTD	Zenith Total Delay

Contents

Chapter 1

Introduction

Contents

1.1 Dissertation Aim

The aim of this dissertation is to provide a theoretical framework for the designing of testing procedures to validate the performance of ground stations in support of exploration missions in near and deep space. The definition of a repeatable methodology for the evaluation of the performance of ground systems in space tracking is relevant in the context of the expanding number of deep space missions which require TT&C and navigation support. The currently active deep space networks dedicated to tracking activities can see a workload reduction with an increase in affiliated complexes that track spacecraft, but the accuracy of the latter must be experimentally validated to avoid the introduction of low quality data to the navigation and planetary exploration activities, which may affect the overall accuracy of the trajectory reconstruction.

The complexity in the validation of the tracking performance of ground stations arises from the multitude of variables that can affect the telecommunication link, from limitations in the single subsystem's performance and noise introduced by the antenna electromechanical components, to unmodeled spacecraft dynamics and delays in the transmission

path of the signals. In consideration of this, comparison of the performance of tracking systems requires the employment of high quality calibration and dynamical models, accurate knowledge of space weather and orbit geometry, and appropriate evaluation metrics.

This work is framed in the context of lunar and planetary exploration missions by addressing the challenges in receiving and processing radiometric data for radio science investigations and navigation purposes. These challenges include the designing of an appropriate back-end to read, convert and store the antenna voltages, the definition of appropriate methodologies for pre-processing, calibration, and estimation of radiometric data for the extraction of information on the spacecraft state, and the definition and integration of accurate models of the spacecraft dynamics to evaluate the goodness of the recorded signals. Additionally, the experimental design of acquisition strategies to perform direct comparison between ground stations is described and discussed. In particular, the evaluation of the differential performance between stations requires the designing of a dedicated tracking campaign to maximize the overlap of the recorded datasets at the receivers, making it possible to correlate the received signals and isolate the contribution of the ground segment to the noise in the single link. Finally, in support of the methodologies and models presented, results from the validation and design work performed on the Deep Space Network (DSN) affiliated nodes DSS-69 and DSS-17 will also be reported.

1.2 The Orbit Determination Problem

In this section, the fundamental equations and models of astrodynamics will be briefly reviewed to provide the basis for a detailed description of statistical orbit determination using radiometric data. This theoretical framework will then be contextualized in its applications to deep space missions. While the procedures described here are applicable to any mission, most of the results and examples discussed will be taken from interplanetary missions based on radiometric tracking.

The orbit determination process consists of the indirect estimation of the trajectory - or ephemeris - of a target through the observation of the effects of its motion on the received signals at a specific receiver, generally on the ground. From an operational perspective, in the orbit determination (OD) process two subsequent phases can be identified:

- Initial Orbit Determination (IOD): IOD procedures use limited data to provide an initial estimate of the spacecraft trajectory. Such methods are based on the local linearization of the spacecraft orbit and approximations of the orbital parameters. These methods provide position and velocity estimations with uncertainties higher than those obtained by performing statistical orbit determination [Vallado, 2001], but these preliminary results can be used as a starting solution for more accurate estimations.

- Statistical Orbit Determination (SOD): The SOD routines are based on a local expansion of the dynamical system of the spacecraft around a reference trajectory and initial state. The latter can be estimated through IOD procedures or propagation of a previous state of the spacecraft. These methods rely on the minimization of a

cost function to provide the best estimate - in a statistical sense - of the spacecraft trajectory [Schutz et al., 2004]. The estimation accuracies of these algorithms are higher than those of IOD routines, with a larger number of data points and data types available.

With respect to the SOD procedure, the required steps can be described as follows:

- Pre-processing of radiometric data: Generally, raw data are received and converted to voltage on the ground as-is. These often require pre-processing routines to be converted to observables, and calibrated to remove unwanted noise contributions. In this phase, the quality of calibrations can depend on the available measurements and on the type of mission. Noise sources and calibrations will be discussed in more detail in section 1.2.3.
- Generation of radiometric observables from measurements: Once systematic noise contributions are removed from the data, the measurements are processed to generate the associated observables, which are the measurable quantities that contain information on the state of the spacecraft.
- Computation of radiometric observables from models: Through a dynamical model of the spacecraft and the Solar System, the nominal values of the observables are computed for a comparison to the observed one. The computed observables are obtained by integrating the state of the spacecraft using the acceleration contributions of its dynamical model.
- Estimation through nonlinear filtering: Using different methods (generally a batch Kalman filter [Smith et al., 2017]), the parameters of the dynamical model are changed to fit the data and obtain the OD solution.
- Solution analysis: After processing, the quality of the solution is investigated to assess the goodness of the estimated parameters and make decisions for operations on the spacecraft.

1.2.1 Radio-Frequency and Applications

As a spacecraft traverses the Solar System in exploration missions, the transmission link to Earth is guaranteed by using centimeter-wavelength radio signals. The communication is based on a sinusoidal carrier with circular polarization and phase modulation, as frequency variations, mostly due do Doppler effect, preclude the use of frequency modulation. Specifically, the transmitted information can be either imprinted on subcarriers or the signal carrier itself. This differentiation depends on both technical factors and the type of mission. When employed in radio science experiments and navigation activities, radio-frequency transmissions provide communication capabilities to transmit Telecommands (TC) to the spacecraft, receive Telemetry (TM) on the status of the mission, and provide a Payload Data Transmission (PDT) links [Modenini and Ripani, 2022]. Thanks to the variations in the signals associated with the relative motion between the transponders in

the link, these signals can also be employed for navigation or radio science experiments. Table 1.1 reports the frequency bands allocated to deep-space links by the International Telecommunication Union.

Table 1.1: Deep space communication allocated frequency bands [Thornton and Border, 2003].

Band	**Uplink Frequency [MHz]**	**Downlink Frequency [MHz]**
S	2110-2120	2290-2300
X	7145-7190	8400-8450
Ka	34200-34700	31800-32300

As transmissions using the allocated bands permit the modulation of data on carriers at multiple frequencies, so different data rates can be achieved. Additionally, as the wavelength of the radio-frequency signal changes, so does its interaction with the transmission media. Therefore, the choice of one or multiple bands can affect the quality of the transmission when communicating with spacecraft [Asmar, 2022, Bertotti et al., 1993].

For space missions, the navigation process is characterized by the systematic estimation and correction of the trajectory of the spacecraft during the mission. In particular, due to uncertainties in the models and the statistical nature of maneuvers and forces acting on the spacecraft, the orbit determination procedure must be repeated in time to verify the correctness of the applied changes in the attitude and velocity of the spacecraft. As trajectory-correction maneuvers (TCM) are performed, the spacecraft ephemeris is compared to the mission requirements, and the insertion or mission trajectory is finalized [Wood, 2008]. In the end, the objective of the navigation procedures is to make the spacecraft satisfy a target orbit where it can activate its payloads to gather useful data.

Radio science consists in performing estimations and validating hypotheses by analyzing the variations in the characteristics of radiometric measurements. More specifically, these changes can depend on the transmitter and its trajectory, or on the propagation of the signal through a mismodelled path. Missions relying on the first principle study the frequency variations in the transmitted carrier due to the Doppler shift. As this is caused by perturbations in the trajectory of one (or both) the transponders, these can be estimated from the frequency deviations to study planetary interiors, mass/density distributions, non-gravitational accelerations, or relativistic effects [Asmar, 2022, Asmar et al., 2017, Iess et al., 2007]. Investigations based on the second principle are instead concerned with electromagnetic perturbations on the signal after it is transmitted, which in turn are caused by the electromagnetic interactions with the transmission media encountered. These interactions include diffusion, scattering, and reflection from surfaces, signal occultations, or phase advancement due to charged particles [Tortora et al., 2004]. Table 2 provides a general overview of possible investigations performed via the use of radiometric measurements [Asmar, 2022]. In addition to radio science investigations, radio-frequency communication also provides the baseline for orbit determination and navigation procedures [Thornton and Border, 2003]. Fig. 1.2 shows the classification of possible radio science investigations in the two aforementioned categories.

Target [category]	Science products	Observables [radio mode]	Limiting factors
Planetary atmospheres [*Propagation through media*]	• Temperature-pressure profiles • Neutral density • Ionospheric density • Wave properties • Wind velocity • Abundance of key molecules • Shape or equipotential models • Turbulence and scintillation effects • Magnetic fields	• Frequency/ Phase • Amplitude • Polarization • *[One-way or crosslinks]*	• Phase stability • Amplitude stability • Signal-to-noise ratio • Fresnel zone size • Absorption • Geometrical coverage • Temporal density • Orbital accuracy • Multipath interference
Planetary surroundings [*Propagation through media*]	• Ring particle sizes • Ring wave structure • Ring density • Torus electron density • Cometary comae • Planetary ejecta	• Amplitude • Phase • *[One-way]*	• Phase stability • Amplitude stability • Signal-to-noise ratio • Fresnel zone size • Absorption • Geometrical coverage • Temporal density • Orbital accuracy
Solar corona and solar wind [*Propagation through media*]	• Electron density • Turbulence and structures • Coronal ejecta • Coronal and solar wind speed • Scintillation effects • Magnetic fields	• Doppler • Range • Amplitude • Polarization • *[One or two-way]*	• Signal-to-noise ratio • Phase stability • Range calibration
Planetary surfaces [*Scattering off surfaces*]	• Electrical properties • Roughness • Material type • Near-surface layering	• Amplitude • Polarization • Doppler • *[One-way or crosslinks]*	• Signal-to-noise ratio • Geographic resolution • System calibrations • Orbital opportunities

(Continued)

Figure 1.1: Overview of possible radio science targets in deep space, obtainable science products, radiometric observables employed, and investigation limiting factors, part 1. Courtesy of [Asmar, 2022].

Target [category]	Science products	Observables [radio mode]	Limiting factors
Planetary interiors from gravity [*Remote sensing and rotational dynamics/ geodesy*]	• Planetary bulk mass • Mass/density distribution • Interior structure models • Thickness of layers • Libration • Admittance • Gas giants wind patterns • State of the core • Total and core moments of inertia • Tidal response • Natural oscillations • Size and density of core and mantle • Length of day variations • Mass transport/redistribution • Chandler wobble • Ephemeris	• Doppler • Range • *[Two-way or crosslinks]*	• Frequency stability • Unmodeled nongravitational effects • Trajectory design • Orbital accuracy • View geometry • Length of data arcs • Topography/shape/ equipotential models
Fundamental Physics [*Perturbation in spacecraft motion*]	• Gravitational radiation • Relativistic time-delay • Post-Newtonian parameters • Redshift—Equivalence principle	• Doppler • Range • *[Two-way except redshift]*	• Frequency stability • Calibrations
Atmospheric dynamics [*In situ*]	• Wind velocity • Molecular abundance from absorption	• Doppler • *[Crosslinks or one-way]*	• Frequency stability • View geometry
Atmospheric Density [*In situ*]	• Density from drag effects • Cometary mass flux	• Doppler • *[Two-way]*	• Phase stability • Trajectory

Figure 1.2: Overview of possible radio science targets in deep space, obtainable science products, radiometric observables employed, and investigation limiting factors, part 2. Courtesy of [Asmar, 2022].

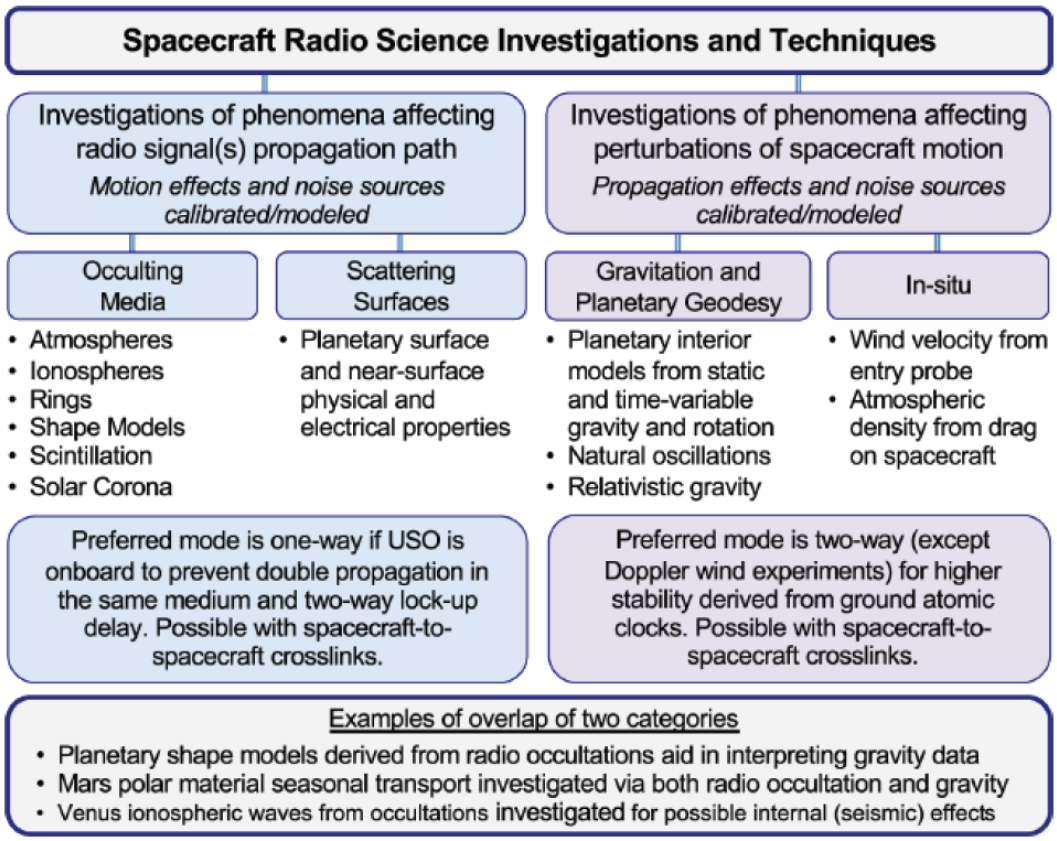

Figure 1.3: Classification of radio science investigations by phenomena investigated, courtesy of [Asmar, 2022].

1.2.2 Radiometric Observables and Tracking Configurations

Radiometric tracking is currently the most employed and reliable navigation method for space missions [Asmar, 2022]. As will be better defined in section 1.2.5, the state of the spacecraft cannot be observed directly, but it must be estimated through the analysis of observables generated from the tracking data sent by the spacecraft. When performing radiometric tracking, different types of measurements, or observables, can be recorded. The accuracy of tracking or estimation of the physical parameters of the transmission channel depends on the type and quality of the radiometric observables received.

Radiometric tracking can be performed in different configurations, as illustrated in Fig. 1.4. Some radiometric observables can be generated only when tracking with specific configurations, or operational modes. Operational modes, or tracking configurations, are classified as follows.

- One-way configuration: When tracking in the one-way operational mode, the downlink radio signal is generated on-board the spacecraft, using an Ultra-Stable Oscillator (USO), and transmitted to the ground station. From a technological perspective, this operational mode is possible only if the oscillator in use satisfies the stability required by the scientific investigation. Alternatively, a variation of this operational mode is the one-way uplink configuration, where the signal is generated on

the ground, and received at the spacecraft. While the latter is promising for long-distance communication thanks to the transmission power available on the ground, the spacecraft must be capable of processing the data, instead of simply performing frequency synchronization operations [Tyler et al., 2009, Asmar, 2022].

- Two-way configuration: The two-way operating mode occurs when the ground station transmits the radio signal, the spacecraft receives it, performs frequency synchronization and demodulation, and then retransmits it in a phase-coherent mode to the same station. The hydrogen maser at the station allows the transmitted signal to benefit from a very stable frequency reference, making this tracking configuration the most accurate and favorable for tracking and radio science experiments [Asmar, 2022].

- Three-way configuration: During three-way tracking, a first station generates the uplink signal, the spacecraft receives it, and then it is coherently retransmitted back to Earth to a different station. This occurs as a result of the high Round-Trip Light-Time (RTLT) when performing tracking at interplanetary distances, as the transmitting station can be no longer visible to the spacecraft due to Earth's rotation. In consideration of this, usually a different station on another continent is used to receive the downlink leg. This mode also occurs when two or more stations are meant to receive the same spacecraft signal concurrently, but only one station has the capabilities of sending the uplink, placing the other station in three-way mode.

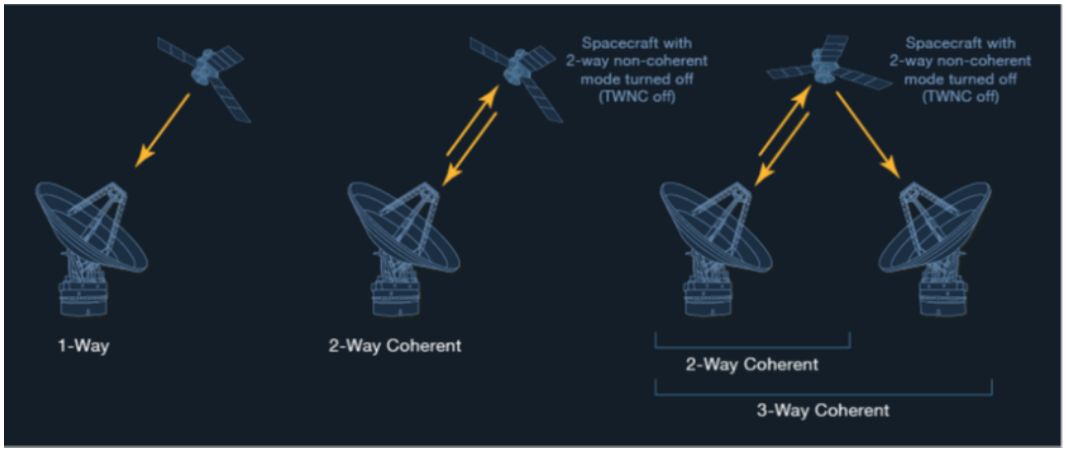

Figure 1.4: Usual radiometric tracking configurations [Doody, 2011].

Radiometric observables are the result of some measurable effect on the signal, which in turn contains information on the state of the spacecraft. These are generated by processing the downlink signal to estimate the useful information content, which in turn is mapped to the position, attitude, or velocity of the spacecraft.

The simplest radiometric measurement involved in spacecraft tracking is the range observable. This data contains information on the slant range between the spacecraft and the ground station. The currently operational ranging system at the Deep Space

Network (DSN) is the Sequential Ranging Assembly (SRA) [Moyer, 2005], and the conceptual implementation is based on the comparison between the transmitted range code and a model of the received one. The ideal instantaneous ranging ρ is defined in Eq. 1.1 [Schutz et al., 2004].

$$\rho = \sqrt{(\mathbf{r} - \mathbf{r}_r) \cdot (\mathbf{r} - \mathbf{r}_r)} \tag{1.1}$$

Where $\mathbf{r}$ and $\mathbf{r}_r$ are the positions of the spacecraft and the receiver, respectively. The associated observable is measured by estimating the one-way transmit time of the ranging signal. This can be generated at the ground station to estimate the round-trip transmit time, or directly at the spacecraft if a one-way configuration is employed. The ranging observable ρ_{obs} is found through Eq. 1.2 accordingly to the operational mode, where τ_1 and τ_2 are the computed one-way and round-trip transmit times, respectively.

$$\rho_{obs} = \tau_1 c = \frac{1}{2}\tau_2 c \tag{1.2}$$

The ranging observable is different from the instantaneous range, in consideration of the introduction of delays caused by the Earth's atmosphere and other transmission media, and due to the clock synchronization of the time-keeping subsystems involved. In this context, the use of a two-way tracking configuration provides a more accurate observables generation. Details on the modelling of error sources for ranging observables are discussed more in detail in [Schutz et al., 2004], chapter 3.

The range-rate observables, also called Doppler observables, are the most used and reliable radiometric measurements. The one-way range-rate defines the derivative with respect to time of the line-of-sight topocentric range, therefore it can be analytically described as in Eq. 1.3 [Schutz et al., 2004].

$$\dot{\rho} = \frac{\dot{\boldsymbol{\rho}} \cdot \boldsymbol{\rho}}{\rho} \tag{1.3}$$

The Doppler observables are based on the Doppler shift experienced by signals due to the motion of the transponders involved in the telecommunication link. For one-way and two-way operational modes, the sky frequency received on the ground is defined in Eq. 1.4 [Thornton and Border, 2003].

$$f_R = \alpha(1 - \frac{2\dot{\rho}_{obs}}{c})f_T = (1 - \frac{\dot{\rho}_{obs}}{c})f_T \tag{1.4}$$

Where α is the turn-around ratio of the spacecraft transponder, c the speed of light in a vacuum, and f_T the transmitted frequency. The turn-around ratio is required in a two-way or three-way configuration to avoid interference between the uplink and the downlink legs of the transmission. This parameter is a scalar that increases or reduces the downlink frequency according to ratios specific to the frequency bands involved. From the received frequency, the range-rate can then be directly computed as in Eq. 1.5.

$$\dot{\rho}_{obs} = \frac{c}{2}(\frac{f_R}{\alpha f_T} - 1) = c(\frac{f_R}{f_T} - 1) \tag{1.5}$$

From a practical point of view, the observed range-rate is estimated by integrating the phase difference between a reference tone (i.e. transmitted frequency) and the sky frequency [O'Dea and Kinman, 2019, Buccino et al., 2018, Thornton and Border, 2003], or by estimating the residual frequency with respect to the reference one through spectral analysis [Togni et al., 2021]. The operative algorithm employed to perform the generation of Doppler observables depends on how the data are acquired and recorded. For open-loop receiver, where a fixed bandwidth is recorded, raw data are digitalized and post-processing allows more versatility in their handling [Thornton and Border, 2003]. Closed-loop receivers directly generate the observables by cycle counting and only output frequency estimations at the specified count time.

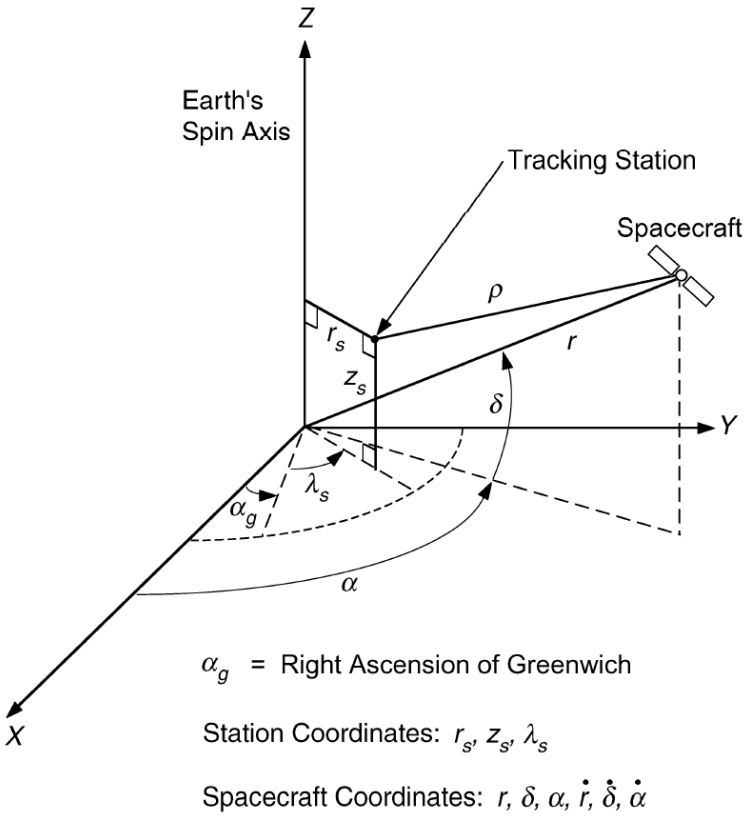

Figure 1.5: Tracking geometry in an inertial reference frame, courtesy of [Thornton and Border, 2003].

With respect to Fig. 1.5, the simplified model in Eq. 1.6 was developed and described in [Curkendal and McReynolds, 1969]. In this, the topocentric range-rate is defined as the sum of two contributions: the geocentric range-rate and the projected station velocity on the station-spacecraft vector.

$$\dot{\rho}(t) = \dot{r}(t) + \omega_e r_s cos(\delta) sin(\omega_e t + \phi + \lambda_s - \alpha) \tag{1.6}$$

In Eq. 6, ω_e is the mean rotation of Earth and ϕ is the phase angle that depends on the epoch. The qualitative plot of Eq. 1.6 is reported in Fig. 1.6. While this model can produce accurate results, it is valid only when non-gravitational accelerations acting on the spacecraft are negligible. Additionally, given its simplicity it's possible to expand

the two terms of Eq. 1.6 into a 6-parameter equation linear in its unknowns, making it possible to perform a least square estimation of the trajectory of the spacecraft that provides rough but generally correct orbit estimations.

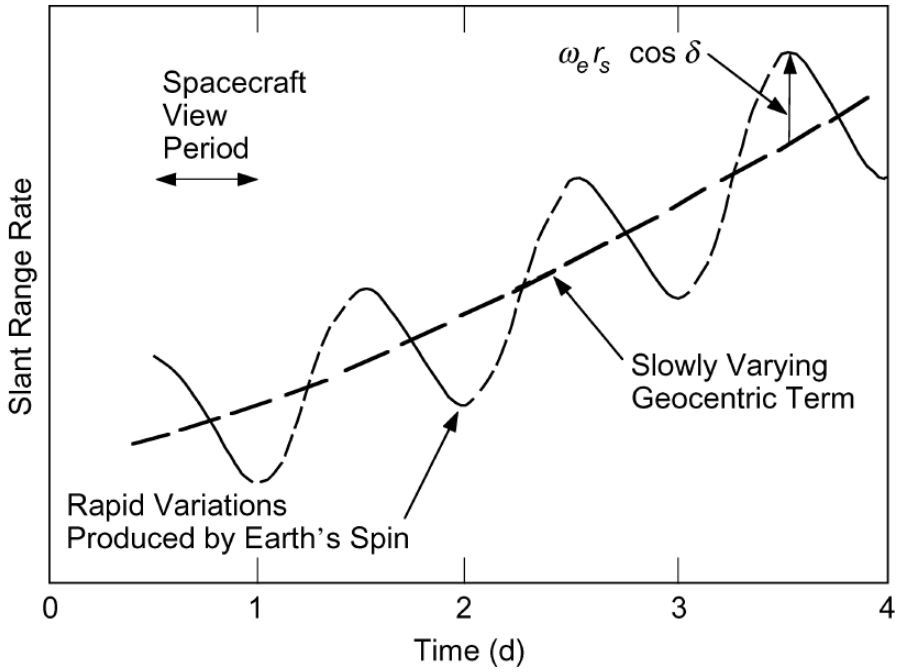

Figure 1.6: Expected observed range-rate of a spacecraft in deep space, courtesy of [Thornton and Border, 2003].

Very-Long-Baseline Interferometry (VLBI) observables are related to the angular position of the spacecraft with respect to a baseline vector between two stations. As the tracking signal is transmitted from the spacecraft, its arrival time to a receiver depends on the topocentric range, as previously discussed. If the spacecraft is visible from two or more stations at the same time, the downlink transmission can be recorded by multiple receivers. As the arrival delay depends on the wavefront of the signal, Eq. 7 can define the geometric delay τ_g.

$$\tau_g = \frac{1}{c}\boldsymbol{B} \cdot \hat{\boldsymbol{s}} \tag{1.7}$$

Where $\boldsymbol{B}$ is the baseline between the two stations and $\hat{\boldsymbol{s}}$ the unit vector in the source direction. Assuming both stations rely on stable and accurate clocks, the downlink signals can be analyzed through cross-correlation, obtaining an estimation of the geometric delay. From this, the direction of arrival with respect to the baseline can be estimated, and the angular position computed. Additionally, if three or more stations are in line of sight of the spacecraft, the second angular component of the spacecraft can be deducted. VLBI measurements are affected by clock errors and atmospheric delays. In particular, local delays, such as the one caused by the passing of signals through the troposphere, can affect the generation of the VLBI observables if not appropriately calibrated [Thornton and Border, 2003].

Differently from the VLBI observables, the Delta VLBI observables can be employed

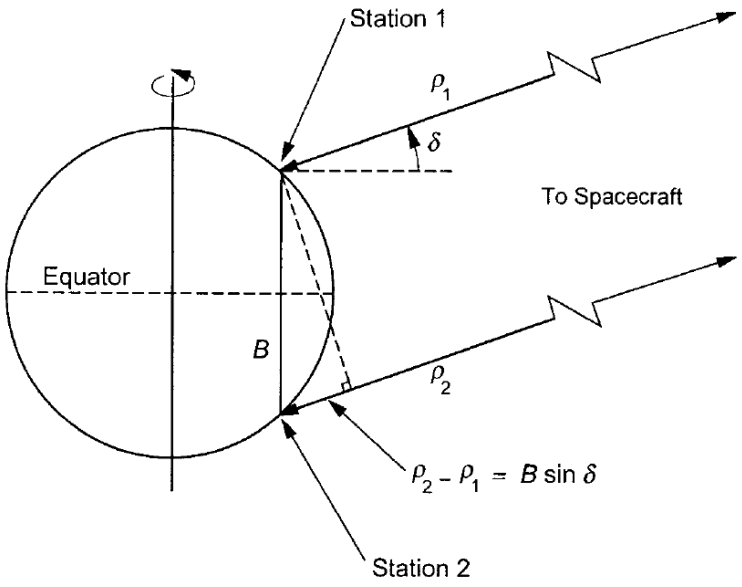

Figure 1.7: Very-Long-Baseline Interferometry, courtesy of [Thornton and Border, 2003].

to avoid the effect of uncalibrated delays. Delta VLBI measurements are based on the same principle as the VLBI ones, but tracking is performed on two signal sources at the same time. In particular, by recording signal sources (such as quasars) with a well-defined angular position at the same time of the transmission sent out by the spacecraft, it is possible to elide the effect of uncalibrated delays and timing offsets. While a vast catalogue of source positions is known [Jacobs et al., 2015], to perform Delta VLBI tracking the spacecraft and the source must be approximately at the same angular position from the viewing stations. Usually, the angular difference between the two sources is acceptable if less than 15 degrees.

1.2.3 Error Sources and Calibrations

As briefly introduced, various error sources can affect radiometric observables. It's important to underline there is difference between the physical effect represented by the observables, and their computed measurement. For a general observable q, this difference can be defined as $q = q_{obs} + \epsilon$, where the difference between the observable and its measurement is a small, non-negligible error ϵ due to uncalibrated noise sources.

The fundamental error source that affects any radiometric observable is the clock instability of the electronic systems involved in the communication link. The effect of a clock drift on the Doppler observables consists in a drift in the estimated range-rate, since the downlink frequency is mixed with a reference frequency and compared to the expected one. In one-way transmissions the reference frequency is given by an USO on-board the spacecraft, and the major error contribution is caused by the clock of the spacecraft. In a two-way operational mode, the signal is generated on the ground and coherently regenerated on-board. Here, the clock instability can be limited by using hydrogen masers at the station. For three-way transmissions, the tracking performance is degraded by possible clock offsets in the two receiving stations. Eq. 1.8 shows the error in the range-

rate estimation introduced by a frequency offset.

$$\Delta\dot{\rho} = c\frac{\Delta f}{f} \tag{1.8}$$

More in detail, the root-mean-square error introduced in the range-rate at a given count time τ_c and RTLT $M\tau_c$ is given by Eq. 1.9 [Thornton and Border, 2003]. The count time defines the observation time used to count the difference in cycles to estimate the Doppler observable.

$$\mathrm{RMS}_{\Delta\dot{\rho}} = \sqrt{2}c\sigma_y(2, M\tau_c, \tau_c) \tag{1.9}$$

Where σ_y is the Allan standard deviation of the clock. The Allan standard deviation itself is a measurement of the instability of clocks, accounting for short-term jitters and long-term drifts. This is defined in [Riley and Howe, 2008] as in Eq. 1.10, defining the stability over a sampling interval τ.

$$\sigma_y(\tau) = \sqrt{\frac{1}{2(M-1)}\sum_{i=1}^{M-1}[y_{i+1} - y_i]^2} \tag{1.10}$$

The Allan standard deviation for the hydrogen masers employed in ground stations is generally around 8×10^{-15} for a count time of 60 seconds, and down to 10^{-15} at 1000 seconds [Thornton and Border, 2003]. At these values of clock instability, the noise introduced in the Doppler observables generation is negligible when compared to other noise sources. The effect of a clock instability on the range observables is defined in Eq. 1.11.

$$\Delta\rho = \sqrt{2}c\tau\sigma_y(\tau_c) \tag{1.11}$$

The effects of clock offsets on range and range-rate observables are defined in Eq. 1.12 and Eq. 1.13.

$$\Delta\dot{\rho} = c\Delta T \tag{1.12}$$

$$\Delta\rho = \dot{\rho}\Delta T \tag{1.13}$$

Other noise sources in deep space Doppler tracking have been identified and characterized by previous studies, with the objective of defining models and suppression strategies to improve tracking accuracies [Iess et al., 2014, Asmar, 2022]. The principal noise sources in deep space Doppler tracking are generally divided in six categories [Asmar, 2022]:

- Thermal noise: thermal noise is caused by the agitation of electrons inside of the electronic components of the receiver. This noise is usually modelled as white in frequency, and is proportional to the system temperature of the receiving asset. Its effects on the accuracy of tracking will be addressed in detail in sections 2.3 and 2.6.
- Solar plasma: the interaction between the transmitted signal and solar plasma causes

phase scintillation and intensity fluctuations [Asmar, 2022]. While this effect can be probed with radio science missions, it can greatly affect navigation capabilities of spacecraft traversing the elliptic plane, especially when the spacecraft is in solar conjunction. The intensity of the link degradation is inversely proportional to the Sun-Earth-Probe (SEP) angle and the square of the signal's frequency. Calibration of solar plasma-induced phase delays can be performed through multi-link transmissions [Bertotti et al., 1993, Tortora et al., 2004, Iess et al., 2014], effectively reducing the negative effects of solar wind on the channel quality.

- Ionosphere: similarly to solar plasma, the electronic content of the Earth ionosphere causes phase accelerations of the transmitted signal. Calibration strategies are the same that are employed for solar plasma: through a multi-link communication link, the differential refractivity can be estimated and compensated.

- Troposphere: when multi-link transmissions are available, tropospheric delay is one of the main contributors to tracking inaccuracies. The phase delays introduced depend on the thermodynamic parameters of the local atmosphere. These can be estimated through statistical (seasonal) models, by propagating surface weather measurements, or by using GNSS-based delay estimations or microwave radiometers. When using advanced instrumentation (AWVR, TDCS) to measure directly the total path delay, the calibration is the most accurate [Buccino et al., 2021, Manghi et al., 2021]. Less accurate estimations can be obtained by using models to estimate the contribution of wet and dry components on the signal path [Saastamoinen, 1972, Manghi et al., 2021] or by averaging the path delay computed for multiple GNSS-transmitters.

- Spacecraft delay variation: internal delays when the signal travels from the electronics to the transmitting antenna can introduce a bias in the measurement of the observables. These effects are calibrated before the start of the mission, but with the aging of electronic components these can vary during the spacecraft lifetime, and therefore we should keep into account some uncertainty.

- Ground station delay uncertainty: ground stations are characterized by the movement of mechanical elements with high inertias and sensibility to environmental changes. Due to these effects, the transmission path from the receiver to the backend (which can be up to a few kilometers from the antenna) can change, introducing unmodelled delays in the radiometric measurements.

With regard to the effects of thermal, tropospheric, and dispersive noise, their intensity can be estimated from the stability (i.e. Allan deviation) of the downlink frequency. Fig. 1.8 shows the fractional frequency stability of the downlink Doppler measurements of InSight during Sol 921 and the associated models. At different integration times τ, different models can be applied. Thermal noise can be modelled as white phase noise, the effect of the troposphere on the data is white in frequency, and dispersive noise (i.e. ionosphere and plasma noise) can be described by Kolmogorov noise.

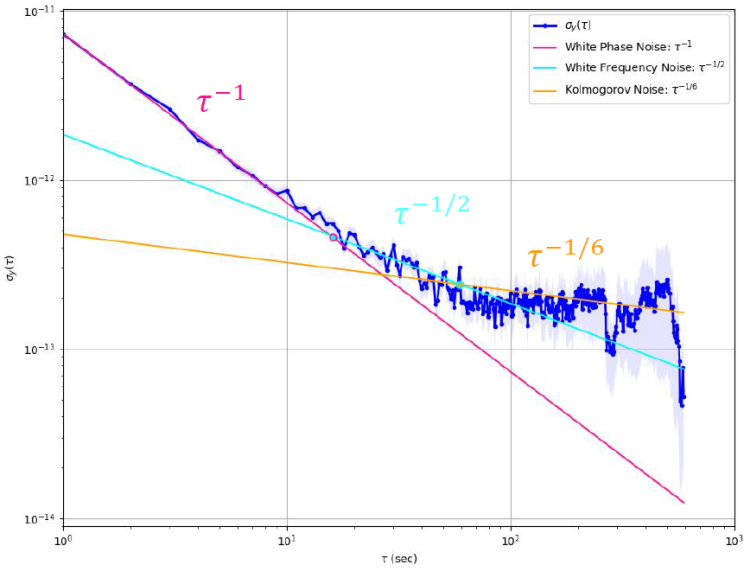

Figure 1.8: Allan deviation (experimental and model) of InSight Doppler residuals during Sol 921, courtesy of [Buccino, 2021].

1.2.4 Fundamentals of Astrodynamics

The study of astrodynamics is concerned with the computation of the orbits of planets, satellites, and artificial bodies in the Solar System. As every massive object obeys Newton's laws of motion, the precise estimation of ephemerides requires the accurate evaluation of the accelerations acting on the target of the analysis. Most of modern astrodynamics investigations are focused on the generation of ephemerides for spacecraft, with the objective of navigation or scientific investigation of the space environment. With reference to Fig. 1.9, which describes the simple restricted two-body problem model, the gravitational attraction between the primary m_1 and the spacecraft m_2 is defined as in Eq. 1.14.

$$\mathbf{F}_{12} = -\mathbf{F}_{21} = -\frac{Gm_1m_2}{r^3}\mathbf{r} \tag{1.14}$$

Where $\mathbf{r} = \mathbf{R}_2 - \mathbf{R}_1$ is the distance between the center of mass of the two bodies and $G = 6.6743 \times 10^{-11}$ $[m^3kg^{-1}s^{-1}]$ is the gravitational constant. When Eq. 1.14 is coupled with Newton's second law the equation of motion of the spacecraft with respect to the origin of the reference frame can be analytically or numerically computed.

In consideration of a general and more accurate model where the spacecraft ephemeris is affected by multiple accelerations, the fundamental equation of motion can be written as in Eq. 1.15 [Milani and Gronchi, 2010].

$$\dot{\mathbf{X}} = \mathbf{F}(\mathbf{X}, t, \boldsymbol{\mu}) \tag{1.15}$$

Where $\mathbf{X}$ is the state vector of the spacecraft, t the epoch associated to it, and $\boldsymbol{\mu}$ the array of the dynamical parameters of the model. The dynamical parameters consist in all those variables that influence the solution of the equation of motion of a spacecraft. The state vector is a mathematical construct that completely defines the spacecraft in space at any epoch $t \geq t_0$. The state vector $\mathbf{X} \in \mathbb{R}^p$ consists in a number of parameters sufficient to

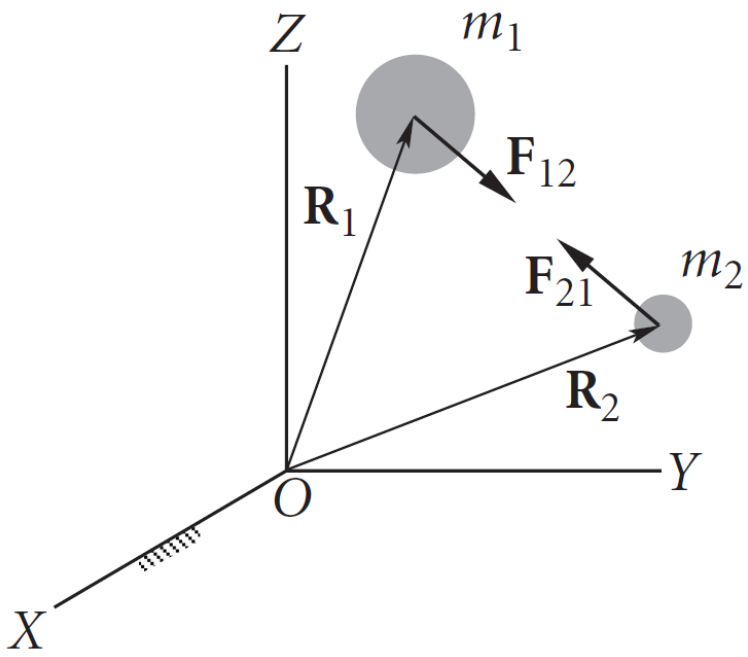

Figure 1.9: Free-Body diagram in the restricted two-body problem, courtesy of [Curtis, 2013].

uniquely characterize the position and attitude of the spacecraft. Necessarily then, under the hypothesis of the spacecraft being a rigid body with 6 degrees of freedom in space, $p \geq 6$. The general solution (or integral flow) of Eq. 1.15 is in the form:

$$\mathbf{X} = \mathbf{X}(\mathbf{X}_0, t, \boldsymbol{\mu}) \tag{1.16}$$

This last equation defines a mapping function from the initial condition or state vector $\mathbf{X}_0$ and dynamical parameters to the state of the spacecraft at the current epoch t. The concepts of integral flow and mapping between epochs are strictly related to the state transition matrix and their properties are described in detail in [Schutz et al., 2004, Milani and Gronchi, 2010].

Eq. 1.16 can be rewritten using the Newton-Euler formulation for a clearer definition of the fundamental equation of motion for a spacecraft.

$$\begin{cases} \dot{\mathbf{r}} = \mathbf{v}(\mathbf{r}, t, \boldsymbol{\mu}) \\ \dot{\mathbf{v}} = \mathbf{F}(\mathbf{r}, t, \boldsymbol{\mu}) \end{cases} \tag{1.17}$$

In Eq. 1.17, the dot notation defines differentiation with respect to time. It can also be noted that the arrays on left-hand side of the equation satisfy $\frac{d\mathbf{X}}{dt} = [\dot{\mathbf{r}}\ \dot{\mathbf{v}}]$. The non-linear vector function $\mathbf{F}$ in Eq. 1.17 defines the dynamical model of the Solar System and the accelerations affecting on the spacecraft. As this function encompasses multiple effect, it is convenient to separate it into different functions to isolate the components at play. While separating F into the single accelerations is formally correct, it is not convenient for a general description, since these effects depends on the mission geometry and spacecraft trajectory. Similarly to [Milani and Gronchi, 2010], the following general-purpose model

can instead be used.

$$\frac{d\mathbf{X}}{dt} = \mathbf{F}_0(\mathbf{X}, t, \boldsymbol{\mu}_0) + \mathbf{F}_1(\mathbf{X}, t, \boldsymbol{\mu}_1) + \mathbf{F}_2(\mathbf{X}, t, \boldsymbol{\mu}_2) \tag{1.18}$$

Eq. 1.18 decomposes the function $\mathbf{F}$ into separated components with decreasing effects on the state vector. In particular, the unperturbed equation of motion is defined by $\mathbf{F}_0$, while $\mathbf{F}_1$ and $\mathbf{F}_2$ respectively describe the most relevant and the negligible perturbations affecting the state vector. With this distinction, there is no need to separate perturbations into gravitational and non-gravitational (or surface) forces, as can alternatively be done.

Perturbations

Perturbations in the orbit of spacecraft are deviations from the undisturbed motion caused only by the gravitational attraction of the primary. In ideal conditions, the spacecraft acts only under the effect of gravitational attraction and follows Kepler's laws. In reality, multiple effects affect the orbit of the spacecraft, to the point that the real orbit can change drastically from the undisturbed one. This difference can be appreciated by integrating the orbit from the initial state of the spacecraft (i.e. solving the Cauchy Problem), which consists in finding a solution that satisfies Eq. 1.15. Different approaches can be taken to integrate the trajectory of the spacecraft, and modern astrodynamics usually employs numerical integration techniques to provide very accurate results [Gurfil, 2006]. In these, the single perturbing forces are isolated and computed at each integration time. The most important accelerations affecting the state of spacecraft are:

- Newtonian gravitational acceleration caused by massive objects other than the primary body, also known as n-body perturbations. This effect is generally computed using a point-mass equation. Its perturbing effects are greater when the standard gravitational parameter Gm_1 of the primary is lower, and the orbital altitude increases.

- Tides, caused by periodic variations in the distribution of mass inside of the primary. For Earth, these are further divided in pole tides, solid Earth tides, and ocean tides. Pole and solid Earth tides account for the deformation of Earth due to its elasticity, while ocean tides describe the motion of masses of water. These are modelled thanks to surveys from geodesy satellites, such as TOPEX and GRACE [Gurfil, 2006], and are usually accounted for as variations in the Earth gravitational potential from the ideal spherical model.

- Aspherical gravitational potential of the primary, defined as spherical harmonics expansions of the gravitational acceleration. Due to oblateness, non-homogeneous mass distribution, and other effects, the gravitational attraction of primaries does not equal the one of a point-mass with the same gravitational parameter. To account for this effect, the primary potential is written as a spherical harmonic potential equation in an Earth-centered, Earth-fixed reference frame [Gurfil, 2006]. Spherical harmonics are described by coefficients, usually presented in the form $J_{i,j}$, which

define the intensity of the single harmonic contribution to the gravitational potential. For practical applications, the spherical harmonics are truncated, depending on the accuracy required by the trajectory estimation, and multiple models exist for the Earth potential [Gurfil, 2006, Vetter, 1994].

- Atmospheric drag, caused by the momentum exchange between gas particles around the primary and the surfaces of the spacecraft. This effect is accounted for through empiric atmospheric density models and approximations of the shape of the S/C. Given the dependency of the vertical density profile on the solar flux and geomagnetic indices, current atmospheric models introduce around a 15% error in the estimation of atmospheric drag [Gurfil, 2006].

- Solar radiation pressure (SRP), caused by the photon interaction (reflection, absorption) with the spacecraft. Similarly to atmospheric drag, SRP must account for the intensity of solar activity, the shape, and the attitude of the spacecraft. The main error sources when computing this acceleration are estimations of the solar luminosity, numerical approximations, approximations in the shadow models, and incorrect estimation of the spacecraft attitude.

- Planetary radiation pressure, caused by albedo and thermal radiation from the primary. Similarly to SRP, this effect accounts for the impulse caused by photons reflected by the primary.

Other effects include the gravitational accelerations due to unconventional mass contributions, such as mascons or planetary rings, uncertainties in the performed maneuvers, such as the effect of misalignments in the thrusters, thermal imbalances, or leakage from the stored propellant.

Fig. 1.10 shows a general-purpose division of disturbing functions and the order of magnitude of their intensity at variable orbit altitudes. As the numerical integration of the equation of motion can require intensive computations, different missions can truncate or ignore certain perturbing forces, depending on the required OD accuracy. Usually, disturbances due to gravity are computed as a correction to the gravitational potential (e.g. Tides, gravitational harmonics) [Vallado, 2005], while surface forces are computed as function of the spacecraft mass and mechanical properties. Various complete and truncated empiric models exist to estimate these effects. For a more comprehensive discussion see [Vallado, 2005, Gurfil, 2006].

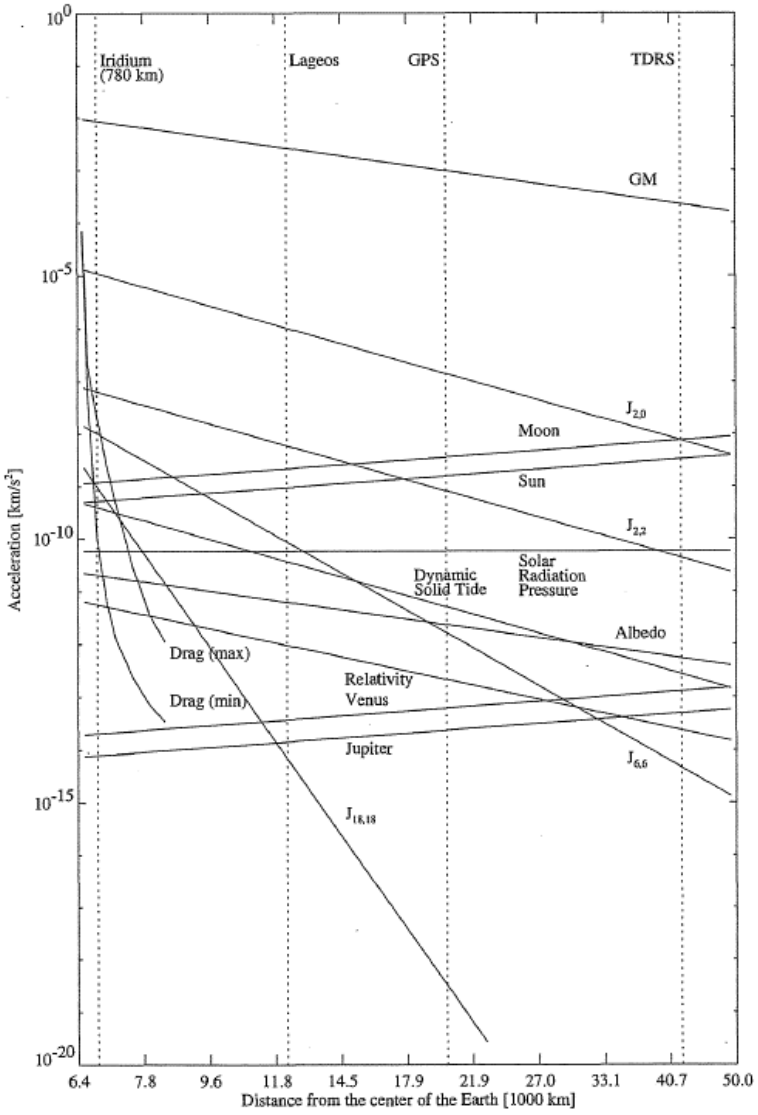

Figure 1.10: Order of magnitude of various perturbations on a satellite orbit at difference orbital altitudes, courtesy of [Montenbruck et al., 2002].

1.2.5 Statistical Orbit Determination

Modern orbit determination procedures rely on a stochastic approach to find the best solution to the problem of estimating the state and trajectory of a spacecraft. This is achieved by performing tracking routines and processing the data registered at a receiver, usually a ground station. The objective of statistical orbit determination is to unambiguously estimate the state vector of the tracked spacecraft, with the limitation that this cannot be observed directly. This inability and the nonlinearity of the problem introduce the requirements of implementing a mathematical model to describe the dynamics of the spacecraft, and to perform an accurate estimation of the observed quantities. The statistical orbit determination process can be summarized using the following system of differential equations [Schutz et al., 2004]:

$$\begin{cases} \dot{\mathbf{X}} = \mathbf{F}(\mathbf{X}, t) \\ \mathbf{Y}_i = \mathbf{G}(\mathbf{X}_i, t_i) + \epsilon_i \end{cases} \tag{1.19}$$

Where $\mathbf{Y}_i$ is the set of observations at the epoch t_i, also called observables. $\mathbf{F}$ and $\mathbf{G}$ are nonlinear equations that relate the state vector $\mathbf{X}$ to the appropriate variables, and ϵ_i is the noise affecting the observations. Operatively, statistical OD is performed by an iterative comparison of the observables generated by the processing of the received data (i.e. observed observables) with the observables computed using the dynamical model described by Eq. 1.15 (i.e. computed observables). Overall, the objective is to change iteratively the parameters $\boldsymbol{\mu}$ of the dynamical model, as previously defined, to minimize the difference between the observed and the computed, called the residuals. Only after the residuals are minimized, navigation commands can be applied to the spacecraft, or new model estimations formulated using the newly fine-tuned parameters.

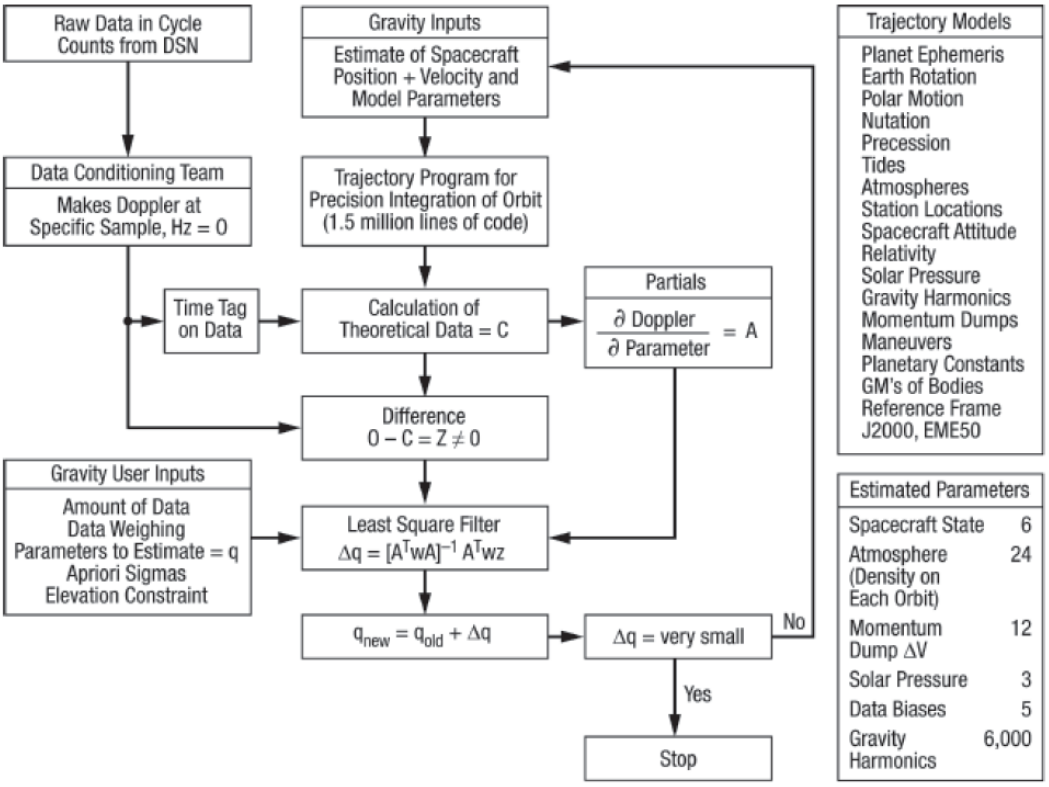

Figure 1.11: The navigation and orbit determination process, described as an iterative procedure to estimate the trajectory of spacecraft and related dynamical parameters, courtesy of [Asmar, 2022].

In general, the point at which the spacecraft is tracked and observations are collected is called the topocenter. In consideration of this, the integration of the equation of motion and the processing of the observables must account for the contribution in the definition of the position of the spacecraft. In this context, the topocentric range, which coincides with the slant-range, is recalled [Sansò and Rummel, 1989].

$$\boldsymbol{\rho} = \mathbf{r} - \mathbf{r}_r \tag{1.20}$$

Where the topocentric range $\boldsymbol{\rho}$ is related to the position of the topocenter $\mathbf{r}_r$ and the one of the spacecraft $\mathbf{r}$. In Eq. 1.20, the range is found by processing the range measurements obtained and performing an estimation of the state of the spacecraft, while the position of the spacecraft comes from the integration of the equation of motion, as defined in Eq. 1.17, and the coordinates of the topocenter come from estimations based on the theory of deformable Earth. As defined in Eq. 1.15, the state of the spacecraft depends on the dynamical parameters of the model employed, so that $\boldsymbol{\rho} = \boldsymbol{\rho}(t, \boldsymbol{\mu})$.

As defined, statistical orbit determination is an iterative procedure that requires the linearization of the state of the spacecraft about a nominal condition. In consideration of the uncertainties in the dynamical model and the trajectory of the target, Eq. 1.20 will not be exact. It is therefore possible to define the general a-priori (or computed) observable $Y_c = Y_c(t, \mathbf{P}_R)$, with $\mathbf{P}_R$ being the vector of the parameters to which the observable is sensitive. If the predicted model and state are sufficiently close to the real ones, a first order approximation of the true vector $\mathbf{P} = \mathbf{P}_R + \Delta\mathbf{P}$ is possible with acceptable errors. The real observable can therefore be written as a function of the a-priori (or computed) observable, as in Eq. 1.21.

$$Y(t, \mathbf{P}) = Y_c(t, \mathbf{P}_R) + \sum_i \frac{\partial Y}{\partial P_i} \Delta P_i \tag{1.21}$$

Eq. 1.21 can be further expanded in Eq. 1.22 in consideration of the nature of the observable considered. For radiometric tracking, all observables depend, generally, on the state of the spacecraft, the position of the topocenter, and the dynamical model.

$$Y(t, \mathbf{P}) = Y(\mathbf{X}_S(t, \boldsymbol{\mu}_1), \mathbf{X}_T(t, \boldsymbol{\mu}_2)) \tag{1.22}$$

Where $\boldsymbol{\mu}_1$ is the subset of $\mathbf{P}$ to which the state of the spacecraft is sensitive, such as its velocity, the coefficients of the gravitational harmonics, or surface forces parameters. $\boldsymbol{\mu}_2$ consists in those parameters on which the position and velocity of the topocenter depend, such as tidal model parameters, or the Earth orientation parameters at the epoch of tracking. Overall, the residual observables (i.e. the observed minus computed) can be formally described as in Eq. 1.23. Given the observation equation (Eq. 1.23) and multiple observations from a single satellite arc it's then possible to define a complete system to be solved each iteration of the orbit determination process, until the residuals $\Delta\mathbf{Y}$ are acceptable.

$$\Delta Y = Y(t, \mathbf{P}) - Y_c(t, \mathbf{P}_R) = \left[\frac{\partial Y}{\partial \mathbf{X}_S}, \frac{\partial Y}{\partial \mathbf{X}_T} \right]_{\mathbf{P}_R} \sum_i \left(\frac{\partial}{\partial P_i} \right)_{\mathbf{P}_R} \left[\mathbf{X}_S \mathbf{X}_T \right] \Delta P_i \tag{1.23}$$

In consideration of the cardinality of $\mathbf{P}$, it is a common choice to divide the array in different classes of parameters, depending on the type of mission that is tracked [Milani and Gronchi, 2010]:

- Solve-for parameters: the improved estimation of these parameters is the objective of the OD procedure. The values of these directly affects the observables, and they

are iteratively changed to improve the quality of the residuals. The state of the spacecraft is always considered a solve-for parameter.

- Consider parameters: this set includes all those parameters that affect the observables, but whose estimation cannot be improved with the tracking. The uncertainty in these parameters reduces the accuracy of the solution of the OD.

- Exact parameters: these parameters are considered, for the purpose of the OD procedure, as exactly known. This set includes both parameters that do not affect the observables and the state of the spacecraft, and those with a negligible uncertainty.

Another distinction for the solve-for parameters consists in their definition as arc-dependent or arc-independent.

- Internal parameters $\mathbf{P}_I$: these parameters depend on the single arc considered, such as the state of the spacecraft, or the Earth orbital parameters at the epoch of the arc.

- External parameters $\mathbf{P}_E$: these are the global parameters, and their value is applicable to all observables from the spacecraft, independently on the arc considered.

This distinction introduces the possibility of using observables from multiple arcs to minimize the uncertainty in the estimation of the parameters of the dynamical model. This approach is called multi-arc [Milani and Gronchi, 2010, Sansò and Rummel, 1989], and consists in the sequential analysis of all the (single) tracking arcs, identified by different boundaries conditions. This multi-arc approach increases the number of observations that depend on the external parameters, increasing the accuracy of their estimation. In addition, the accuracy of estimation can be further increased by selecting the arcs with more favorable conditions (high SNR, optimal geometry, etc.).

Single-Arc and Multi-Arc Approach

The orbit determination process using the single-arc and multi-arc approaches is performed as follows.

$$\mathbf{A}^{(m\times n)}\mathbf{X}^{(n\times 1)} = \mathbf{L}^{(m\times 1)} \tag{1.24}$$

Eq. 1.24 defines the linear observation equations in matrix form, where $\mathbf{A} = \frac{\partial Y_i}{\partial P_j}$ is the partial derivatives matrix, with m observables and n unknown parameters. Due to measurement errors in the observables, it is possible to write explicitly $\mathbf{L} = \mathbf{l} + \mathbf{r}$, with $\mathbf{l} = (\mathbf{Y} - \mathbf{Y}_c)_{t_i}$ and $\mathbf{r}$ the vector of residuals. In consideration of $m > n$ the objective of orbit determination is therefore to solve:

$$\mathbf{AX} - \mathbf{l} = \mathbf{r} \tag{1.25}$$

And the least square estimate $\hat{\mathbf{X}}$ of $\mathbf{X}$ is given by the minimization of Eq. 1.26.

$$\mathbf{r}^T\mathbf{P}_l\mathbf{r} \tag{1.26}$$

Where $\mathbf{P}_l$ is the weight matrix that depends on the a-priori standard error of unit weight σ_0, and the covariance matrix of the observations $\mathbf{C}_l$, as reported in Eq. 1.27.

$$\mathbf{P}_l = \sigma_0^2\mathbf{C}_l \tag{1.27}$$

The weight coefficient matrix is then defined as $\mathbf{Q}_l = \mathbf{P}_l^-1$. For uncorrelated observations (normally assumed for tracking data) $\mathbf{C}_l = \mathbf{I}$, with $\mathbf{I}$ the identity matrix. After performing matrix operations, it is possible to write the solving equation to find the minimum of the residuals as Eq. 1.28.

$$\mathbf{A}^T\mathbf{P}_l\left(\mathbf{A}\mathbf{X} - \mathbf{l}\right) = 0 \tag{1.28}$$

Then, by letting $\mathbf{N} = \mathbf{A}^T\mathbf{P}_l\mathbf{A}$ and $\mathbf{b} = \mathbf{A}^T\mathbf{P}_l\mathbf{l}$, it is possible to write the least squares normal equations as:

$$\mathbf{N}\mathbf{X} = \mathbf{b} \tag{1.29}$$

With the sought-for least square estimation of the parameters being:

$$\hat{\mathbf{X}} = \left(\mathbf{A}^T\mathbf{P}_l\mathbf{A}\right)^{-1}\mathbf{A}^T\mathbf{P}_l\mathbf{l} = \mathbf{N}^{-1}\mathbf{b} \tag{1.30}$$

With the weight coefficient matrix of the solution being $\mathbf{Q}_{\hat{\mathbf{X}}} = \mathbf{N}^-1$. From this, it is possible to compute the covariance matrix (Eq. 1.31).

$$\mathbf{C}_{\hat{\mathbf{X}}} = \left(\mathbf{l}^T\mathbf{P}_l\mathbf{l} - \mathbf{l}^T\mathbf{P}_l\mathbf{A}\hat{\mathbf{X}}\right)\mathbf{Q}_{\hat{\mathbf{X}}} = \hat{\sigma}_0^2\mathbf{Q}_{\hat{\mathbf{X}}} \tag{1.31}$$

Where the a-posteriori variance of unit weight $\hat{\sigma}_0^2$ appears. The covariance matrix contains the information on the uncertainties in the estimated parameters after the model has converged to a solution. The standard deviation $\hat{\sigma}_{\mathbf{X}_i}$ and the correlation $\mathbf{K}_{ij}$ between all unknowns of $\hat{\mathbf{X}}$ can be estimated from the elements of the covariance matrix, as shown in Eq. 1.32 and Eq. 1.33.

$$\hat{\sigma}_{\mathbf{X}_i} = \sqrt{\mathbf{C}_{\hat{\mathbf{X}}}^{ii}} \tag{1.32}$$

$$\mathbf{K}_{ij} = \frac{\mathbf{C}_{\hat{\mathbf{X}}}^{ij}}{\sqrt{\mathbf{C}_{\hat{\mathbf{X}}}^{ii}\mathbf{C}_{\hat{\mathbf{X}}}^{jj}}} \tag{1.33}$$

The extension of the single-arc analysis to a multi-arc procedure can be performed by splitting the normal equation system (Eq. 1.29) into partitioned matrices. By dividing the system it's possible to explicit the normal equation system for the K^{th} arc.

$$\begin{bmatrix}\mathbf{N}_{II} & \mathbf{N}_{IE}^T\\ \mathbf{N}_{IE} & \mathbf{N}_{EE}\end{bmatrix}^K\begin{bmatrix}\mathbf{X}_I\\ \mathbf{X}_E\end{bmatrix}^K = \begin{bmatrix}\mathbf{b}_I\\ \mathbf{b}_E\end{bmatrix}^K \tag{1.34}$$

Where the internal parameters $\mathbf{X}_I$ and the external parameters $\mathbf{X}_E$ are isolated. By considering this matrix equation after estimating the internal parameters of all the arcs through a single-arc analysis, the residual unknown is the array of external parameters $\mathbf{X}_E$ that affect the observables of the arcs. The solving system then becomes:

$$\mathbf{X}_I^K = \mathbf{N}_{II}^{-1}(\mathbf{b}_l - \mathbf{N}_{IE}^T \mathbf{X}_E)^K \tag{1.35}$$

And the reduced normal equations:

$$\mathbf{N}_K^* \mathbf{X}_E = \mathbf{b}_k^* \tag{1.36}$$

By combining the solving equations for all arcs ($K = 1, ..., N$) the solution for the external parameters can be found:

$$\hat{\mathbf{X}}_E = \sum_{K=1}^{N} (\mathbf{N}_K^*)^{-1} \sum_{K=1}^{N} \mathbf{b}_K^* \tag{1.37}$$

With:

$$\mathbf{N}_K^* = \left(\mathbf{N}_{EE} - \mathbf{N}_{IE}\mathbf{N}_{II}^{-1}\mathbf{N}_{IE}^T\right)^K \tag{1.38}$$

$$\mathbf{b}_K^* = \left(\mathbf{b}_E - \mathbf{N}_{IE}\mathbf{N}_{II}^{-1}\mathbf{b}_I\right)^K \tag{1.39}$$

For more details on astrodynamics fundamentals, radiometric observables, or statistical orbit determination, see [Schutz et al., 2004, Gurfil, 2006, Milani and Gronchi, 2010, Vallado, 2001].

1.3 Ground Stations for Deep Space Tracking

Tracking spacecraft over interplanetary distances is a technological challenge that requires dedicated infrastructure to receive and process signals. The role of ground stations in near and deep space missions is to provide communication capabilities to perform Tracking, Telemetry and Command (TTC) during all phases of a mission. In this section, a functional description of ground stations for near and deep space operations is provided. The most common architectures and configurations are then described to provide an overview on the mechanical and RF components involved in radio tracking. Finally, the role of networks when dealing with spacecraft operations is discussed.

1.3.1 Architectures and Acquisition Chain

Deep space antennas are systems characterized by high directional gains and complex mechanical structures. Even though small variations in the hardware employed and in the acquisition chain can be identified at different stations, all of them have similar configurations. Fig. 1.12 describes the functional architecture of a ground station for tracking in near and deep space.

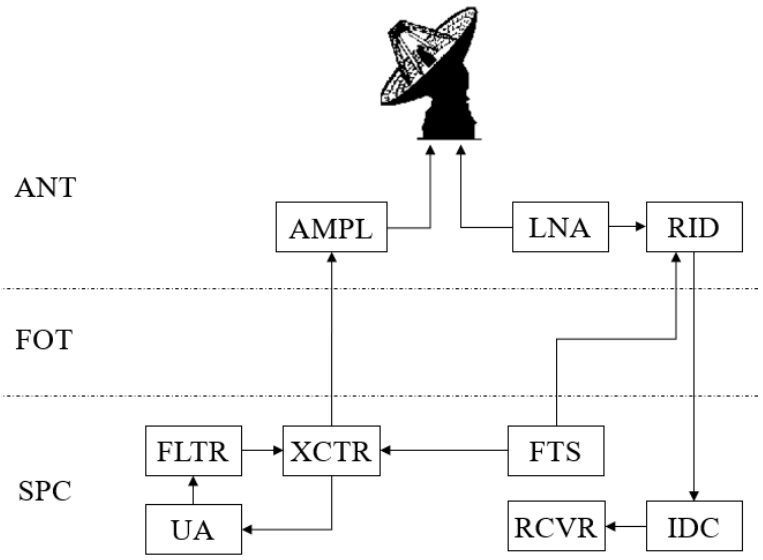

Figure 1.12: General architecture of ground stations involved in space operations.

In Fig. 1.12 three macro-sections are highlighted:

- Antenna (ANT): Here, the downlink signal is received at the parabolic reflector and transmitted to the radio-frequency front end (or feed). At the same time, the uplink signal can be emitted and sent to space.
- Fiber Optic Transmission line (FOT): This subsystem is concerned with the transmission of the signal from the front end to the receiver, which in some cases can be several km far from the dish. The employment of fiber optic instead of a beam waveguide (BGW) or coaxial cables greatly reduces the transmission losses, which can consist in tens of dB for the distances and frequencies involved.
- Signal processing center (SPC): Here, the signals are converted to the digital domain and processed to extrapolate the required downlink phase that contain information on the spacecraft state, and to compute the uplink phase to modulate on the carrier.

In the functional diagram, the low-noise amplifier (LNA) amplifies the received signal while introducing the least amount of thermal noise. This step can be performed in multiple steps, with a first cryogenic LNA and successive hot LNAs. After being amplified, the downlink signal is transmitted to the RF-to-IF downconverter (RID). Here, it is mixed down to an intermediate frequency that can be processed and digitalized later. The Intermediate Frequency (IF) employed is in the order of 100 MHz. As mixing introduces new frequency components, appropriate filtering is also performed at this step. The down-conversion is achieved with the support of the Frequency and Timing Subsystem (FTS), which provides a very high-stable time and frequency reference for accurate processing. This subsystem is usually a hydrogen maser, which is characterized by a very high frequency stability. In the SPC, the signal is converted from analog to digital in the IF-to-Digital Converter (IDC) before being transmitted to the receiver. In this step, the digital gain is usually set in an automatic way to minimize the quantization noise of

the digitalization. Finally, the signal is sent to the receiver to extract the signal phase, generate the data types used for radiometric tracking, and demodulate TM.

Uplink activities, on the contrary, are characterized by an Uplink Assembly (UA) that generates the modulation and frequency to be transmitted and records their phase. The UA sends the signal phase to an exciter for up-conversion to radio-frequency (RF). The exciter itself is connected to the FTS to generate a stable and coherent phase. The uplink signal is then passed to an amplifier (AMPL) (e.g. Klystron) before being radiated into space.

With regard to receivers, there are currently different standard ones employed in ground stations over the globe. The most common ones for deep space operations are the following:

- Downlink Tracking & Telemetry (DTT): This NASA receiver is commonly employed in 34-m and 70-m antennas of the DSN. The DTT is particularly useful when performing tracking activities, as it employs a digital Phase-Locked Loop (PLL) to acquire and track the downlink phase and generate telemetry, ranging, and doppler observables.

- Radio Science Receiver (RSR): The RSR is the radio science receiver equipped at designated stations of the DSN to acquire data for radio science investigations. The RSR can record up to 4 channels of raw data points in variable bandwidths, and is particularly useful when more information than the single carrier frequency is requested, as post-processing algorithms can be employed to perform spectral analysis.

- Open Loop Receiver (OLR): The OLR, similarly to the RSR, is employed in DSN stations to record data in a defined and variable bandwidth. Developed as part of a standardization strategy of NASA, the OLR can replace the RSR, having the same functionalities [Jongeling and Navarro, 2019].

- Intermediate Frequency and Modem System (IFMS): the IFMS is a receiver developed by ESA. It is an integrated system that provides ranging, telemetry, and telecommand services for deep and near space missions. This receiver can record open-loop and closed-loop in parallel, making it a flexible and general purpose receiver.

- Telemetry, Tracking & Control Processor (TTCP): The TTCP receiver is an ESA receiver. This is the receiver most commonly employed in stations of the European Space Tracking (ESTRACK) network. Similarly to the IFMS, the TTCP allows the recording of open-loop and closed-loop data in parallel.

With regard to the mechanical structure, the most common architecture for antennas is an Azimuth/Elevation pointing system, while the dimension of the main reflector ranges between 21-m to 70-m, with the most used being the 34-m parabolic dish of DSN complexes. Fig. 1.14 presents the general architecture of a 34-m beam waveguide (BWG)

antenna of the DSN [Imbriale, 2005]. With regard to the mechanical and radio-frequency (RF) equipment, all antennas involved in space operations employ a parabolic reflector to channel the downlink signal into the receiver and achieve a high directional gain. The receiver itself can be located in the phase centre of the main reflector (i.e. at the focus of the parabola) or in a room in the pedestal of the antenna. Different solutions define the configuration employed by the antenna.

For a front-feed configuration, the receiver is positioned in the focus of the main reflector. This solution is characterized by a relatively low aperture efficiency (55-60%) and a high sensitivity to mechanical deformations due to gravity. Other configurations involve the transmission of the signal to a receiver located in the base of the antenna. This can be achieved by sending the RF signal through coaxial cables or BWG. The usual technical solution used is a series of mirrors (or BWG) to send the signal down to the appropriate receiver. In particular, this solution is very versatile as it allows multi-frequency transmissions using dichroic mirrors, and flexibility in changing the receiver at will, usually through a rotation and retransmission of the signal path. On the contrary, BWG are characterized by spillover losses caused by the non-ideal illumination of the mirrors. An alternative solution employed at the DSN in the past consists in antennas with a Cassegrain configuration (see Fig. 1.13), with the feed located directly in the center of the main reflector.

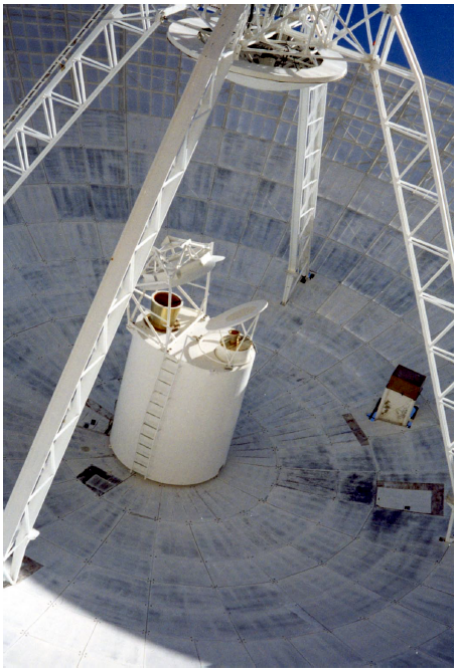

Figure 1.13: Detail of the front end of DSS-12 positioned in the main reflector, courtesy of [Imbriale, 2005].

Independently on the configuration and transmission strategy, all antennas are characterized by a directional gain proportional to the effective aperture of their main reflector. This gain can be reduced by inaccuracies in the parabolic geometry or manufacturing quality. The quality of the surface of the main reflector can in fact reduce the antenna gain. This effect is stronger as the signal frequency increases. The metric used to quantify these losses is the root-mean-square (RMS) of the surface accuracy. This can be evalu-

ated experimentally by performing holographic measurements, and strategies to reduce it include active surface compensations.

Other losses at the antenna are caused by the dislocation of the subreflector, causing deviations in the transmitted signal and a worse spillover efficiency. As these variations affect the station delays, they must be appropriately computed and mapped. Given that this effect depends on a variation in the gravity vector, the deviations from the nominal condition are worse at low elevations.

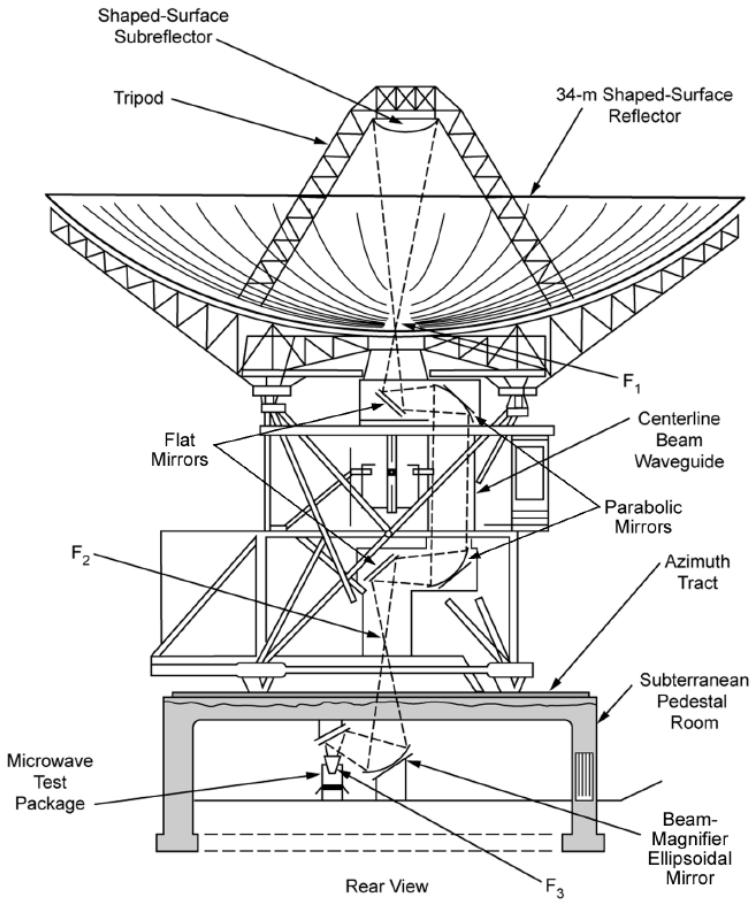

Figure 1.14: General architecture of a DSN 34-m BWG antenna, courtesy of [Imbriale, 2005].

Fig. 1.15 shows the architecture of a NASA-JPL feed, as currently employed at the affiliated node DSS-69 in Italy. The signal transmitted via BWG is channeled through a corrugated feed horn as it enters the feed. Filters and isolators are then used to limit the bandwidth of the signal around the operating band and avoid interference. Multiple LNAs are then used in series, with the noise figure of the first cryogenic stage dominating over the others. The RF (and still analog) signal is then down-converted to an intermediate frequency with one or more mixers. As the signal is down-converted to the order of MHz, it is then transmitted to the back-end for digitalization using an optical link.

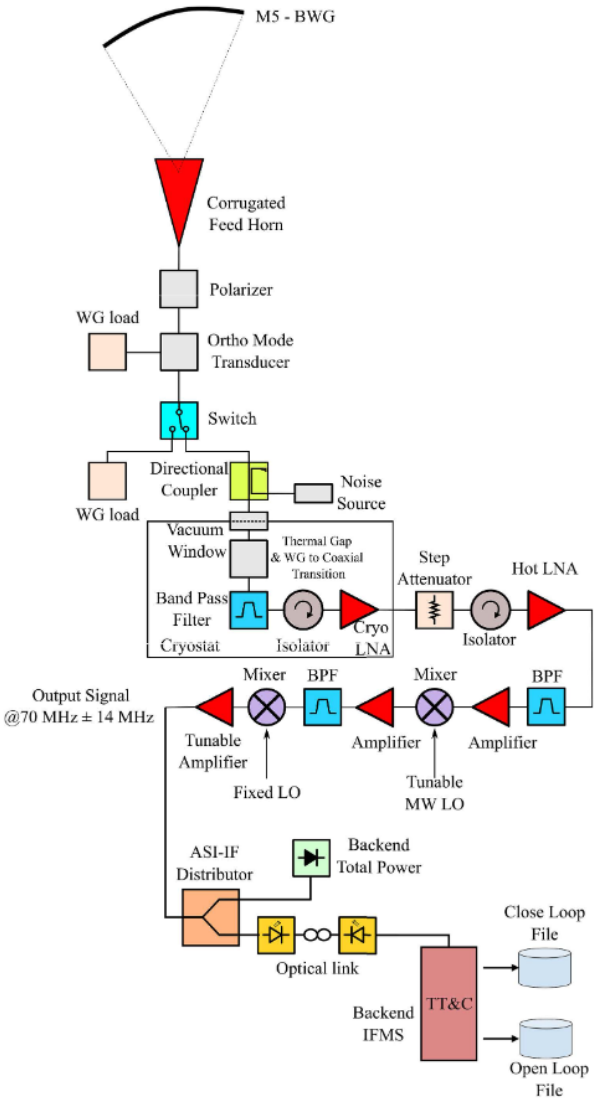

Figure 1.15: RF architecture of the feed of DSS-69, courtesy of [Valente et al., 2022].

1.3.2 Networks and Tracking Windows

Tracking of spacecraft during critical mission phases, such as Entry, Descent, and Landing (EDL), planetary encounters, or fly-bys is crucial for successfully performing investigations in deep space. As the limitation in the access time for the ground segment can preclude these missions to be successful, there's been an effort in the development of globally distributed networks of ground stations to support space endeavors with continuous and redundant communication coverage.

Thanks to international collaboration, multiple complexes and stations are currently capable of supporting tracking in the Solar System, creating networks with minimal outages of access time. The two largest networks currently supporting deep space missions are the Deep Space Network (DSN) of NASA and the European Space Tracking (ESTRACK) network of ESA. In addition to these, commercially operated or affiliated stations support operations by reducing the load on the main tracking complexes. Examples of these are the DSN affiliated nodes Sardinia Deep Space Antenna (DSS-69) managed by the Italian

Space Agency (ASI) [Valente et al., 2022], the Morehead State University ground complex DSS-17 [Pham, 2022], or the Goonhilly Earth Station.

The Deep Space Network (NASA)

The DSN is a network of globally distributed complexes with multiple antennas at each location. With the main stations of the DSN separated by approximately 120 degrees in longitude, and present in both Earth hemispheres, this network of ground stations managed by the Jet Propulsion Laboratory (JPL) has been providing support to deep space missions since its establishment in 1958. The DSN consists in three main DSCCs: the Goldstone DSCC in California (USA), the Madrid DSCC in Spain, and the Canberra DSCC in Australia.

Figure 1.16: Locations of NASA stations as of 2017. Stations outlined in red are part of the Deep Space Network (DSN). Stations outlined in green are part of the Near Earth Network (NEA). Stations in blue are part of the Space Network (SN) [Mai, 2017].

Every DSCC includes multiple deep space stations that employ large parabolic dish antennas and dedicated RF equipment. Stations are classified with respect to their architecture, namely 34-m high efficiency (HEF) antennas, 34-m BWG antennas, and 70-m deep space (D.S.) antennas. The HEF antennas - as well as the D.S. ones - rely on a BWG architecture, their naming convention was chosen to distinguish them from the previous antenna architecture, which was not designed for optimum gain-to-noise-temperature (G/T) [Imbriale, 2005]. Table 1.2 provides an overview of the capabilities of the deep space stations currently active at the three DSN complexes.

The DSCC are strategically positioned to isolate them from unwanted RF interferences and provide maximum coverage. Following this strict requirement, DSN complexes are located in remote locations, or in areas shielded by natural formations.

Table 1.2: Capabilities of DSN Deep Space Stations [Tai, 2019].

Complex	DSS ID	Size (m)	Type	Uplink	Downlink	EIRP (dBm)	G/T (dB/K)
	15	34	HEF	X	S,X	109-140	39.1-56.2
	23*	34	BWG	X	X,Ka	134-145	51.3-62.5
Goldstone	24,26	34	BWG	S,X,K	S,X,K,Ka	109-145	40.6-62.5
	25	34	BWG	X,Ka	X,Ka	134-145	51.3-62.5
	14	70	D.S.	S,X	L,S,X	132-146	48.3-61.7
	45	34	HEF	S,X	S,X	109-140	39.1-56.2
	33*	34	BWG	X	X,Ka	134-145	51.3-62.5
Canberra	34,36	34	BWG	S,X,K*	S,X,K,Ka	109-145	40.6-62.5
	35	34	BWG	X,Ka*	X,Ka	134-145	51.3-62.5
	43	70	D.S.	S,X	L,S,X	132-146	48.3-61.7
	65	34	HEF	S,X	S,X	109-140	39.1-56.2
	53	34	BWG	X	X,Ka	134-145	51.3-62.5
Madrid	54,56	34	BWG	S,X,K	S,X,K,Ka	109-145	40.6-62.5
	55	34	BWG	X,Ka *	X,Ka	134-145	51.3-62.5
	63	70	D.S.	S,X	L,S,X	132-146	48.3-61.7

* represents features that are planned in the near-term future

European Space Tracking Network (ESA)

The ESTRACK Network consists in the infrastructures that provide a link between spacecraft and the ESA's Operations Control Center at ESOC. The objective of ESTRACK is to provide global coverage for near and deep space missions. To do so, it relies on a core network of seven core stations, which are then complemented by the augmented and cooperative networks, respectively operated by commercial entities or by external agencies. At present, there are seven ESA core stations that support space operations: Kourou (French Guiana), Cebreros (Spain), Redu (Belgium), Santa Maria (Portugal), Kiruna (Sweden), Malargue (Argentina), and New Norcia (Australia). Of these, only three constitute the ESA Deep Space Network (EDSN) and support deep space missions: New Norcia (DSA-1), Cebreros (DSA-2), and Malargue (DSA-3).

Figure 1.17 shows the ESA stations around the globe. Table 4 summarizes the capabilities of the main ESTRACK deep space antennas to support deep space missions.

The stations of the EDSN employ a 35-m main reflector, with a Cassegrain feed configuration and BWG to transmit the signal to the front end at the base of the antenna. The concept of operations of ESTRACK relies on a single Operations Control Centre (ESOC) that is connected and provides commands to all ground stations of the network.

The RF parameters for the EDSN are reported in Table 4. While DSA-1 supports S-band and X-band operations for both uplink and downlink transmissions, DSA-2 only supports X-band uplink and downlink in X and Ka-band. DSA-3 has X and Ka capabilities for both uplink and downlink operations.

Figure 1.17: Locations of ESTRACK stations as of 2017. Blue stations are owned and operated by ESA. Orange stations are procured commercially and operated by commercial entities. Green stations are owned and operated by external agencies, but regularly support ESA missions [ESA, 2015].

Table 1.3: Capabilities of ESTRACK Deep Space Antennas.

Complex	DSA ID	Size (m)	Type	Uplink	Downlink	EIRP (dBm)	G/T (dB/K)
New Norcia	1	35	BWG	S, X	S, X	97-107	37-57
Cebreros	2	21	BWG	X	X, Ka	107	50-57
Malargue	3	35	BWG	X, Ka	X, Ka	100-107	50-57

Chapter 2

Data Pre-processing

Contents

The purpose of signal processing is to extract as much information as possible from a signal and use it for effective decision-making. Radiometric tracking is based on the estimation of changes in the parameters of radio-frequency signals. The employment of a radiometric communication link between ground segments and the spacecraft is often used for navigation purposes. At the same time radio science experiments rely on it as part of the investigation methodology, and estimate changes to the signal due to the transmission media encountered [Asmar, 2022].

The post-processing of signals recorded through open-loop receivers can serve various purposes in radio science applications. The spectrum-based estimation of frequency is widely used for carrier synchronization and TT&C operations [Katayama et al., 1992] and navigation [Bertotti et al., 1993, Togni et al., 2021, Asmar, 2022, Thornton and Border, 2003]. Planetary surfaces can be investigated remotely through spectral analysis of the phase noise and scattering introduced in the downlink leg [Simpson, 1993], and lunar geological structures through time-frequency analysis of echoes [Fa et al., 2015]. Characteristics of planetary interiors can be deducted by residual Doppler frequencies in the downlink signals [Asmar et al., 2017], and atmospheric-induced delays on the phase of signals make it possible to investigate the composition of large bodies [Tyler et al., 1989]. Unmodeled variations in the frequency of downlink signals can also uncover details on the structure of planetary rings [Thomson et al., 2007]. In this context, this chapter defines a formal framework for the characterization of non-stationary signals and their digitalization

(sections 2.1 and 2.2), presents the signal processing algorithm developed to deal with radiometric data for Doppler measurements estimatiion (section 2.3) and the validation procedures performed on it (section 2.4), introduces an experimental prediction model developed for the SNR threshold in signal detection (section 2.5), and describes the effect of the processing parameters on the quality of observables (section 2.6).

2.1 Signal Characteristics

Signals employed in radiometric tracking are characterized by high frequencies (see chapter 1), and the variations in their parameters are to be estimated to obtain information on the transmission media and dynamics of the transmitter [Asmar, 2022]. To perform correct estimations, the characteristics of these signals must be correctly defined to implement the most appropriate processing algorithms. The main classifications of signals consist in:

- Deterministic or random: A stochastic or random signal is characterized by a lack of predictability. In contrast to a deterministic signal, whose values can be perfectly defined at any moment, the value of a random signal at any instant is unknown. It cannot be anticipated based on the knowledge of values at other prior instants. It is only possible to estimate the parameters of random signals in a statistical way by computing their averages and moments.

- Stationary or non-stationary: When a signal is stationary, its defining parameters or their moments do not change with time. When it is non-stationary, there is a variability in the characteristics of the signal, and appropriate algorithms must be employed to account for the change in time of the defining parameters. Usual methods for the analysis of time-varying signals belong to the field of time-frequency analysis [Boashash, 2015].

- Single-tone or multi-tone: single-tone signals are characterized by a single frequency component and, therefore a localized energy accumulation in the frequency domain. Multi-tone signals, on the other hand, are defined by two or more tones. Generally speaking, estimation methods applicable to single-tone signals can be extended to multi-tone ones by using an estimate-and-subtract strategy [Serbes, 2021].

The signals employed in radiometric tracking can be of different kinds, depending on the radiometric observables to be recovered. Doppler tracking is based on carrier synchronization, and the downlink signal is a residual carrier with no modulation. Ranging requires telemetry, and signals can either use a suppressed-carrier or residual-carrier BPSK, QPSK, or offset QPSK modulation [O'Dea and Kinman, 2019]. The general mathematical model of radiometric signals is defined in Eq. 2.1.

$$x(t) = \left(m(t)\sqrt{2C}\right) cos\left(2\pi \int_0^t (f_c(\tau) + f_D(\tau)d\tau) + \theta(t)\right) + \nu(t) \tag{2.1}$$

Where $x(t)$ is the downlink signal, $m(t)$ the multiplicative noise, C is the signal's power, and $\sqrt{2C}$ the amplitude of the signal, f_c is the frequency of the carrier, f_D is the Doppler frequency, $\theta(t)$ is the instantaneous phase that can change due to modulation, and $\nu(t) \sim \mathcal{N}(0, \sigma^2)$ is the additive noise contribution modelled as Additive White Gaussian Noise (AWGN). If no modulation is employed, $\theta(t) = \theta(t_0) = \theta_0$, as the signal is considered in a finite interval starting at the epoch t_0. For most applications, especially in transmissions in near space, the multiplicative noise can considered negligible, and therefore $m(t) = 1 \forall t \in [t_0, t_{end}]$. The goodness of signals is evaluated through the signal-to-noise ratio (SNR). For a signal in the form of $x(t)$ ($m(t) = 1$) the SNR is defined as the ratio between the power of the deterministic signal and the power of the AWGN, computed as its variance. Eq. 2.2 defines the SNR by explicating the signal power C and its amplitude A, since $C = A^2/2$.

$$\mathrm{SNR} = \frac{C}{\sigma^2} = \frac{A^2}{2\sigma^2} \tag{2.2}$$

Signals can be defined either in the time domain or in the frequency domain. Both representations are equivalent and present the same information content but with different dependencies. For stationary signals, these two independent representations completely define the signals parameters [Boashash, 2015].

When considering one or the other representation, one must consider the properties that need to be explicated: signals in the time domain show the energy distribution of the signal with respect to time, while when operating in the frequency domain, the focus is given to the frequency content in the signal. The transformations from one domain to the other are called the Fourier Transform (FT) and the Inverse Fourier Transform (IFT) respectively. They are presented in Eq. 2.3 and Eq. 2.4.

$$\mathrm{X}(f) = F\{x(t)\} = \int_{-\infty}^{\infty} x(t) e^{-j2\pi ft} dt \tag{2.3}$$

$$x(t) = F^{-1}\{\mathrm{X}(f)\} = \int_{-\infty}^{\infty} x(t) e^{j2\pi ft} df \tag{2.4}$$

Where $\mathrm{X}(f)$ defines the frequency spectrum (or the FT) of $x(t)$. While $x(t)$ can be real or complex, $\mathrm{X}(f)$ is always complex. By performing operations on the frequency spectrum, other spectra can be derived as follows:

- Magnitude spectrum: $|\mathrm{X}(f)|$
- Phase spectrum: $\angle \mathrm{X}(f)$
- Energy spectrum: $|\mathrm{X}(f)|^2$

The energy spectrum is well contextualized by the Parseval theorem described by Eq. 5, which states the conservation of the signal energy in both domains.

$$\mathrm{E}_x = \int_{-\infty}^{\infty} |x(t)|^2 dt = \int_{-\infty}^{\infty} |\mathrm{X}(f)|^2 df \tag{2.5}$$

The signal described in Eq. 2.1 is a real-valued function, defining the physical signal transmitted to the ground station. When discretized and sampled, the associated digital signal is real-valued as well. As this is impractical due to ambiguities in the frequency components and spectral inefficiency due to the Hermitian symmetry of the signal itself [Boashash, 2015], the received data is always demodulated into I&Q components to obtain the equivalent analytic signal. Given a real signal $x(t)$, the complex signal $z(t)$ is said to be associated with $x(t)$ if Eq. 2.6 is valid.

$$z(t) = x(t) + j\mathrm{H}\{x(t)\} \tag{2.6}$$

Where $\mathrm{H}\{x(t)\}$ is the Hilbert transform of $x(t)$. The new signal obtained this way does not exhibit Hermitian symmetry, and therefore the positive and negative frequencies can be distinguished with no ambiguity. This result is derived from the transformation from a signal in a sinusoidal form, which corresponds to two complex exponentials, to a single complex exponential that defines the analytic signal. The Hermitian symmetry shown by a sinusoid comes directly from this consideration, as the arguments of the exponentials are equal but dissimilar in sign and show a mirrored amplitude in the energy spectrum after the Fourier transformation.

$$z(t) = \left(m(t)\sqrt{C}\right) exp\left(j\left(2\pi\int_0^t (f_c(\tau) + f_D(\tau)d\tau) + \theta(t)\right)\right) + \nu(t) \tag{2.7}$$

In general, the signal's frequency is a function of time, and both the carrier and the Doppler frequencies can be variable. If the tracking configuration is two-way or three-way, the uplink frequency is generally ramped to compensate for the cumulative Doppler effect of the uplink and downlink paths. This way, the downlink frequency should be equal to or close to a constant value. After mixing and digitalization, this translates to a base-band signal with a low residual frequency. Even though it is accurate, the pre-steering usually does not perfectly compensate for the Doppler effect, and therefore the residual frequency remains time-dependent and variable. In addition, possible amplitude fluctuations due to the transmission media can happen. Noise contributions, finally, are generally defined as random signals. While the noise contribution to the real signal is modelled as AWGN, after processing through the Hilbert transform, the noise becomes a Complex AWGN (CAWGN) in the form of $\nu_c(t) \sim \mathcal{CN}(0, \mathbf{I}\sigma^2)$, where the new noise power is spread on both the in-phase and quadrature components, and is uncorrelated to the original one. In light of these considerations, radiometric signals cannot be considered stationary or deterministic, and therefore their analysis requires the employment of estimation methods for time-frequency analysis [Boashash, 2015].

The time and frequency domain representations show the dependency of the signal from both variables. Differently from the case of stationary signals, the variations in the time and frequency domain are generally not mutually exclusive. Considering this, the Fourier transform is inadequate for a correct representation of the signal under analysis, as the evaluation of $\mathrm{X}(f)$ at any frequency value requires the computation of $x(t)$ at all time instants. To overcome this limitation, the time and frequency domain processing

are extended to a single Time-Frequency Representation (TFR), described by a Time-Frequency Distribution (TFD). Time-frequency distributions can simultaneously highlight a signal's energy concentration in both domains By defining $\rho_z(t, f)$ the TFD of $z(t)$, the energy flow in a spectral window Δf during a certain time interval Δt can be defined as in Eq. 2.8, highlighting the variability in both domains in a single representation.

$$\mathrm{E}_{\Delta f,\Delta t} = \int_{t_0-\Delta t/2}^{t_0+\Delta t/2} \int_{f_0-\Delta f/2}^{f_0+\Delta f/2} \rho_z(t, f) dt df \tag{2.8}$$

For any given time-frequency distribution, the product of the resolution in both domains has a lower bound. This comes from the Heisenberg uncertainty principle in quantum mechanics and is defined as Gabor's uncertainty principle [Gabor, 1946]. When performing estimations, it is therefore important to consider the bandwidth-duration product BT of a signal, where B is the range of frequencies where $\mathrm{F}\{z(t)\} \neq 0$, and T the range of times where $z(t) \neq 0$. The bandwidth-duration parameter describes the quantity of information contained in a signal or in part of it. Considering this principle, it is possible to have a low variance in the frequency estimation or in the time localization of the energy of a signal. This translates, when performing frequency estimation, in a direct dependency of the variance of estimation on the length of the signal considered. This will be addressed in detail in section 2.4 with the definition of the Cramér-Rao Lower Bound (CRLB).

The introduction of time-frequency distributions paves the way for the definition of a time-dependent frequency, generally known as the Instantaneous Frequency (FI), as in Eq. 2.9.

$$f_i(t) = \frac{1}{2\pi} \frac{d\theta}{dt}(t) \tag{2.9}$$

A visual representation of Eq. 2.9 is provided in Fig. 1, where the TFD is presented along the time domain and frequency domain ones. The signal represented is a single-tone non-stationary signal, with $m(t) = 1$, $\sqrt{2C}(t) = 1 + 0.1t$, $f_i(t) = -5 + t$, and SNR=30 dB. The single time and frequency domain cannot correctly show the energy distribution, as the former fails to represent the frequency content, and the latter cannot distinguish the variation in time of the tone. On the contrary, the TFD is able to map both variations simultaneously, reporting how the energy concentration changes with time.

Various TFDs can be employed for time-frequency analysis, each with its properties. The application of some of the most common TFDs to a monocomponent non-stationary signal is presented in Fig. 2 and Fig. 3 [Boashash, 2015]. The signal considered is sampled at 1 Hz, lasts 65 samples, has a frequency range from 0.1 Hz to 0.4 Hz, and has unit amplitude from sample 9 to sample 57.

Generally speaking, the Wigner-Ville Distribution (WVD) (Fig. 2.2 (a)) can be considered the fundamental TFD [Boashash, 2015], and all other time-frequency representations can be written as filtered or smoothed version of it. The WVD is defined as in Eq. 2.10.

$$\rho_z(t, f) = \int_{-\infty}^{\infty} z(t + \frac{\tau}{2}) z^*(t - \frac{\tau}{2}) e^{-j2\pi f\tau} d\tau \tag{2.10}$$

Where the operator * defines the conjugate of the complex z.

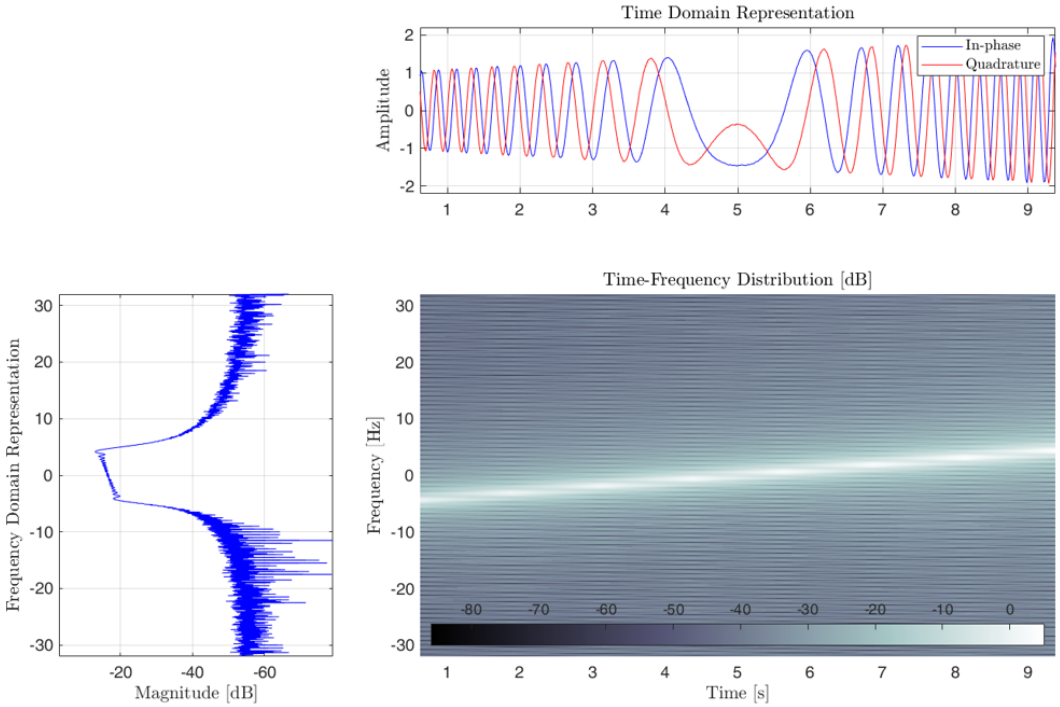

Figure 2.1: Time representation, frequency representation, and time-frequency representation of a residual-carrier signal with $\sqrt{2C}(t) = 1 + 0.1t$ and $f_i(t) = -5 + t$.

$$K_z(t,\tau) = z(t+\frac{\tau}{2})z^*(t-\frac{\tau}{2}) \tag{2.11}$$

Eq. 2.11 defines the signal kernel of the WVD. The kernel is designed so that its TFD is a unit delta function at the instantaneous frequency of the signal, which is linearized for the WVD [Boashash, 1992a, Boashash, 1992b].

While the WVD generates the sharpest ridge in the time-frequency domain, the presence of cross-terms (see Fig. 2.2 and Fig. 2.3) poses a challenge in the correct analysis of the signal. In particular, the WVD has a rapid degradation in its performance in the presence of noise, since the cross-correlation between signals and noise amplifies the artifacts that can be seen in Fig. 2.2. Cross-terms are often considered the main constraint in the analysis of signals through TFDs, and one of the solutions developed is the analysis of signals through the Short-Time Fourier Transform (STFT) and the spectrogram, as the cross-terms are filtered in these.

The STFT consists in the transformation of an arbitrary real or complex signal z(t) in the frequency domain, as described in Eq. 2.12. In practice, the signal is filtered using a sliding real and even function w, also known as observation window.

$$\mathrm{STFT}_z^w(t,f) = \int_{-\infty}^{\infty} z(\tau)w(\tau-t)e^{-j2\pi f\tau}d\tau \tag{2.12}$$

The spectrogram S is for the STFT the equivalent of the energy spectrum for the Fourier transform, as defined in Eq. 13.

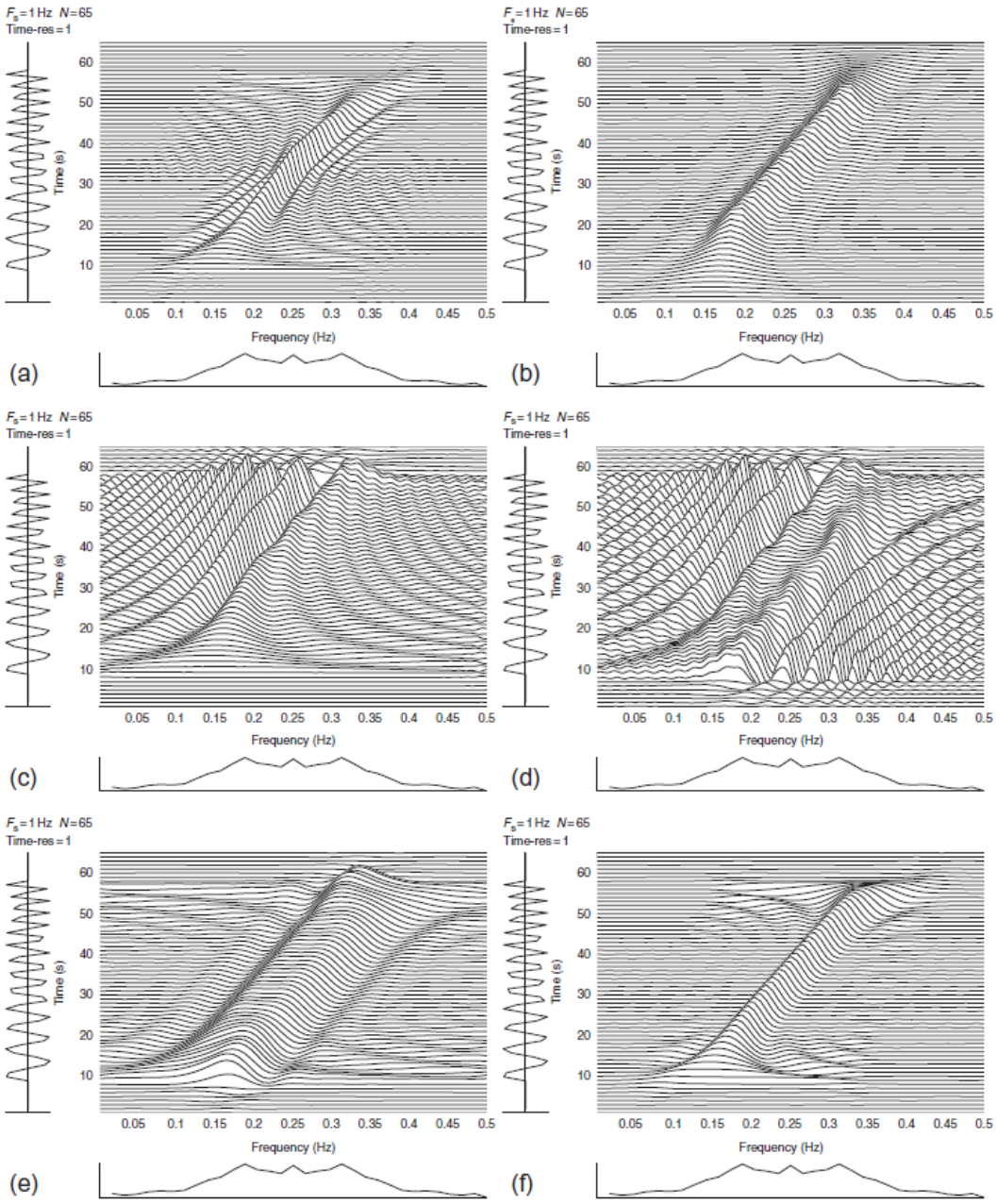

Figure 2.2: (a) Wigner-Ville; (b) Spectrogram, 21-point rectangular window; (c) Page; (d) Levin; (e) Windowed Levin, 19-point Hamming window; (f) exponential, $\sigma = 4$, courtesy of [Boashash, 2015].

$$\mathrm{S}_z^w(t,f) = \left| \int_{-\infty}^{\infty} z(\tau) w(\tau - t) e^{-j2\pi f \tau} d\tau \right|^2 \tag{2.13}$$

By performing the Fourier transformation using an observation window, the spectrum can be located in time, as opposed to the Fourier transform where the time-dependency creates ambiguities. From a practical point of view, the computation of the spectrogram of a signal can be considered as stacking multiple spectra one after the other, and obtaining a resolution in both time and frequency. Due to Gabor's uncertainty principle, the employment of large windows tends to smear the spectra obtained [Gabor, 1946, Boashash, 2015,

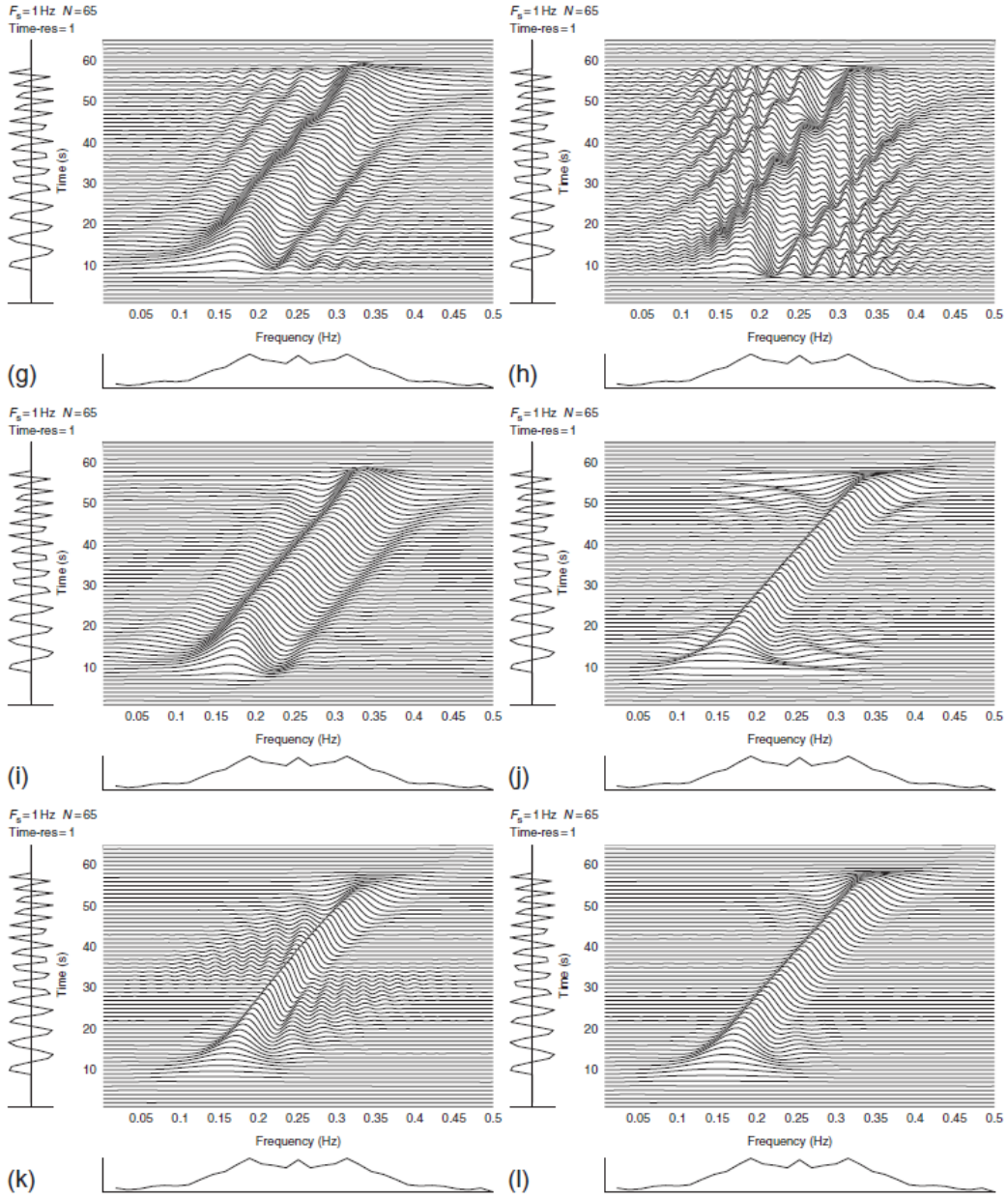

Figure 2.3: (g) Born-Jordan, $\alpha = 1/2$; (h) Zhao-Atlas-Marks, a = 2, $g_2(\tau) = 1$; (i) Zhao-Atlas-Marks, a = 2, $g_2(\tau)$ =19-point Hamming window; (j) Doppler-independent, $g_2(\tau)$ =29-point Hamming window; (k) Lag-independent, $g_1(t)$ =9-point Hamming; and (l) Separable kernel, $g_1(t)$ =9-point Hamming, $g_2(\tau)$ =29-point Hamming, courtesy of [Boashash, 2015].

Putland and Boashash, 2000]. Fig. 2.4 shows the ambiguity when computing the spectrogram of a signal with a linearly-variable frequency.

The time-frequency resolution when computing the spectrogram must be tuned according to the rate of change of the frequency components involved, which can be considered proportional to the intensity of the non-stationarity. While this procedure requires a two-step estimation, with the most accurate spectrogram being computed after a first rough analysis, it is possible to maximize the height of the spectrogram with respect to the noise floor. The ideal length of the observation window for the spectrogram is defined in Eq.

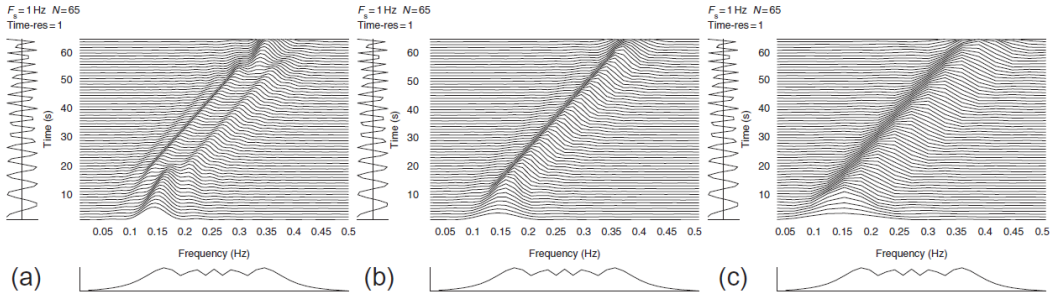

Figure 2.4: Spectrogram of a signal with linear frequency rate. (a) low window length (b) optimal window length (c) high window length, courtesy of [Boashash, 2015].

2.14 [Togni et al., 2021, Boashash, 2015], and describes the duration that minimizes the half-height width of the ridge of the spectrogram in the time-frequency domain. When this value is used as an upper bound, the instantaneous spectrogram (i.e. the energy spectrum in the time interval of interest) is also unimodal around the frequency of the tone to be estimated.

$$\Delta w = \sqrt{2} \left| \frac{df_i(t)}{dt} \right|^{-1/2} \tag{2.14}$$

Window functions can be used to alter the energy content of the signals to be processed. By doing so, negative effects after the digitalization can be attenuated or filtered, like leakage and scalloping losses. The only window that does not alter the signal to be processed is the rectangular window, which only accounts for the limitation in time of the recorded signal ($w(t) = 1 \forall t$).

When dealing with parameters estimation, the introduction of windows affect the accuracy of estimation of the signal frequency [Boashash, 2015, Fan et al., 2021]. In consideration of this, windowing functions will not be described in this dissertation, but a complete review of their design and applications can be found in [Prabhu, 2014].

2.1.1 Signal Detection

The generation of radiometric observables is strictly dependent on the correct estimation of the parameters of the signals involved. When using spectral methods, the estimation of parameters of stochastic signals is a non-linear problem, and the estimates and associated observables are correct up to a maximum accuracy that depends on the information content of the signal considered [Rife and Boorstyn, 1974]. The lower bound in the estimation accuracy of parameters is called the Cramér-Rao Lower Bound. These estimations exhibit a threshold effect when the energy of the deterministic part of the signal becomes small in comparison to the stochastic one (noise). This threshold defines the value of SNR at which the accuracy of estimation quickly decreases and departs from the theoretical minimum. Common metrics to evaluate the threshold effect and the accuracy of estimation are the Root-Mean-Square Error (RMSE) and the Mean-Square Error (MSE).

As usually happens in non-linear problems, the convergence to the correct solution

depends on a correct initialization around that value. In this context, the estimation of the parameters of signals is strictly related to detection of the signal itself through the noise caused by the transmission channel. In consideration of this, the probability of correctly detecting a signal through noise affects the MSE of estimation when dealing with stochastic signals. Fig. 2.5 shows the general MSE of estimation for the frequency of signals. In it, three different regions are highlighted:

- Asymptotic region: In this region the noise power is low when compared to that of the deterministic signal. When performing estimations, the signal is always detected and estimators will always converge to the correct solution. When using an optimal estimator, the MSE of estimation tends to the CRLB asymptotically, as no contribution from wrong initializations is affecting the accuracy of estimation.
- Threshold region: This region is characterized by a variable probability of detection. Therefore, the MSE is modulated by the number of outliers (i.e. incorrect initializations), which usually affects the estimation with a higher contribution than correct estimations.
- No-information region: In this region the signal is completely buried in noise, no information can be extracted from it and the estimation of the parameters is purely random. Estimations in this region are usually random variables with uniform probability distributions over the space of all admissible values.

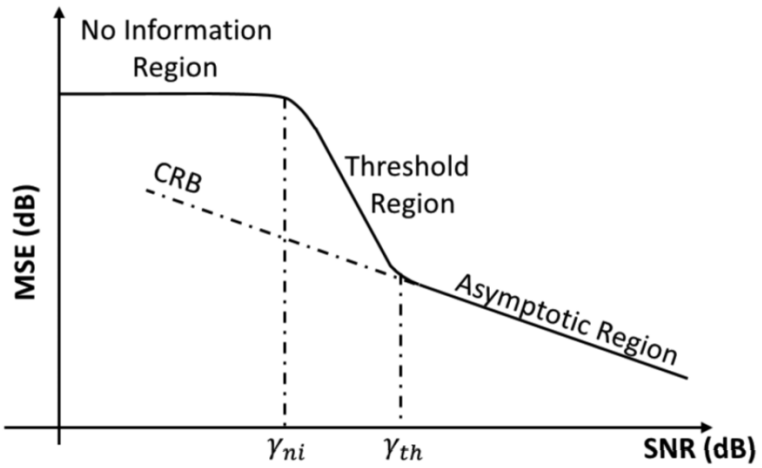

Figure 2.5: Signal detection regions as function of the SNR, courtesy of [Serbes and Qaraqe, 2022].

2.2 Digital Signal Processing

Even though signals are transmitted and received analogically, before being processed by a computer they need to be sampled and recorded. Digital signals are always processed to satisfy Nyquist-Shannon's sampling theorem. As previously defined, signals are made bandwidth-efficient by performing an Hilbert transformation on them. After digitalization

and Hilbert transformation, the real and analytic signal are defined as in Eq. 2.15 and Eq. 2.16.

$$x[n] = (m[n]\sqrt{2C[n]})cos\left(2\pi Fn + \theta[n]\right) + \nu[n] \tag{2.15}$$

$$z[n] = (m[n]\sqrt{C[n]})exp\left(j\left(2\pi Fn + \theta[n]\right)\right) + \nu[n] \tag{2.16}$$

Where $n = \{0, 1, \ldots N-1\}$ is the index of the sample considered. In consideration of a sampling frequency f_s, the signal is sampled at the time instants $t_n = n/f_s$, and the frequency of the signal is the normalized frequency $F = f/f_s$. Additionally, the dependency on the two frequency contributions is not explicit anymore, since the normalized frequency of the recorded signal is now dependent on the ratio of change of the instantaneous phase of the signal. In these equations the concept of sampling time $T_s = 1/f_s$ is introduced, implying a discretization of the signal in the time domain. The sampling time defines the difference between two consecutive acquisitions of the signal.

The Fourier transform can be performed on digital signals, and it takes the name of Discrete-Time Fourier Transform (DTFT) (Eq. 2.17). The DTFT takes a discrete signal as input, and is continuous in the frequency domain.

$$\mathrm{DTFT}_z(f) = \sum_{n=-\infty}^{\infty} z[n]exp(-j2\pi Fn) \tag{2.17}$$

An efficient and discrete implementation of the DTFT is the Discrete Fourier Transform (DFT), usually implement as a Fast Fourier Transform (FFT). The FFT performs a discrete transformation to the frequency domain, as defined in Eq. 2.18. It is computationally efficient, at the cost of a limited resolution.

$$\mathrm{DFT}_z(f) = \sum_{n=0}^{N-1} z[n]exp(-j2\pi kn/N) \tag{2.18}$$

In particular, the FFT is computed only at the discrete frequencies kn/N. The cardinality of the FFT of a signal $z[n]$ is the same as the one of the signal itself. In consideration of this, a strategy to increase the resolution of the FFT is to add samples to the signal without altering its information content. This strategy is called zeropadding, and consists in adding a trail of zeros to the digital signal. To obtain a signal of length M, the zeropadding ratio $Z = M/N$ is introduced, and the padding itself is achieved by adding $M - N$ zeros to the signal. For a given padded signal length M, the resolution of the DFT is defined as $\Delta F = 1/M$. As the discrete frequency is normalized, the resolution in the effective frequency of the signal is computed as $\Delta F = f_s/M$. From the DFT, the discrete amplitude, phase, and energy spectra can be computed. In particular, the discrete energy spectrum can also be referred to as the Power Spectrum (PS).

$$\mathrm{PS}_z(f) = \left|\sum_{n=0}^{N-1} z[n]exp(-j2\pi kn/N)\right|^2 \tag{2.19}$$

The PS can be normalized by the noise floor. With this approach, the realizations of the deterministic signal and random noise can be described using parametric distributions. The Normalized Power Spectrum (NPS) is defined in Eq. 2.20.

$$\mathrm{NPS}_z(f) = \frac{2}{N\sigma^2}\mathrm{PS}_z(f) \tag{2.20}$$

As previously defined, TFDs make it possible to isolate the energy distribution in different time intervals. By slicing the TFD of a non-stationary signal (i.e. fixing the time coordinate) it is possible to evaluate the instantaneous spectra of the signal. By using an appropriate resolution in time it is therefore possible to render the signals stationary in a single interval, and treat them as such. In particular, the DFT can be considered a slice of the DSTFT, and the PS a slice of the spectrogram. Overall then, time-frequency analysis can be reduced to the frequency analysis of stationary signals.

2.3 Development of Signal Processing Routines

Given the widespread interest on the estimation of the parameters of signals, multiple approaches and algorithms exist to tackle the non-linearities and provide accurate estimations [Candan, 2011, Fan et al., 2015, Fan and Qi, 2018, Serbes, 2018, Chen et al., 2020, Li et al., 2021, Mou et al., 2021, Liu et al., 2022]. With regard to the generation of radiometric observables, the most important estimation to be computed is the frequency of the signal (average or instantaneous). In general, the goodness of estimation of the other parameters depends on how accurate the signal frequency can be computed. As a general discriminant, frequency estimation methods are divided in time domain and frequency domain estimators. Time domain estimators rely on filters to estimate the instantaneous phase of signals and compute its derivative. Such methods are called phase-locked loops (PLL). Frequency estimation through PLL algorithms provides the most accurate results [Buccino et al., 2018, Buccino et al., 2022], but their performance is usually degraded by the non-stationarity of signals and fluctuations in the signal's phase and amplitude. This last phenomenon can often be observed during radio science experiments, especially when the signal passes through the interplanetary plasma. As calibrations are performed only after the observables are generated and the frequency has been estimated, it is not possible to compensate these phenomena on the raw data before processing. Frequency domain estimators, on the contrary, rely on the Fourier transform to analyze the energy distribution of the signal in the frequency domain. Their robustness to noise and applicability for a complete signal characterization make them a solid general purpose choice for digital signal processing.

In consideration of this, a general-purpose signal processing algorithm developed with the aim of generating radiometric observables from raw data is presented. The method is based on spectral interpolation, and was adapted from Brent's minimization method [Brent, 2013]. As this estimation algorithm provides the local extremum of a unimodal function, it requires the power spectrum of a stationary or semi-stationary signal as input. The original implementation of this method is attributed to Tortora et Al. [Tortora et al., 2004]

for the frequency estimation of the downlink signal from Cassini during the 2002 Solar Conjunction Experiment. During its employment, this spectral-based method demonstrated high robustness to group phase delay and amplitude oscillations of the downlink signal, which were caused by interplanetary plasma and solar wind. From its first implementation, this method was better characterized and improved to maximize the accuracy of estimation using radiometric data [Togni et al., 2021].

The concept of operations is to perform a first coarse frequency estimation using a Maximum Likelihood Estimator (MLE) (i.e. the PS or NPS) to provide a first guess of the signal's frequency. Then, a fine estimation algorithm interpolates the NPS to compute the residual frequency. The frequency estimation is then obtained by addition of both. The coarse estimation is obtained by maximization of the NPS (Eq. 2.21) of a signal z_m padded to M samples.

$$k^{(c)} = \text{argmax}(S_k(z_m)) \tag{2.21}$$

Where $k^{(c)}$ is the index associated to the estimated coarse signal frequency $\hat{f}_z^{(c)}$. This estimation will always be a multiple of the fundamental frequency of the NPS, as defined in Eq. 2.22.

$$f^{(c)} \in \left\{ \frac{2k - M}{2M} \right\}, k = \{0, 1, ..., M-1\} \tag{2.22}$$

If the SNR of the signal is higher than the SNR breakdown threshold, and therefore the probability of detection is 100%, $\hat{f}_z^{(c)}$ is the best estimate of the signal's frequency f_z using a MLE. From the coarse estimation, the real signal frequency is obtained from Eq. 2.23.

$$f_z = \hat{f}_z^{(c)} + \frac{\delta}{M} \tag{2.23}$$

Where δ/M is the residual frequency, with $\delta \in [-0.5, 0.5]$. Essentially, Eq. 2.23 defines the maximum error in the frequency estimation by using the NPS with no spectral interpolation, as its resolution in frequency is limited by the FFT's resolution, reportedly $1/M$.

The MSE of the developed algorithm in the asymptotic, threshold, and no-information regions frequency estimation can be modelled as in Eq. 2.24. This error model assumes the estimator is optimal, but simulations (Fig. 2.9, 2.14, 2.15) confirm the applicability of this model to the proposed algorithm.

$$\text{Var} = (1-p)\frac{6}{(2\pi T_s)^2 N(N^2-1)\rho} + \frac{p}{12T_s^2} \tag{2.24}$$

With p the probability of a correct estimation. The algorithm developed is characterized by a superlinear order of convergence with a rate of 1.325, and provides an unbiased estimate of the signal's frequency, as the search interval is halved and re-centered at every step. Each iteration i of the fine estimation is defined by a tuple of the three spectrum amplitudes $\left\{S_-^{(i)}, S_0^{(i)}, S_+^{(i)}\right\}$ at the frequencies $\left\{\hat{f}_z^{(i)} - \Delta_i, \hat{f}_z^{(i)}, \hat{f}_z^{(i)} + \Delta_i\right\}$, where

$\Delta_i = 1/(2^{i-1}M)$ is the convergence interval at the i^{th} iteration. The target of the fine estimation is therefore to solve the set of equations defined in Eq. 2.25 for the coefficients a,b, and c.

$$\begin{cases} S_-^{(i)} = a\left(\hat{f}_z^{(i)} - \Delta_i\right)^2 + b\left(\hat{f}_z^{(i)} - \Delta_i\right) + c \\ S_0^{(i)} = a\left(\hat{f}_z^{(i)}\right)^2 + b\left(\hat{f}_z^{(i)}\right) + c \\ S_+^{(i)} = a\left(\hat{f}_z^{(i)} + \Delta_i\right)^2 + b\left(\hat{f}_z^{(i)} + \Delta_i\right) + c \end{cases} \tag{2.25}$$

Eq. 2.25 is linear in the three unknowns a, b, c, and can be solved to find the new estimation $\hat{f}_z^{(i+1)}$ as the peak of the interpolating parabola. Eq. 2.26 provides the numerical solution of the local maximum found by interpolating through the 3 DFT points considered.

$$\hat{f}_z^{(i+1)} = \hat{f}_z^{(i)} - \frac{1}{2}\frac{\Delta_i^2\left(S_0^{(i)} - S_+^{(i)}\right) - \Delta_i^2\left(S_0^{(i)} - S_+^{(i)}\right)}{\Delta_i\left(S_0^{(i)} - S_+^{(i)}\right) + \Delta_i\left(S_0^{(i)} - S_+^{(i)}\right)} \tag{2.26}$$

The pseudocode of the routine developed is provided in Table 2.1.

Table 2.1: Pseudocode of the proposed algorithm.

Compute z_m with an arbitrary zeropadding ratio $Z = M - N \geq 0$.
Compute the PS or NPS of z_m.
Perform the coarse estimation.
Set $\hat{f}_z^{(i=1)} = \hat{f}_z^{(c)}$ and $\Delta_{i=1} = 1/M$.
For the number of iterations i:
Compute $\left\{S_-^{(i)}, S_0^{(i)}, S_+^{(i)}\right\}$ at the frequencies $\left\{\hat{f}_z^{(i)} - \Delta_i, \hat{f}_z^{(i)}, \hat{f}_z^{(i)} + \Delta_i\right\}$.
Estimate $\hat{f}_z^{(i+1)}$.
Set $\Delta_{i+1} = \Delta_i/2$.

As the routine is used on radiometric data that can span hours, the condition of stationarity cannot be guaranteed. In addition, the generation of observables is usually performed at fixed count times τ_c (1 second, 60 seconds). The non-stationarity of signals is addressed by using the STFT to compute the NPS at the interval of interest. In particular, by using a sliding window of a fixed length, the average frequency of the signal in a certain interval can be computed and then mapped to the central epoch of the interval itself. The proposed algorithm only employs a rectangular window, since other windows would reduce the accuracy of frequency estimation. This degradation in accuracy is reported in [Candan, 2015].

While the count time τ_c describes the rate of estimation of frequency, the integration time τ_i defines the number of samples used for each estimation, and therefore the length (in seconds) of the sliding window employed. The integration time that can be used is inversely proportional to the rate of change of the signal's instantaneous frequency, as to make the signal stationary in the time interval considered. In fact, signals with a frequency-rate are characterized by a smeared main lobe in the power spectrum. This

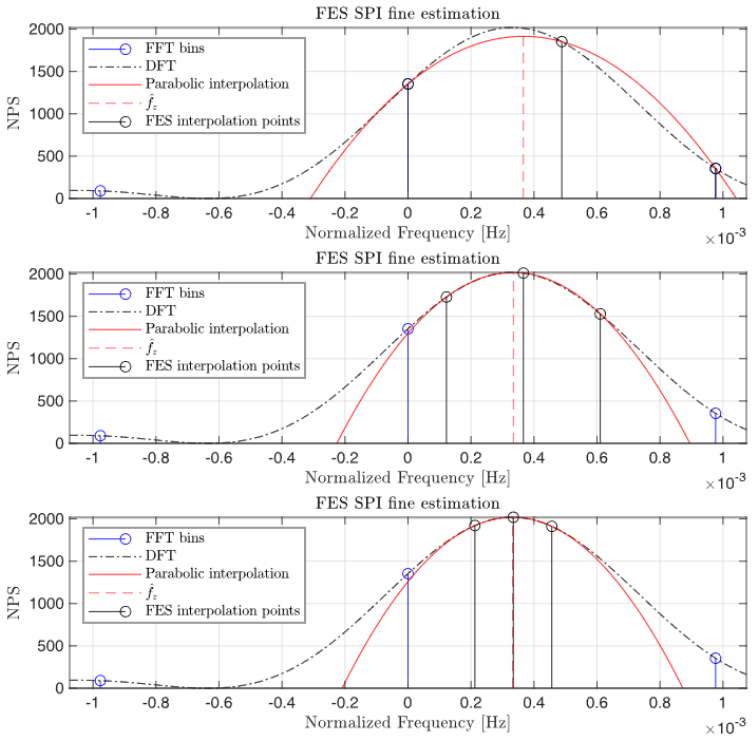

Figure 2.6: Frequency estimation iterations of the algorithm developed. Top: First iteration, the convergence interval is the same as the FFT resolution $1/M$, and the first estimation is given as the analytical peak of the interpolating parabola. Middle: Second iteration, the convergence interval is halved $1/2M$ and a new parabola is fitted through the new three points. Bottom: Third estimation, the convergence interval is halved again $1/4M$ and the frequency estimation becomes more accurate.

phenomenon makes the NPS a non-unimodal function around its peak, making it not possible to converge to the correct average frequency with the developed signal processing routine.

The minimum integration time that should be used depends on the SNR of the signal, in order to guarantee both a correct signal detection and on the required rate of frequency estimation. Conversely, the maximum integration time chosen to have the algorithm converge to a correct estimation depends on the shape of the spectrum generated: spectral interpolation is performed using Successive Parabolic Interpolations (SPI), which converge to the local maxima or minima of a function that is unimodal inside of a prescribed interval. The shape of the main lobe of the power spectrum is a unimodal function only if the variation in the instantaneous frequency in the integration time is limited. In consideration of this, the maximum integration time admissible is defined in Eq. 2.14. Further increases in the integration time split the main lobe into two different lobes and make estimations through the developed routine biased.

2.3.1 Simulations and Performance Validation

The performance of spectrum-based frequency estimators is defined using the estimation bias and the variance that can be reached by the algorithm, provided that the coarse

estimation outputs a correct rough estimate. The analysis of the estimation bias of the developed algorithm is carried out by evaluation of its estimation error $|\hat{f}_z - f_z|$ under different conditions of normalized residual frequency δ, which is the difference between the coarse estimation frequency and the signal frequency. Fig. 2.7 shows the results of simulating a signal with a variable residual frequency between $[-1/2, 1/2]$ and no noise. As the signal frequency is normalized, there is no dependency on the sampling frequency, or the number of samples employed.

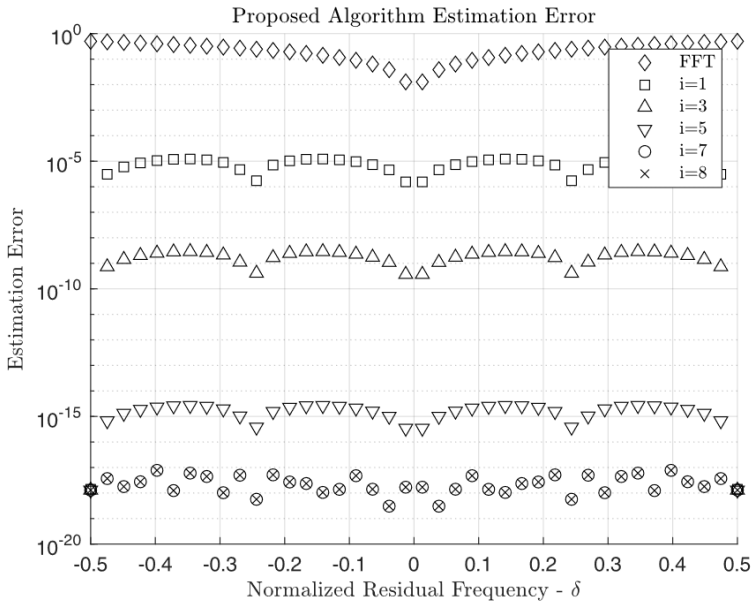

Figure 2.7: Frequency estimation error of a deterministic signal with no noise using the FFT and the developed algorithm at different iterations i.

The estimation accuracy of the NPS is limited by the spectral resolution of the FFT, and as seen in Fig. 2.7, the error in the estimation without interpolation is equal to $|\delta|$. As expected by the interpolation procedure, the estimation error depends on the residual frequency and is 0 when $\delta = \pm 0.25$ $\delta = \pm 0.5$. For any other value of δ, the estimation error at the first iteration of the proposed routine is at least three orders of magnitude lower than the one obtained using the FFT and the NPS. As the number of iterations increase, the estimation error decreases rapidly, and stabilizes around 10^{-18} at iteration number 7. While the estimation error does not provide direct information on the bias of the estimator, it can be used to evaluate the number of iterations required to reach convergence. In addition, in consideration of the estimation error being comparable to the double precision machine epsilon during the simulations, the residual inaccuracies can be considered caused by numerical approximation, and not by an estimation bias of the proposed algorithm.

The variance of estimation must be characterized from a statistical approach due to the stochastic nature of noise. To do so, the MSE metric was used. The use of this accuracy metric was chosen to perform a direct comparison to the theoretical minimum variance of estimation, given by the CRLB. Fig. 2.8 shows the MSE of the estimations compared to the theoretical CRLB. The results are obtained by performing estimations on

10^6 different realizations of signals, changing the number of samples N considered and SNR values. For each realization, a random residual frequency $\delta \in [-0.5, 0.5]$ and initial phase $\theta_0 = [-\pi, \pi]$ are used to randomize the process. For each signal length considered and value of SNR, the FES consistently reaches the CRLB asymptotically. Since the MSE of estimation incorporates both the variance and the bias of the estimator and experimentally MSE≈CRLB, these results confirm the unbiasedness of the proposed algorithm, as well as suggesting it being an optimal estimator independently from the number of samples N, as long as the SNR is higher than the SNR breakdown threshold.

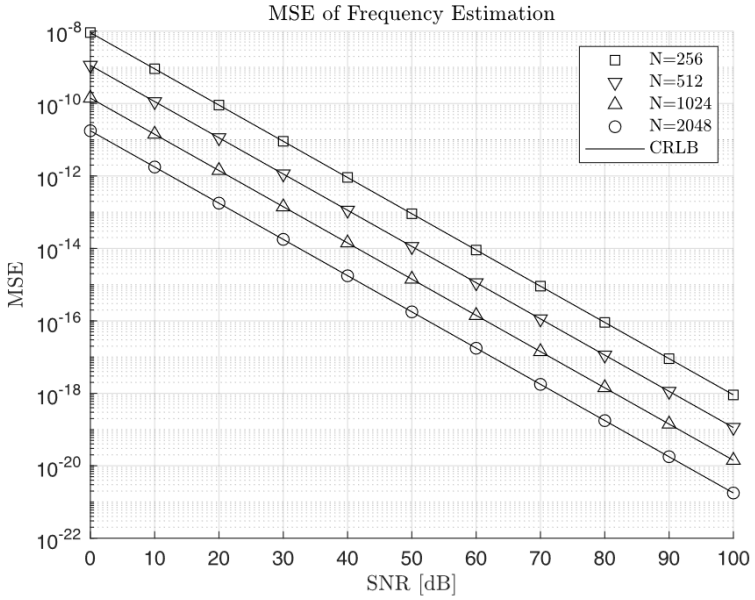

Figure 2.8: Mean squared error of estimation using the routine (i=7) for different number of samples N and SNR. Number of simulations: 10^6.

As the SNR falls below the SNR breakdown threshold, the MSE of the algorithm cannot be described by Eq. 8 anymore, but it must consider the presence of outliers, as reported in Eq. 26. Fig. 9 shows the accuracy of estimation of the estimator below the SNR breakdown threshold, where the MSE departs quickly from the theoretical value described by the CRLB. As the SNR falls below the no-information threshold, the probability of outliers becomes 1 and the MSE tends asymptotically to 112 for any value of N or sampling frequency, in consideration of the normalization of frequency employed.

Fig. 2.9 additionally shows experimentally how the SNR breakdown threshold decreases as more samples are employed for the estimation, as expected from previous studies [Forster et al., 2004, Serbes and Qaraqe, 2022, Athley, 2002, Quinn and Kootsookos, 1994, Steinhardt and Bretherton, 1985].

Fig. 2.10 depicts the comparative performance of the proposed algorithm with different zeropadding ratios to that of other accurate frequency estimation algorithms. The results have been obtained by simulation of 10^6 signals of length N=1024. The choice of performing a high number of estimations is defined in consideration of the much different contributions to the MSE of correct or incorrect estimations, giving it a high sensibility to the number of outliers obtained, especially around the SNR breakdown threshold.

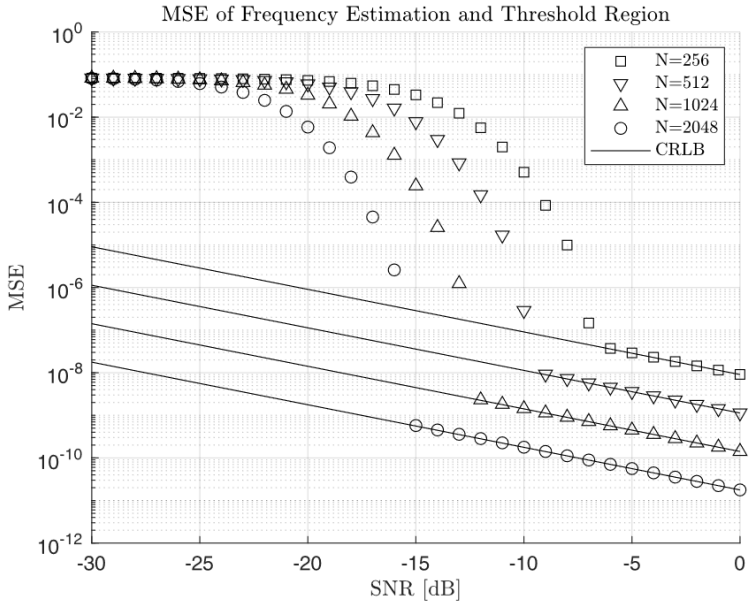

Figure 2.9: Mean squared error of estimation using the FES (i=7) for different number of samples N and SNR above and below the SNR breakdown threshold. Number of simulations: 10^6.

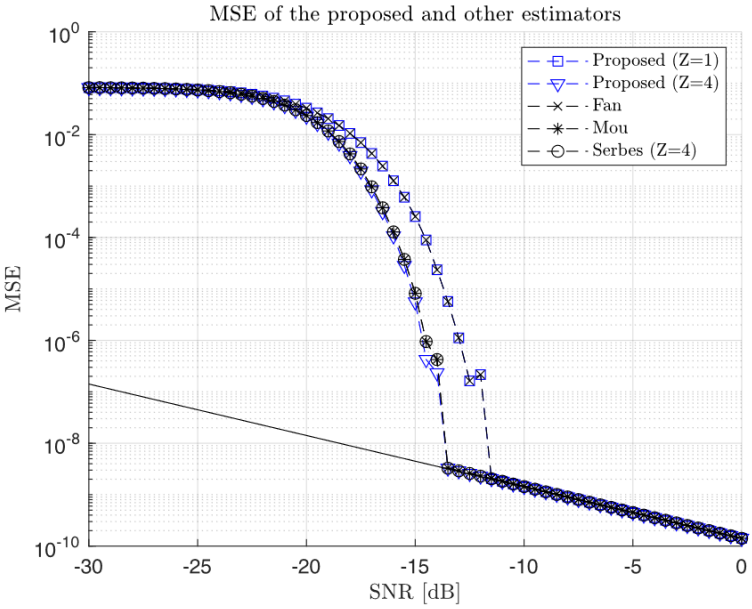

Figure 2.10: Estimated MSE of the proposed algorithm and other estimators [Fan and Qi, 2018, Mou et al., 2021, Serbes, 2021]. Number of simulations: 10^6. Number of samples employed: 1024.

Fig. 2.10 demonstrates how the algorithms where zeropadding is applicable have a lower SNR breakdown threshold of ≈2 dB with respect to estimators with no zeropadding. This will be better discussed in section 2.5. Additionally, Fig. 2.12 reports the variance of estimation of the proposed algorithm is one of the lowest possible and is closer to the CRLB than other estimators.

Fig. 2.12 presents the ratio between the MSE and the CRLB of the aforementioned estimators at different SNR values. As expected, an increase in the zeropadding ratio reduces

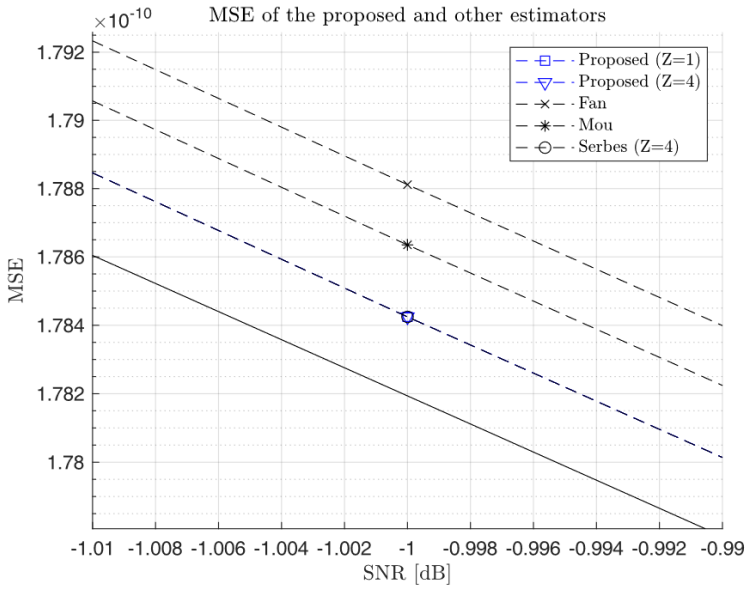

Figure 2.11: Estimated MSE of the proposed algorithm and other estimators (details) [Fan and Qi, 2018, Mou et al., 2021, Serbes, 2021]. Number of simulations: 10^6. Number of samples employed: 1024.

the SNR breakdown threshold, while it does not affect the final accuracy of estimation, which is dependent on the fine estimation step employed.

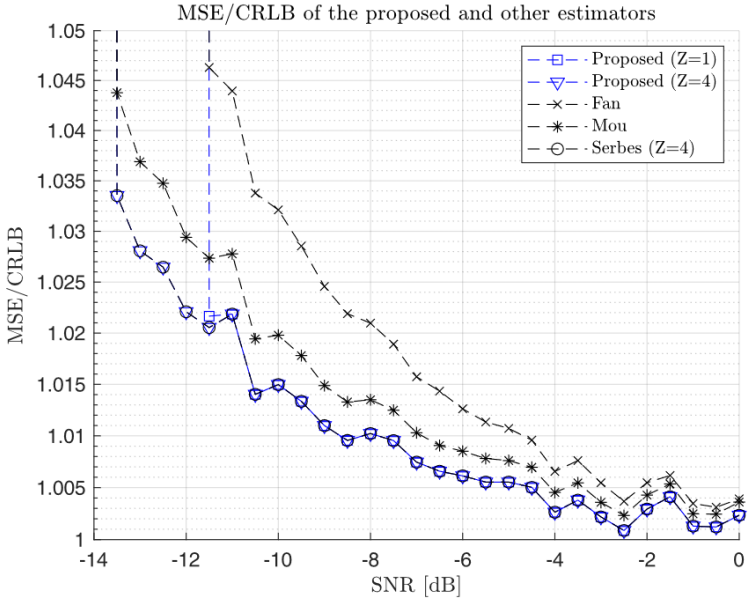

Figure 2.12: Ratio of the MSE of the proposed algorithm and other estimators over the CRLB. Number of simulations: 10^6. Number of samples employed: 1024.

The proposed algorithm and the one from [Serbes, 2021] provide the most accurate estimations at any SNR value. In particular, when both are padded with the same ratio, the accuracy of frequency estimation is almost indistinguishable at all SNR values. To better visualize their performance, in Fig. 2.13 the ratio between the MSE obtained through other estimators and the proposed algorithm is shown. As all ratios are ≥ 1 for

any SNR value considered, the plot confirms the hypothesis of the proposed estimator having a wider initial convergence interval than analytical estimators, as its differential MSE is the lowest around the SNR breakdown threshold, when slight variations in p affect the overall accuracy the most.

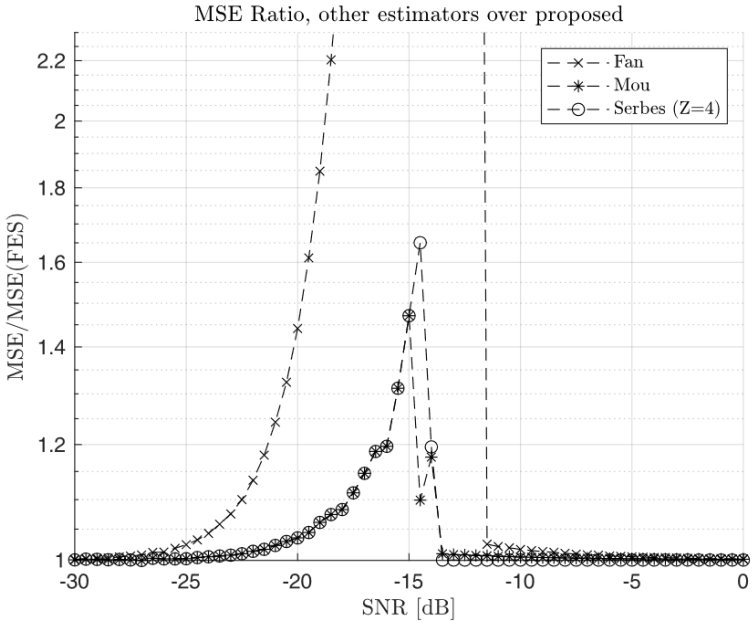

Figure 2.13: Ratio of the MSE of other estimators over the MSE of the proposed algorithm. Number of simulations: 10^6. Number of samples considered: 1024.

2.4 Cramér-Rao Lower Bounds and estimation performance

The estimations of a signal's parameters are characterized by a minimum uncertainty, which is proportional to the information content in the signal (i.e. the time-bandwidth product) and its quality (i.e. the SNR). The CRLB of these parameters (Amplitude, frequency, initial phase) is obtained through inversion of the Fisher's information matrix. A detailed description of the calculations is found in [Rife and Boorstyn, 1974]. An estimator is said to be optimal if the variance of its estimation tends asymptotically to the CRLB of the parameter to be computed.

The CRLB for the estimated amplitude of a signal $\hat{A}$ is defined in Eq. 2.27.

$$\mathrm{CRLB}(\hat{A}) = \frac{\sigma^2}{N} \propto \frac{1}{\rho N} \tag{2.27}$$

Where ρ is the SNR of the signal, N the number of samples considered, and σ^2 the variance of the Random Variable (RV) defining the noise process. Fig. 2.14 visualizes both the CRLB and the estimation variance of the amplitude of a signal with unit power when using the routine developed for signal processing. As is visible, there is a threshold effect around 10 dB where the variance of estimations through spectra diverges from the expected variance. Below the threshold of correct estimation the experimental variance is lower than the one defined by the CRLB. This is justified by the estimation of the

amplitude not being carried out on the correct bin of the NPS, but a random bin where the only energy contribution is given by noise. The experimental variance is then lower as the variance of the RV associated to noise realizations is always lower than the one of the RV associated to the signal energy in the frequency domain ($\mathrm{Var}(\chi_2^2) < \mathrm{Var}(\chi_2^2(\lambda)) \forall \lambda > 0$).

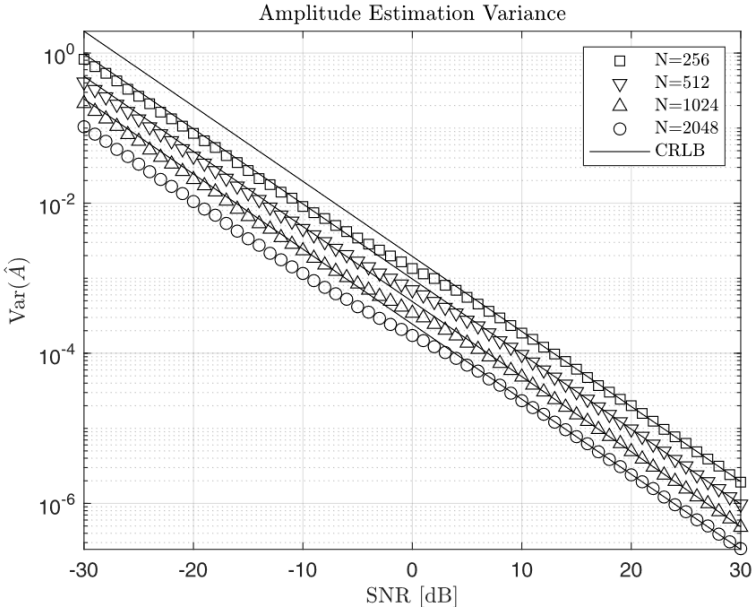

Figure 2.14: Experimental amplitude estimation variance of the proposed estimator and CRLB.

The instantaneous phase of a deterministic signal can be directly estimated as $tan^{-1}(\frac{Q}{I})$. When the signal is at least partially random, such estimation is not correct due to the presence of AWGN noise. In consideration of noise in the form $\nu_c(t) \sim \mathcal{CN}(0, \mathbf{I}\sigma^2)$, the phase of its realizations is random with a uniform distribution in the interval $[-\pi, \pi]$. Therefore, when estimating the phase in the time domain the noise affects the computed phase randomly, and in proportion to the SNR. The computation of the signal phase in the frequency domain is more intuitive, as $\hat{\theta}_0 = tan^{-1}\left(\frac{\mathrm{Im}(\mathbf{X}(f_0)}{\mathrm{Re}(\mathbf{X}(f_0)}\right)$, and by using the estimation of the frequency tone it can be propagated to the requested epoch. Eq. 2.28 shows the CRLB for the estimation of the initial phase when the frequency is known (first equation) or unknown (second equation).

$$\begin{cases} \mathrm{CRLB}(\hat{\theta}_0) = \frac{\sigma^2}{CN} = \frac{1}{2\rho N} \\ \mathrm{CRLB}(\hat{\theta}_0) = \frac{3\left(\frac{t_0^2}{T_s^2}N + \frac{2t_0}{T_s}\frac{N(N-1)}{2} + \frac{N(N-1)(2N-1)}{6}\right)}{\rho N^2(N^2-1)} \end{cases} \tag{2.28}$$

Where t_0 is the epoch of the first sample, and T_s the sampling time. Fig. 2.15 shows the observed variance of estimation and CRLB when employing the developed estimation method. Here, the SNR breakdown threshold is variable with the number of samples N employed, and depends on whether the frequency of the tone can be correctly estimated or not. After falling below the threshold, the phase estimation converges to $\pi^2/3$ when reaching the no-information zone, as expected.

With regard to frequency estimation, Eq. 31 provides the CRLB.

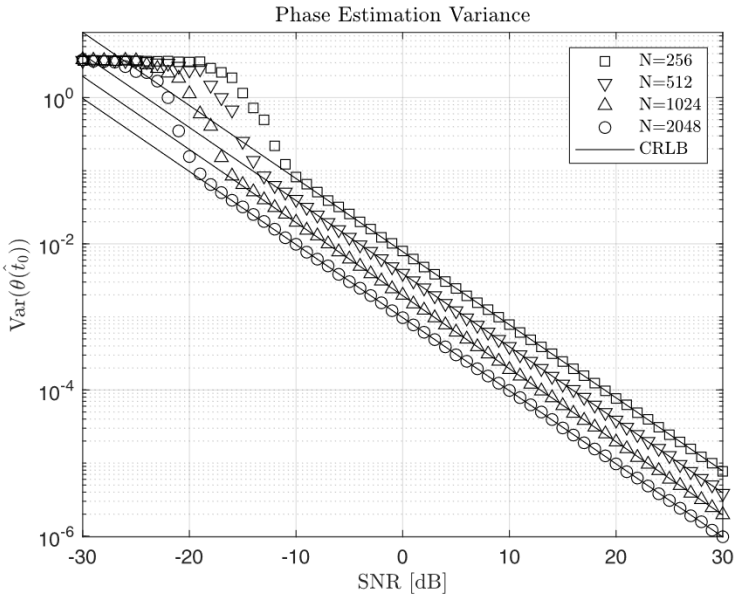

Figure 2.15: Experimental initial phase estimation variance of the proposed estimator and CRLB.

$$\begin{cases} \mathrm{CRLB}(\hat{f}) = \dfrac{\sigma^2}{(2\pi T_s)^2 2C(\frac{t_0^2}{T_s^2}N + \frac{2t_0}{T_s}\frac{N(N-1)}{2} + \frac{N(N-1)(2N-1)}{6})} \\ \mathrm{CRLB}(\hat{f}) = \dfrac{6\sigma^2}{C(2\pi T_s)^2 N(N^2-1)} \end{cases} \tag{2.29}$$

Where N is the number of samples used for the estimation, σ^2 is the variance of AWGN, and t_0 the initial acquisition time of the signal. In Eq. 2.29, the first is valid if the phase is known at the initial acquisition time t_0, and the second if the initial phase is not known.

2.5 Analysis of Detection Thresholds

Incorrect coarse estimations are historically called outliers [Rife and Boorstyn, 1974], and define an initial estimation that does not depend on the signal under analysis, but is random. This phenomenon depends on the energy distribution in the frequency domain. In particular, as the noise density power increases with a reduction in the SNR, the tone to be estimated could be buried in noise. The definition of the three estimation/detection regions depends on the likelihood of this happening.

Given the stochastic nature of random signals, their detectability cannot be estimated deterministically, but only in a statistical sense. This indetermination comes from the fact that the involved parameters are realizations of random processes. The model of signals was introduced in section 2.1. In consideration of it, the random processes that describe the likelihood of its realizations are defined in Table 3.

Table 2.2: Probability distribution functions of RV associated to CAWGN and the modelled random signal.

Random Signal	Probability Distribution Function in the Time Domain
Real(ν_c)	$f(x) = \frac{1}{\sigma\sqrt{2\pi}} exp\left(-\frac{1}{2}\left(\frac{x}{\sigma}\right)^2\right)$
Imag(ν_c)	$f(x) = \frac{1}{\sigma\sqrt{2\pi}} exp\left(-\frac{1}{2}\left(\frac{x}{\sigma}\right)^2\right)$
Abs(ν_c)	$f(x) = \frac{1}{\sigma^2} exp\left(-\frac{x^2}{2\sigma^2}\right)$
Real($z + \nu_c$)	$f(x) = \frac{1}{\sigma\sqrt{2\pi}} exp\left(-\frac{1}{2}\left(\frac{x-A}{\sigma}\right)^2\right)$
Imag($z + \nu_c$)	$f(x) = \frac{1}{\sigma\sqrt{2\pi}} exp\left(-\frac{1}{2}\left(\frac{x-A}{\sigma}\right)^2\right)$
Abs($z + \nu_c$)	$f(x) = \frac{1}{\sigma^2} exp\left(-\frac{x^2+A^2}{2\sigma^2}\right) I_0\left(\frac{xA}{\sigma^2}\right)$

Assuming a signal stationary in the interval considered, in the frequency domain the discourse must account for the energy distribution at different frequency values. To be able to parametrize the random variables, all considerations will be made in the normalized power spectrum. As per theory, the FT of a normal RV is a normal RV, and therefore the real, imaginary and absolute value of noise do not change in a statistical sense. The NPS of noise is a chi-squared distribution with 2 degrees of freedom.

$$\text{NPS}(\nu_c) \sim \chi_2^2 \tag{2.30}$$

$$f_{\chi_2^2}(x) = 1 - exp\left(-\frac{x}{2}\right) \tag{2.31}$$

With regard to the complete signal, the presence of a deterministic signal and noise together make it so the NPS changes in frequency. In particular, the deterministic signal affects the spectrum only at the frequency it is located, while the noise is spread over all the bandwidth. With this in mind, the following is valid for a signal z:

$$\text{NPS}(z) \sim \begin{cases} \chi_2^2, & f \neq f_c \\ \chi_2^2(2N\rho), & f = f_c \end{cases} \tag{2.32}$$

$$f_{\chi_2^2(2N\rho)}(x) = \frac{1}{2} exp\left(-\frac{x + 2N\rho}{2}\right) I_0(\sqrt{2N\rho x}) \tag{2.33}$$

While this is valid for a continuous NPS, for time-limited signals the amplitude of the signal bin is modulated by the FT of the window employed proportionally to the resolution of the FFT. In particular, the following is valid if the signal z has a tone at the frequency $f_c + \Delta f$:

$$\text{NPS}_D(z) = \text{NPS}(z) \times sinc^2(\Delta f) \tag{2.34}$$

With $\Delta f \leq \frac{1}{2M}$ if we consider the normalized frequency. The probability of detection has been characterized in literature through its effect on the MSE of frequency estimation. Rife [Rife and Boorstyn, 1974] originally introduced a predictor for the MSE of frequency estimators (Eq. 2.35).

$$\text{MSE} = (1 - p) \times \frac{1}{12} + p \times \text{CRLB} \tag{2.35}$$

In Eq. 2.35 the probability of detection p is not explicitly computed, but it affects the metric of accuracy as a weighting coefficient. In fact, when $p = 0$ all estimations are outliers, and as the signal does not affect the outcome in any way, the estimation is performed in the no-information region (see Fig. 2.5). The term "outlier" is first introduced in [Rife and Boorstyn, 1974] to define an estimation characterized by an initial guess out of the interval of local convergence of the estimation method.

In Eq. 2.35, the first term defines the contribution of outliers to the MSE of estimation of frequency. The constant term 1/12 is given by the variance of a uniform distribution over the frequency bandwidth of the signal, since when the signal is buried in noise, the maximum of the NPS has an equal probability of being at any frequency value. The probability of detection is defined explicitly in [Rife and Boorstyn, 1974] (Eq. 2.36), but the alternating factorial terms makes it impossible to compute p directly.

$$p = 1 - \frac{1}{N}\sum_{n=2}^{N}\frac{N!(-1)^n}{(N-n)!n!}exp\left(-N\rho\frac{n-1}{n}\right) \tag{2.36}$$

Further work [Forster et al., 2004, Serbes and Qaraqe, 2022, Athley, 2002, Quinn and Kootsookos, 1994, Steinhardt and Bretherton, 1985] has extended the study of the probability of detection identifying the SNR breakdown threshold: the SNR at which the MSE reaches an arbitrary value over the lower bound, usually in the form of $\alpha\times$CRLB. On the contrary, the SNR no-information threshold is commonly defined in the form $\beta\times 1/12$. While multiple approximating models are available, the most complete one is presented in [Serbes and Qaraqe, 2022] and defines the asymptotically exact probability of estimation of the SNR breakdown threshold and of the SNR no-information threshold for a continuous and complex signal. In Eq. 2.37, $W_1(x)$ defines the Lambert-W function.

$$p = exp(-\frac{N}{2}exp(-\frac{N\rho}{2})) \tag{2.37}$$

$$p_{th} = -\frac{2}{N}W_1\left(-\frac{18(\alpha-1)}{\pi^2N^2(N-1)}\right) + O(N^{-2}log^{-2}N) \tag{2.38}$$

$$p_{ni} = \frac{2}{N}\left(ln\left(\frac{N}{2}\right) - ln(-ln(1-\beta))\right) \tag{2.39}$$

The results from [Serbes and Qaraqe, 2022] (Eq. 2.37-2.39) are valid for a discrete signal, but assume the frequency-domain representation to be continuous, or that the frequency to be estimated is a multiple of the fundamental frequency of the FFT. For a discrete representation (e.g. FFT) with a random tone, the resolution in the frequency domain reduces the probability of estimation and the thresholds. Fig. 2.16 shows the probability of detection computed using Eq. 2.37 and by simulating and comparing realizations (10^9) of chi squared and non-central chi squared random variables.

On the contrary, Fig. 16 shows a comparison between the model defined in Eq. 40 and the simulations (10^9) of spectra (N=1024) with different resolutions and achieved with zeropadding of the original signal. As expected, the difference in frequency between the argument of the maximum of the NPS and the real frequency increases the SNR

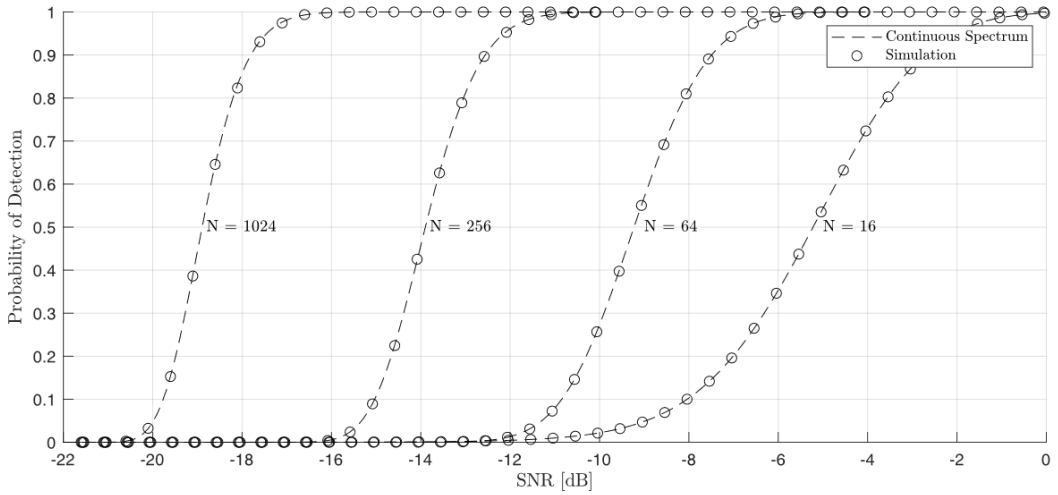

Figure 2.16: Serbes model and experimental probability of detection with no leakage.

thresholds. By defining the zeropadding ratio $Z = M/N$ as the ratio between the length of the signal after zeropadding and the original number of samples, it is possible to define how the effective thresholds tend to the ones in Eq. 2.38 and Eq. 2.39 for $Z \to \infty$.

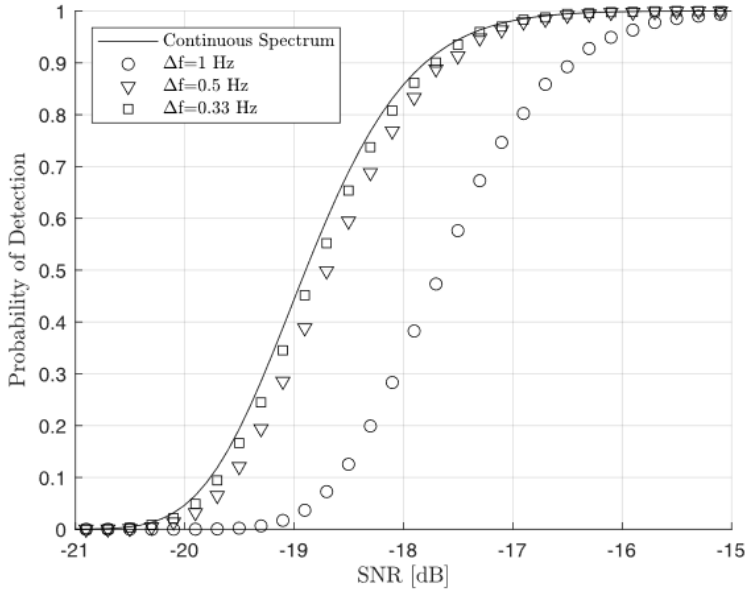

Figure 2.17: Serbes (continuous) model and simulations with different spectral resolutions Δf.

Fig. 2.18 extends the results of Eq. 2.37. The 3D plot shows the analytical probability of detection as defined in [Serbes and Qaraqe, 2022] as a function of N and the Carrier-to-Noise-Density Ratio (P_c/N_0). The passage from the SNR to the P_c/N_0 is immediate, as $P_c/N_0 = \text{SNR} + 10log_{10}(N)$. The choice of this metric as the noise contribution to the signal is done in consideration of its direct effect on the detection threshold. In fact, even though a change in bandwidth affects the total noise power (i.e. changes the SNR), it does not change the noise density and the probability of detection. Fig. 2.19 defines a graphical detection map, where the isolines identify the sets of $(P_c/N_0, N)$ with the same

probability of detection.

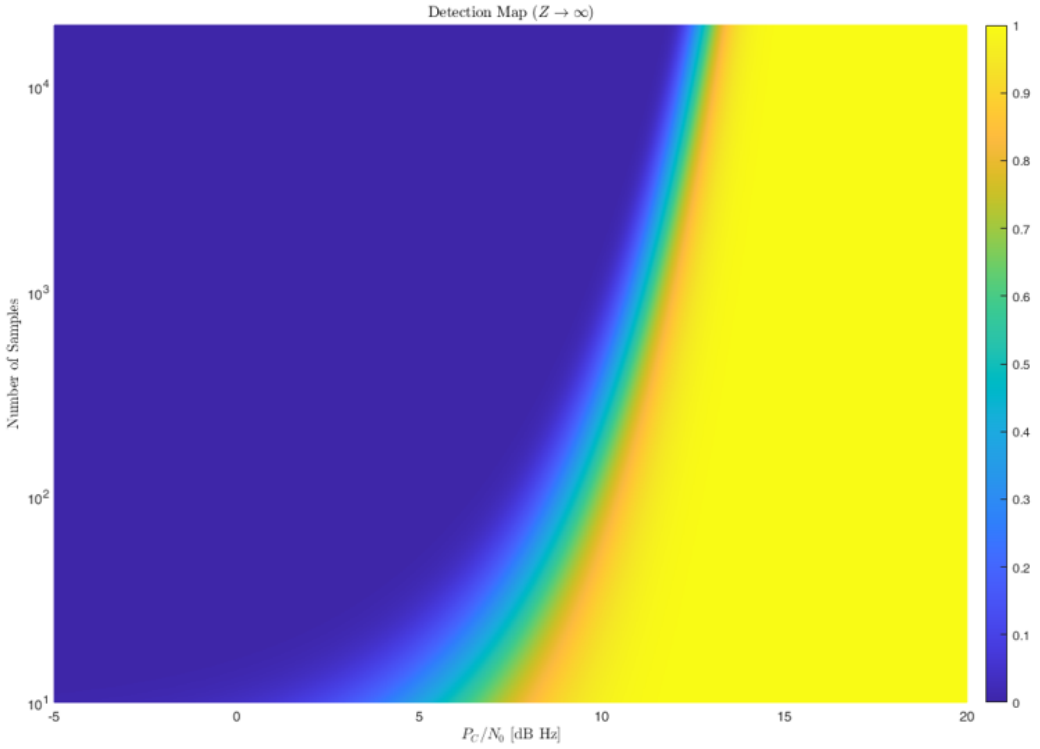

Figure 2.18: Surface plot of probability of detection using the model from [Serbes and Qaraqe, 2022] (Eq. 2.37).

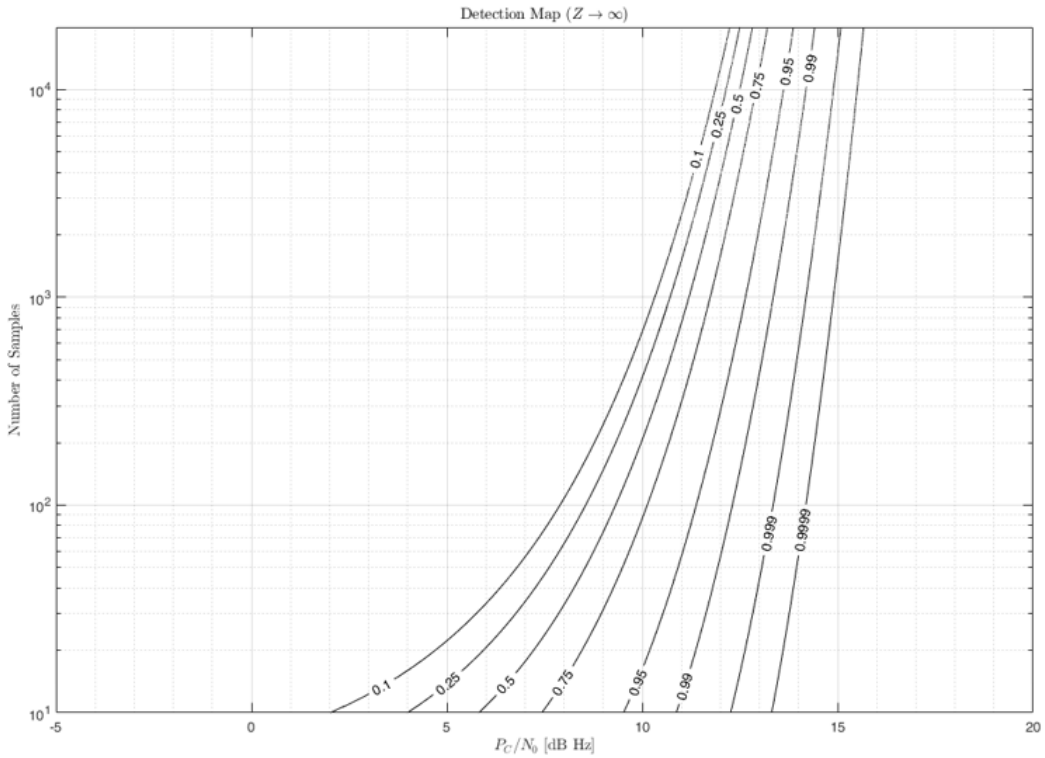

Figure 2.19: Detection map of the model from [Serbes and Qaraqe, 2022] (Eq. 2.37)

When using the NPS to perform detection, the signal is detected when the bin of the

NPS is higher than all other bins. The probability of this event is computed by integrating the probability density functions of the random variables to be compared. The problem is analytically defined in Eq. 2.40, and yields the result shown in Eq. 2.41.

$$p = \Pr(\alpha > \beta)^{N-1} = \left[\int_{-\infty}^{\infty} \Pr(\alpha > x)\Pr(\beta = x)dx\right]^{N-1} = \int_{-\infty}^{\infty} F_\alpha(x) f_\beta(x) dx \quad (2.40)$$

Where F and f are the cumulative distribution function of $\alpha = \text{NPS}(f_z)$ and probability density function of $\beta = \text{NPS}(f \neq f_z)$, respectively. Eq. 2.40 has been analytically solved in [Serbes and Qaraqe, 2022], but with the introduction of a discretization in the spectrum, an analytic solution in closed-form cannot be computed anymore. The reasons for these are the following:

- The introduction of the discretization adds a new function to the amplitude of the carrier ($sinc^2(.)$). This function must be inverted to estimate the probability density function of the random variable associated to the real amplitude. As the sinc function is not invertible, any analytic solution computed would be an approximation.
- The amplitude of the signal tone in the frequency domain is characterized by a non-central chi squared random variable, the distribution functions of which depend on the Marcum Q-function and Bessel functions. These functions are generally hard to integrate, and closed-form solutions are available only for specific cases.

In consideration of the previous points, a new model for the probability of detection when employing a discrete NPS is here presented and described (Eq. 2.41).

$$p = exp\left(-\frac{N}{2} exp(-\frac{N\left(\frac{\rho}{\beta} + \delta\right)}{2})\right) \quad (2.41)$$

This new model accounts for the effect of a residual frequency as a shift in the SNR thresholds and a dilation in the shape of the function. Fig. 2.20 shows the result of using Eq. 2.41 to fit realizations at different signal lengths. Given the impossibility of comparing Eq. 2.41 to an analytical result, no model was developed to predict δ and β. Even though their value as function of N can be approximately predicted (e.g. β is a monotonic function due to $p(P_c/N_0) \leq 1 \; \forall P_c/N_0$), no parametric function was developed, in order to avoid overfitting, since no physical principle was clearly identified to describe the variation of the parameters considered.

Finally, Fig. 2.22 and Fig. 2.23 show the detection map at different zeropadding ratios. As discussed, performing zeropadding on the signal under analysis reduces the SNR thresholds. In particular, going from a non-padded signal ($Z = 1$) to a heavily padded one ($Z \to \infty$), the thresholds decrease of about 1.5 dB, providing an increased robustness of estimation in low SNR conditions. As visible in Fig. 2.25, changing Z from 1 to 2 provides the highest offset in the curve $p(P_c/N_0, N)$, while going from 2 to 3 has a much smaller effect. In consideration of this, the ideal condition of $Z \to \infty$ can be

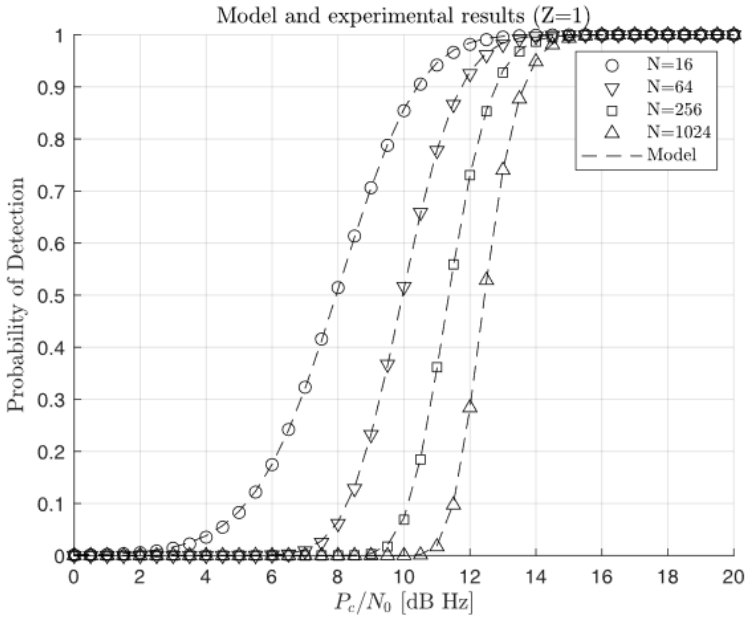

Figure 2.20: Application of the new model to experimental data (Eq. 2.41).

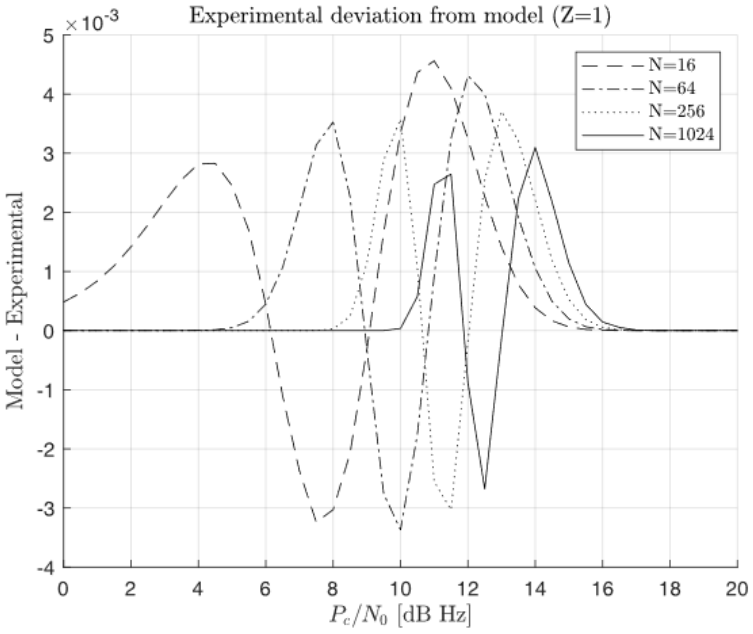

Figure 2.21: Error between experimental data and developed model (Eq. 2.41) at different N.

considered reached with $Z \geq 4$, and assuming ulterior padding has a negligible effect on the detection of a signal from the NPS.

In consideration of the nature of the estimator developed, the algorithm employed can converge to a correct estimation when initialized in a wider range than the single frequency bin of the signal tone. In consideration of this, an extended detection map was developed to include all estimations inside of the main lobe of the signal as correct.

The probability of detection of the main lobe can be accurately described using extreme value theory. In consideration of the stochastic nature of noise and the cardinality

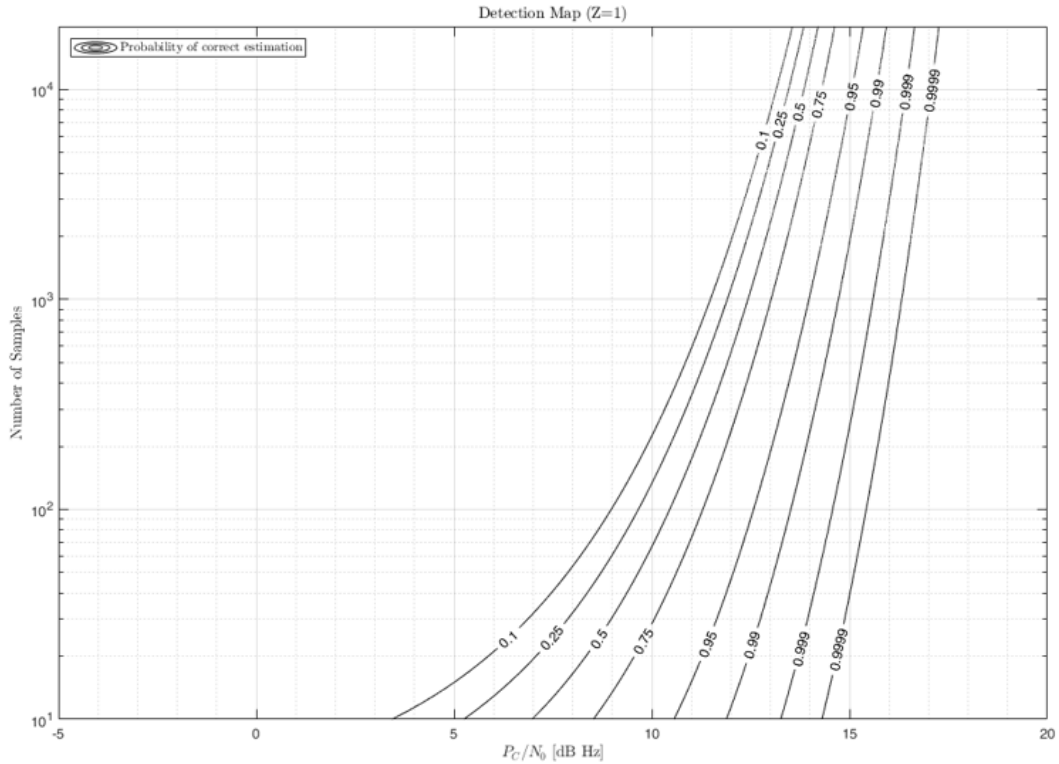

Figure 2.22: Detection map using the developed model (Eq. 2.41) for Z=1.

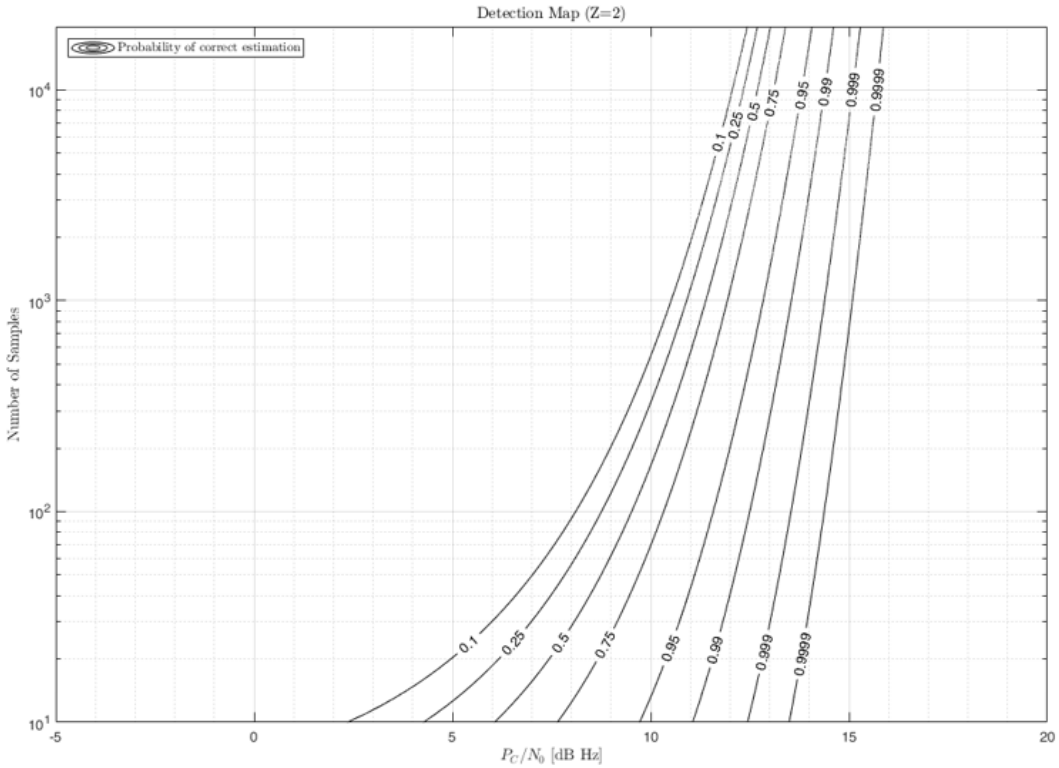

Figure 2.23: Detection map using the developed model (Eq. 2.41) for Z=2.

of the spectral bins associated to it, the probability of detection can be mapped to a characterization of the largest order statistics of noise realizations. Fig. 2.24 shows the finite differences of the experimental (10^6) probability of detection as function of the P_c/N_0. The

model employed to fit the data is the probability distribution function of a generalized extreme value distribution, and defined in Eq. 2.42.

$$f(x) = s\frac{1}{\sigma}exp\left(-\left(1-\xi\frac{x+\mu}{\sigma}\right)^{-\frac{1}{\xi}}\right)\left(1-\xi\frac{x+\mu}{\sigma}\right)^{-1-\frac{1}{xi}} \tag{2.42}$$

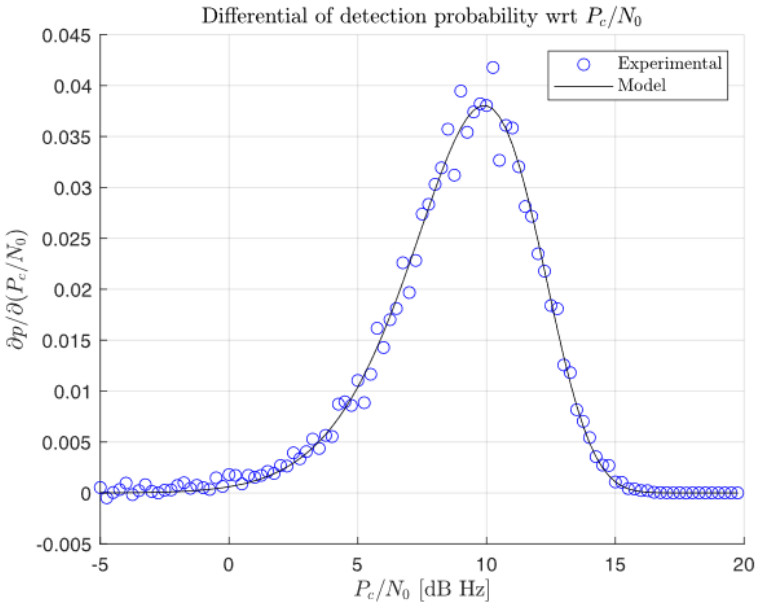

Figure 2.24: Detection map using the developed model (Eq. 2.41) for Z=2.

Where ξ, μ, and σ are the distribution parameters, and s a scale factor. The model used to parametrize the probability of detection consists then in the cumulative distribution function of the random variable described by Eq. 2.42. In other words, it is the integral of Eq. 2.40. Naturally the integration must account for the boundary conditions. To describe the probability of detection, the model function must be less or equal to 1 when the probability of detection is 100%. On the contrary, when in the no-information region, the number of correct estimations must be proportional to the number of bins inside of the main lobe. These boundaries are defined in Eq. 2.43 and Eq. 2.44.

$$\lim_{P_c/N_0\to-\infty} p(P_c/N_0) = \frac{2z+1}{zN}\,\forall N, z \tag{2.43}$$

$$\lim_{P_c/N_0\to\infty} p(P_c/N_0) = 1\,\forall N, z \tag{2.44}$$

In consideration of this, the modelling function becomes:

$$\hat{p}(P_c/N_0) = 1+(K-1)\int_{-\infty}^{P_c/N_0}\frac{1}{\sigma}exp\left(-\left(1-\xi\frac{x+\mu}{\sigma}\right)^{-\frac{1}{\xi}}\right)\left(1-\xi\frac{x+\mu}{\sigma}\right)^{-1-\frac{1}{\xi}}dx \tag{2.45}$$

With $K = (2z+1)/zN$. In Eq. 2.45 the dependency of ξ, μ, and σ from the number of samples N is not shown, but it is highlighted in Fig. 2.25-2.27, where a parametric model is developed to fit their variations with N (Z=1).

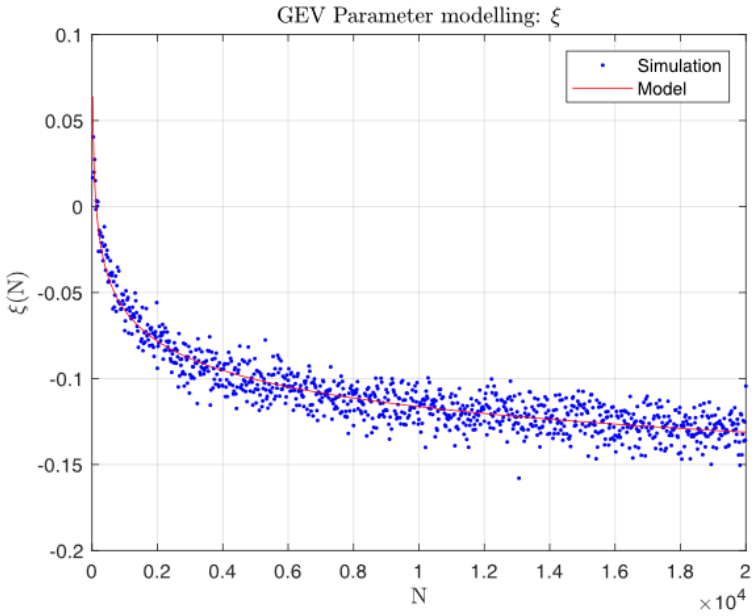

Figure 2.25: Experimental values and model of ξ.

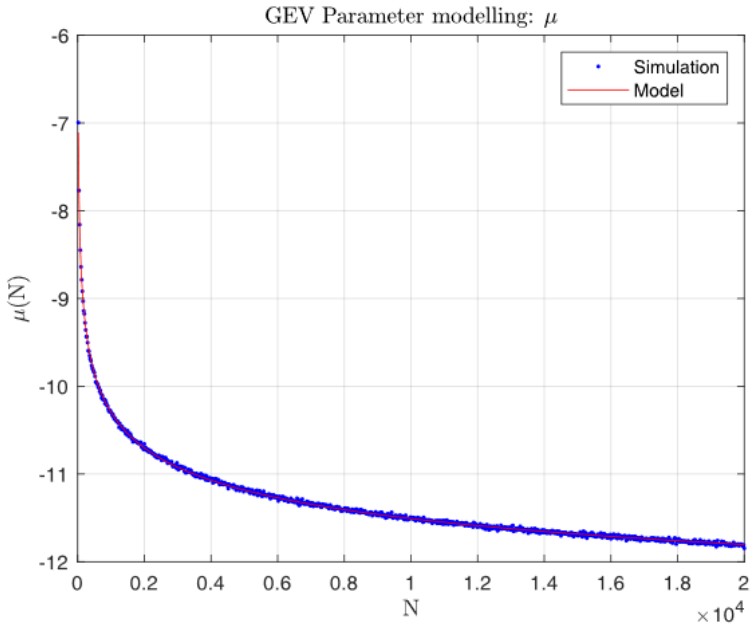

Figure 2.26: Experimental values and model of μ.

Fig. 2.28 and 2.29 show the detection map of the main lobe of a signal for no zeropadding (Z=1) and a high zeropadding ratio (Z=4). Finally, Fig. 2.30 and Fig. 2.31 show the fitness of the developed model to predict the probability of detection, as well as the experimental residuals using different numbers of samples. In particular, for a probability of detection between 0.9 and 1, the maximum divergence of the model from real data is no more than 6×10^{-3}.

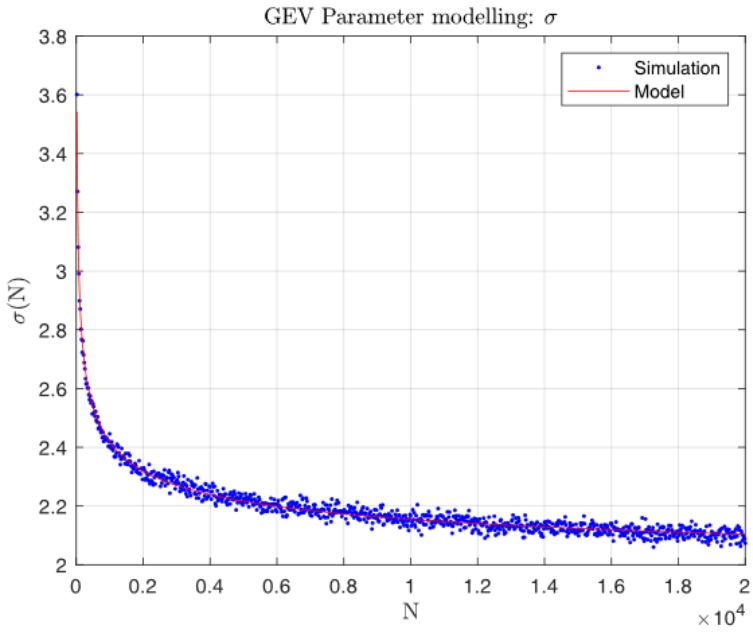

Figure 2.27: Experimental values and model of σ.

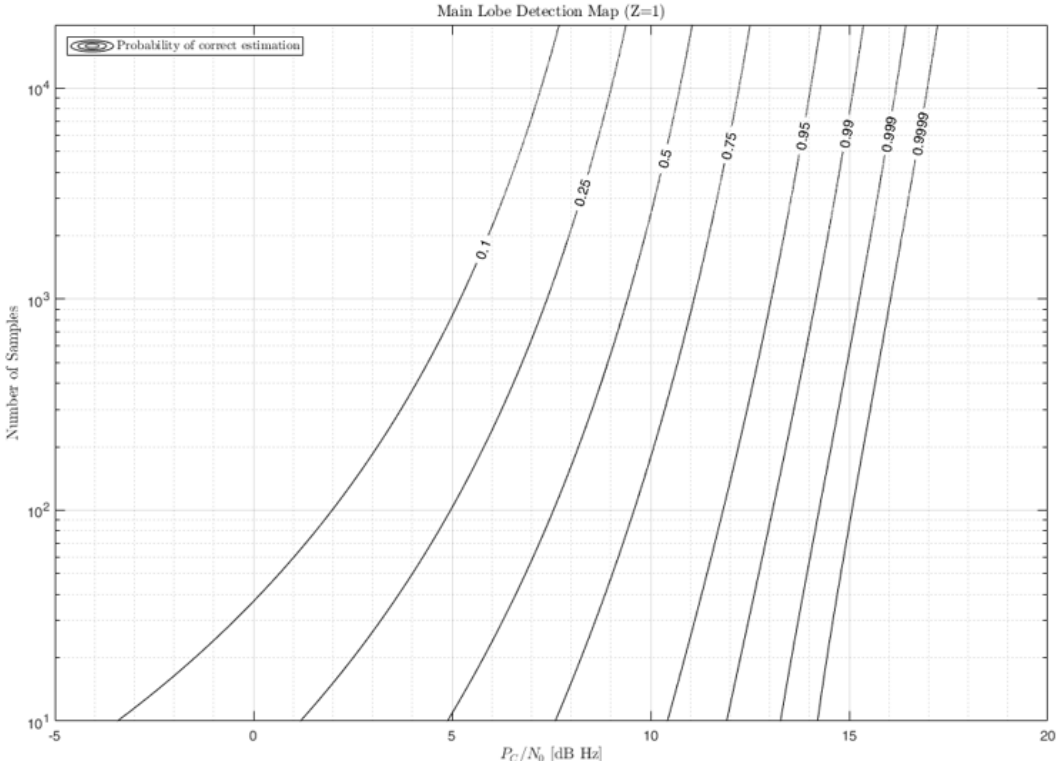

Figure 2.28: Main lobe detection map using the developed model (Eq. 2.45) for Z=1.

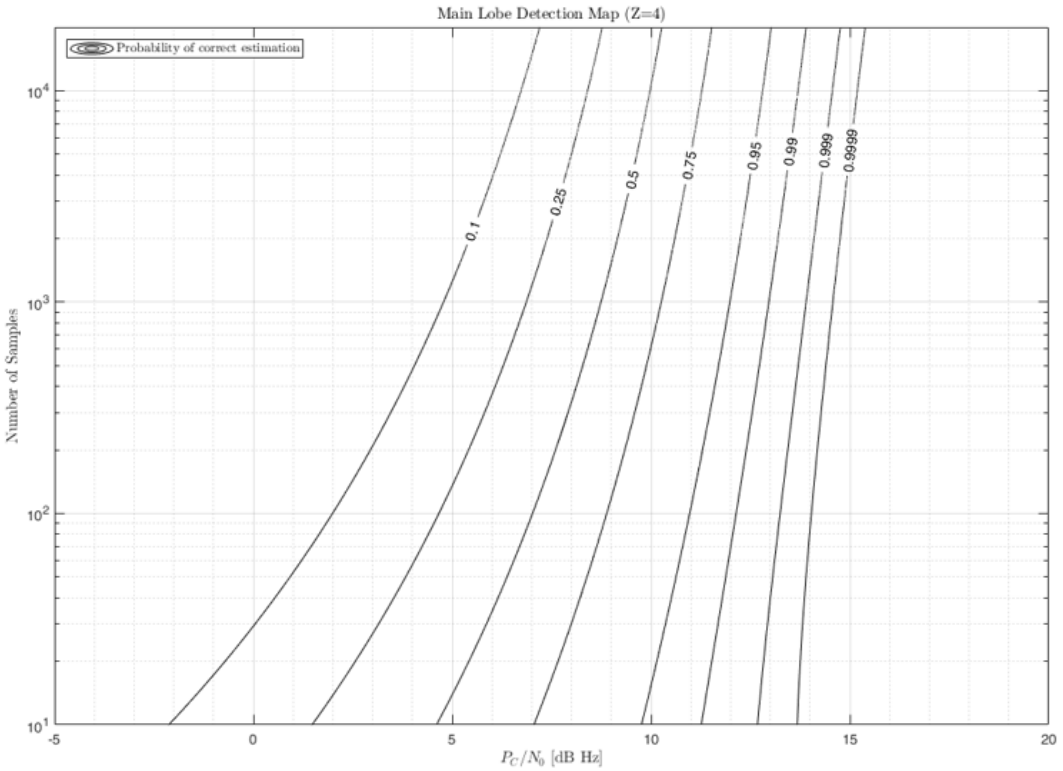

Figure 2.29: Main lobe detection map using the developed model (Eq. 2.45) for Z=4.

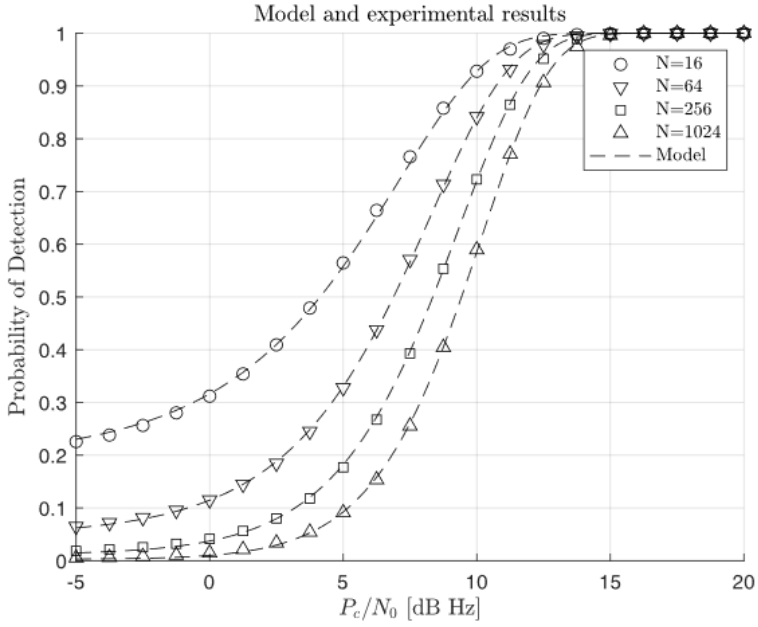

Figure 2.30: Application of the new model to experimental data (Eq. 2.45) at different N.

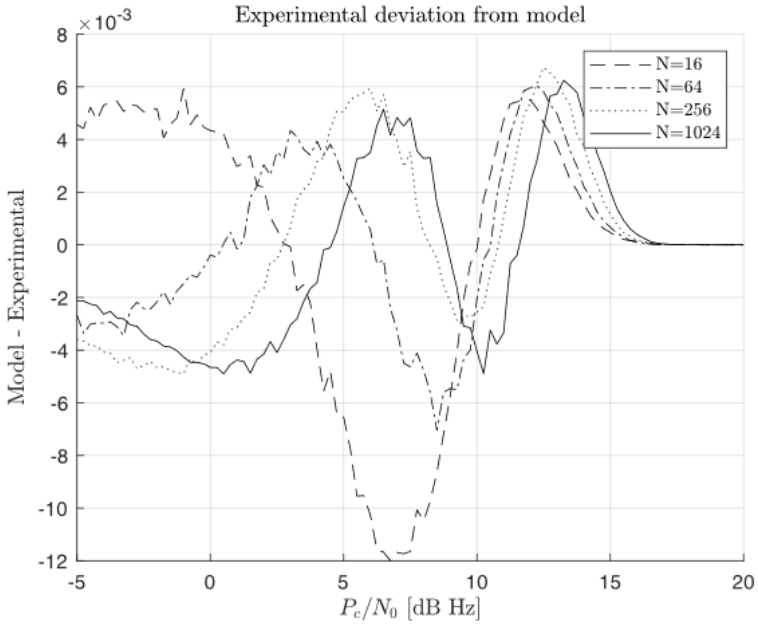

Figure 2.31: Error between experimental data and developed model (Eq. 2.45) at different N.

2.6 Effects on the Generation of Observables

With the frequency estimation algorithm developed it is possible to compute the average frequency in a fixed interval and generate the Doppler observable associated to its central epoch. After computing the average frequency, it is then possible to map the uncertainty in the estimation to the related uncertainty in the range-rate of the spacecraft by considering the transmission frequency [O'Dea and Kinman, 2019]. Under the hypothesis of only thermal noise, Eq. 2.46 defines this relation.

$$\sigma_{\dot{\rho}}^2 = \sigma_f^2 \frac{c}{f_T} \tag{2.46}$$

Table 2.3: Approximate conversion factors for different deep space telecommunication bands.

Carrier Frequency [Hz]	c/f_T [m]
S-Band	0.1363
X-Band	0.0357
Ka-Band	0.0094

In consideration of the limitation on the integration time and the CRLB, Fig. 32 highlights the minimum frequency estimation uncertainty reachable when generating the Doppler observables from raw data. A standard P_c/N_0 of 40 dBHz is assumed. If no frequency rate (on the residual frequency) is present, the integration time does not have an upper limit, as the local spectrum remains unimodal, and the frequency estimation uncertainty is the same as the CRLB. On the contrary, if the residual frequency diverges from a constant value, the target count time must be achieved by averaging successive estimations. Averaging measurements corrupted by AWGN (and therefore uncorrelated), decreases the variance of estimation proportionally to $1/N$, with N the number of measurements averaged. On the contrary, the minimum variance of estimation defined by the CRLB goes with $1/N^3$. Therefore, the employment of an integration time as high as possible is preferred when generating Doppler observables from raw measurements.

An example of the application of this optimization can be found in [Togni et al., 2021], where the proposed algorithm was used to compute the residual frequency from the first closest approach of the spacecraft Juno to Jupiter. A first frequency estimation was performed by using a nominal integration time $\tau_i = 1$ second to estimate the frequency rate of the non-stationary residual signal. Once that was computed, a new ideal integration time of 6 seconds was then used to estimate the average frequencies. This value was chosen as the highest possible integration time allowed by the residual frequency's dynamics of which the target count time (60 seconds) is a multiple. Then, the count time of 60 seconds was achieved by averaging the estimated values. After fitting the received frequency using the orbital model and applying the appropriate conversion factor to estimate the two-way range-rate of the spacecraft, the residuals were analyzed to investigate their quality. Fig. 2.33 shows the residuals of the orbit determination, characterized by a RMS of 0.1 mm/s.

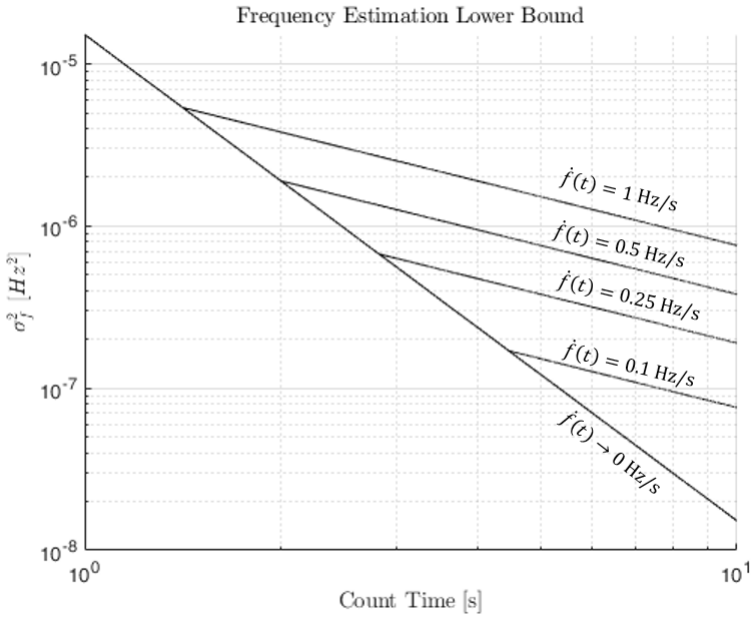

Figure 2.32: Theoretical lowest frequency estimation variance bounds at different signal frequency-rates with $P_c/N_0 = 40$ dBHz.

This value can be compared to the result of previous analyses of this closest approach, which had a standard deviation of 0.106 mm/s [Durante et al., 2020] at 60 seconds of count time using the same dynamical model and data.

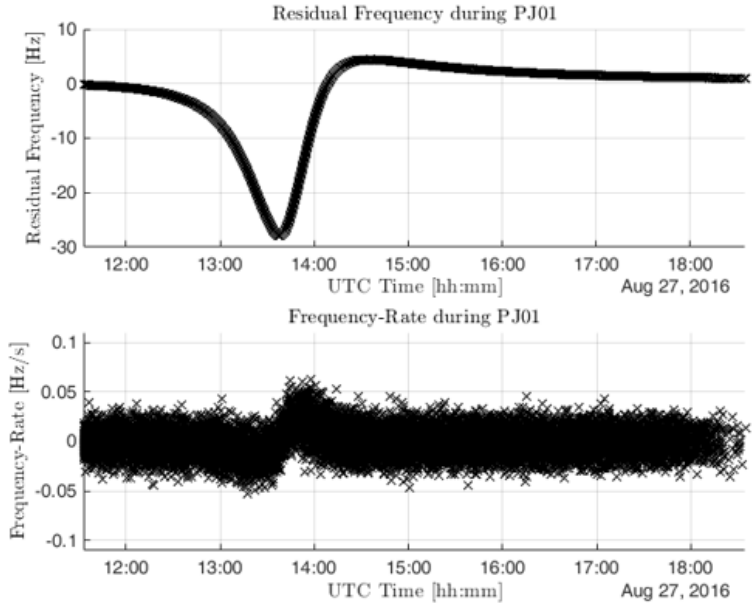

Figure 2.33: Residual frequency and frequency-rate of the Two-Way X/X-Band downlink signal from the Juno spacecraft during PJ01 on August 27, 2016.

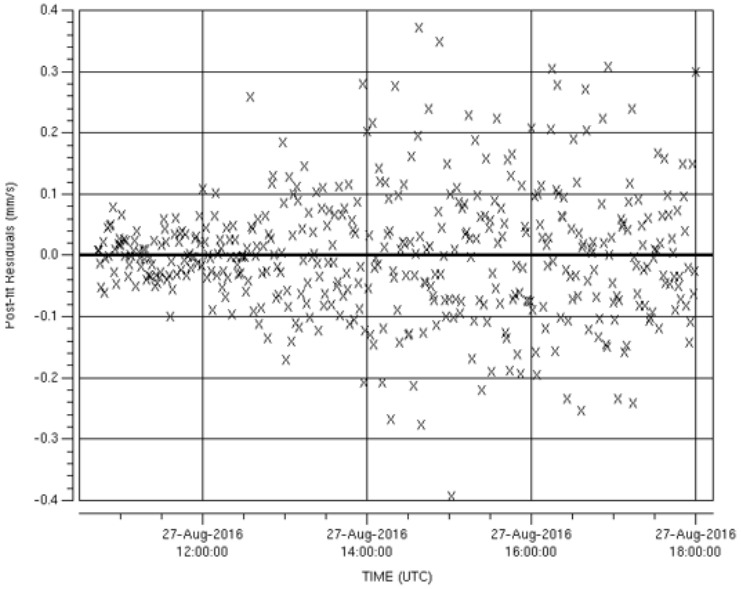

Figure 2.34: Post-fit residuals of the spacecraft Juno PJ01 obtained using the developed routine with $\tau_i = 6$ seconds and $\tau_c = 60$ seconds. RMSE=0.1 mm/s.

Chapter 3

The Sardinia Deep Space Antenna Characterization

Contents

3.1 Introduction

The Sardinia Deep Space Antenna (SDSA), also known as the DSN affiliated node DSS-69, is a ground station managed by the Italian Space Agency (ASI). This key asset is located north of the city of Cagliari on the Sardinia island, west of Italy, and shares some of its infrastructures with the radio-astronomy station known as the Sardinia Radio Telescope (SRT). SDSA had its technical commissioning in 2018 , and since then it's been employed in several tracking activities in deep space. Nevertheless, its radiometric tracking performance for deep space missions has never been fully evaluated or compared to the one of other deep space antennas. In this chapter, the station, its infrastructures and the methodologies employed to perform the characterization of the station's tracking performance are described.

Figure 3.1: The Sardinia Radio Telescope antenna, courtesy of [Valente et al., 2022].

3.2 Complex Architecture

The SDSA station relies on a fully steerable 64 m diameter parabolic radio telescope, which is shared with the SRT station. This infrastructure serves as the interface between the radio-frequency signals received from space, and the receiver dislocated in a shielded room to preserve its robustness to radio-frequency interference. The radio telescope consists of a beam waveguide system to receive the downlink signal at the main reflector and transmit it to the front end located in the pedestal.

With the capability of operating at frequencies spanning a range from 300 MHz to 116 GHz [Valente et al., 2019], the SRT employs an optical quasi-Gregorian configuration. Benefits of this configuration include an increased and tapered illumination efficiency at the main reflector edge, which reduces noise contributions and the level of side lobes [Valente et al., 2019]. Fig. 3.3 reports the optical configuration of the SRT and the details of the beam waveguide employed.

The main reflector (M1) consists of a paraboloid surface composed of 1008 panels (single panel rms: 72 μm). Given the dimensions and the weights at play, the main reflector is equipped with 1116 actuators to compensate for gravitational deformations and thermal loads, which can cause the most gain losses. The M1 compensations are performed using a deformation map, which defines the required positioning of the panels as a function of the pointing elevation. After being reflected by the primary mirror, the radio-frequency signal is then transmitted to M2, an elliptical subreflector that channels the signal towards the beam waveguide. To maximize the radio-frequency performance of the antenna, M2 is

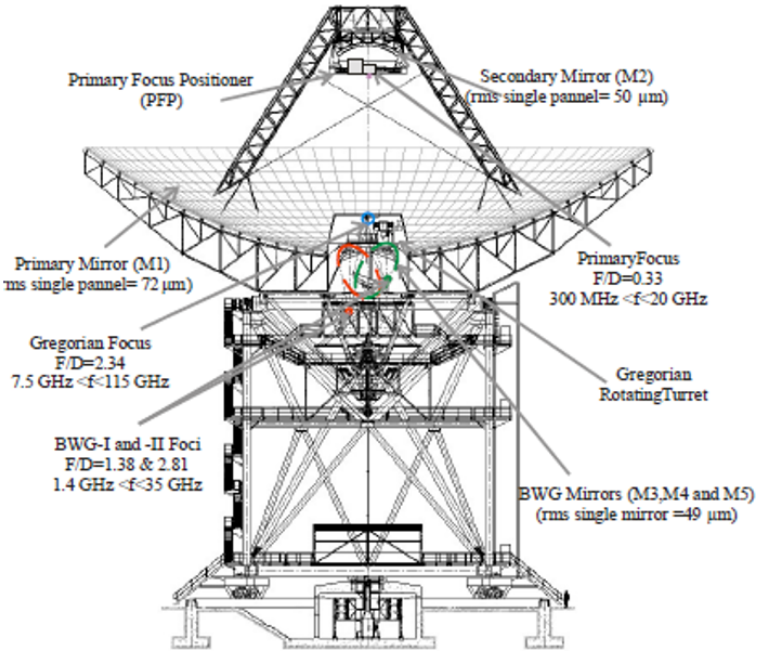

Figure 3.2: Beam waveguide of the semi-gregorian SDSA antenna, courtesy of [Valente et al., 2019].

also equipped with actuators to correct its position due to deformations and maximize its illumination efficiency. The next element in the beam waveguide is the rotating mirror M3, which allows the antenna to select efficiently between different receivers. Ideally, the SRT can have up to 20 receivers installed [Valente et al., 2019], with the slots shared between ASI and the Italian National Institute of Astrophysics (INAF).

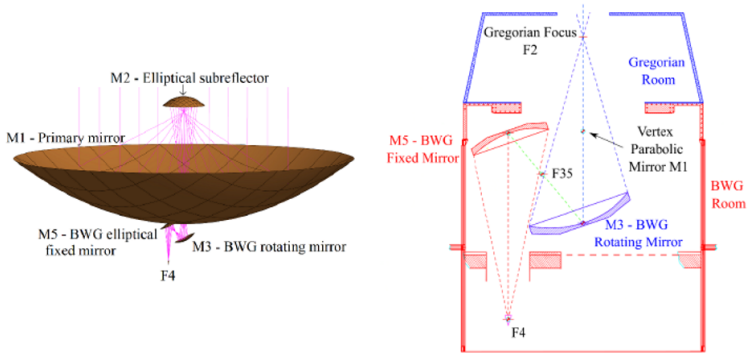

Figure 3.3: Optical configuration of SDSA, courtesy of [Valente et al., 2019].

Table 3.1: Parameters of the mirrors in the SDSA beam waveguide.

Mirror	Size	a	b	F/D
M1	64 m (axially symmetrical)	-	-	0.33
M2	7.9 m (axially symmetrical)	-	-	0.33
M3	3.921 m × 3.702 m	4.7 m	3.8516 m	-
M5	2.994 m × 2.823 m	4.5 m	3.516 m	2.81

The current capabilities of SDSA for deep space tracking are limited to an X-band front end with only downlink capabilities, of which the detailed scheme is provided in Fig. 1.15. Such receiver is employed thanks to a collaboration with NASA JPL, who provided the front end. Fig. 1.15 also describes the signal transmission to the shielded room through an optical link, and the current IFMS receiver, provided by ESA. After the down-conversion to the IF, the signal reaches the back end (IFMS receiver) in an operating band of 28 MHz. As the receiver requires a reference signal, this is provided by the time and frequency laboratory of the station (1 kHz and 5 MHz IRIG-B reference signal with 1 pps).

The processing at the receiver outputs two different streams of information. The closed loop mode of the IFMS performs demodulation and decoding, mostly. To do so, carrier synchronization is required, and therefore through the employment of a PLL, information on the Doppler measurements is also available. The open loop mode outputs baseband in-phase and quadrature components of the signal for successive processing. In particular, the IFMS receiver can be setup to record up to 4 channels with the same bandwidth and different center frequencies. The center frequency can also be appropriately steered to compensate for the Doppler effect on the downlink leg and minimize the residual frequency and required bandwidth. The digitalization in the IFMS is performed at 17.5 MHz, and the final bandwidth is achieved through decimation of the samples. The output of the open loop leg of the receiver is a binary file with the IQ samples and metadata associated to the tracking [IFMS, 2010].

3.3 Station Performance Characterization

The computation of a station's performance for deep space tracking and radio science investigations requires the estimation of the quality and stability of the observables recorded at the site. While a preliminary investigation of the antenna contribution to the transmission error budget is possible, the simulation of such a communication link is of hard implementation due to the contribution of multiple effects to the stability of the downlink frequency. In consideration of this, and the impossibility of performing internal system tests due to the lack of uplink capabilities of SDSA, an acquisition campaign was designed to experimentally test and validate the tracking accuracy of the station. To do this, SDSA was used to perform three-way shadow tracking of the spacecraft Juno with other DSS of the DSN. The choice of using a well-characterized spacecraft such as Juno relies on the availability of models, data, and information on the spacecraft and its state, which make it possible to very accurately model its conditions when transmitting. These tracking activities made it possible to characterize and evaluate the performance of SDSA, especially when different antenna configurations were employed. In particular, the comparison between the characteristics of the residuals at the different stations makes it possible to extrapolate information on bottlenecks in the stability and quality of the transmission link. This can be achieved by using similar tracking configurations and processing algorithms on data from both stations. The end of the acquisition campaign was forced by extra-ordinary maintenance, starting in the second half of June 2021.

3.3.1 The Juno Mission

The Juno mission, part of NASA's New Frontiers Program, was launched on August 5, 2011. The mission was designed to perform nine scientific investigations using eight instruments (Fig. 3.5), as the gravity science experiment relies on telecommunication subsystem on the spacecraft. The Juno spacecraft was launched on August 5, 2011 and entered its science phase around Jupiter on July 4, 2016. Amongst the science objectives of the mission, there is the investigation of Jupiter's interior structure. This will be performed by estimating and computing the gravitational field of the gas giant and the effect of tides caused by the Galilean satellites. Fig. 3.6 shows the highly elliptical polar orbits of Juno, designed to have the closest approach (i.e. perijove) at an altitude below 8000 km and at different longitudes. The prime mission was designed to last 5.07 years with 35 perijoves, and has currently been extended to 77 orbits, with a planned end-of-mission in 2025.

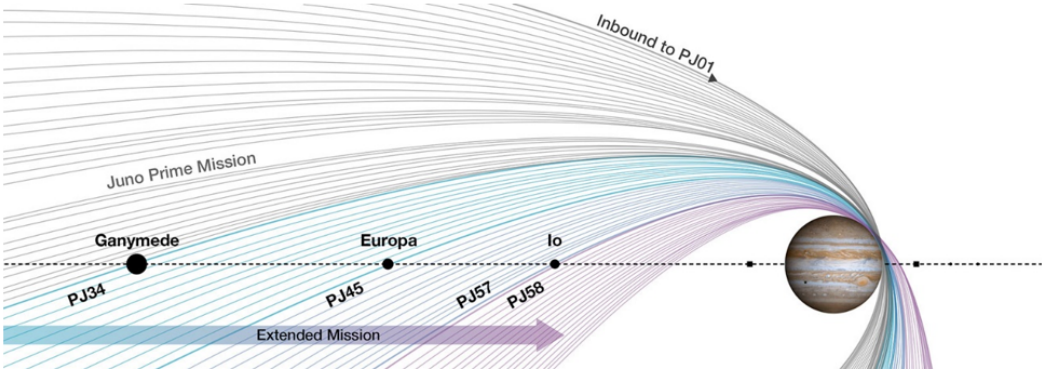

Figure 3.4: Juno nominal and extended mission orbits [NASA/JPL-Caltech/SwRI, 2021]

Fig. 3.6 shows the Juno gravity science instrumentation, which is made up of the space and ground transponders. The spacecraft is equipped with telecommunication hardware capable of performing multi-link transmission, and in particular an X/Ka uplink and X/X/Ka downlink thanks to the Ka-band translator [Asmar et al., 2017]. This transmission link allows the dispersive noise contributions to be calibrated, as it affects the downlink signals proportionally to their carrier's frequency.

Instrument	Institution	Description	Science investigation
Gravity Science (GRAV)	JPL	X- & Ka-band uplink and downlink	Interior structure
Magnetometer (MAG)	GSFC	2 Vector fluxgates (FGM) & 4 co-located star cameras	Interior structure & magnetic dynamo
MicroWave Radiometer (MWR)	JPL	6 wavelengths (1.3–50 cm)	Deep atmosphere sounding & composition
Juno Energetic particle Detector Instrument (JEDI)	APL	Ions 0.015–20 MeV Electrons 0.02–1 MeV	Auroral particle distributions, ion composition
Jovian Auroral Distributions Experiment (JADE)	SwRI	Electrons 100 eV–100 keV Ions 10 eV–40 keV	Auroral particle distributions, ion composition
Waves	U. Iowa	4 m electric dipole & magnetic search coil E-field 50 Hz–40 MHz B-field 50 Hz–20 kHz E bursts 50 Hz–100 kHz B bursts 50–20 kHz Waveforms 1.0 MHz bandwidth	Radio & plasma waves
UltraViolet Spectrograph (UVS)	SwRI	FUV spectral imager wavelength 70–205 nm with 125 km resolution	Spatial & temporal auroral structure
Jovian InfraRed Auroral Mapper (JIRAM)	IAPS/INAF, Italy	IR spectral imager 2–5 microns	Spatial & temporal atmospheric structure and dynamics
JunoCam Juno Camera	Malin Space Sciences Systems	Visible imager	Atmospheric dynamics and structure

Figure 3.5: Juno on-board scientific instruments and experiments, courtesy of [Bolton et al., 2017].

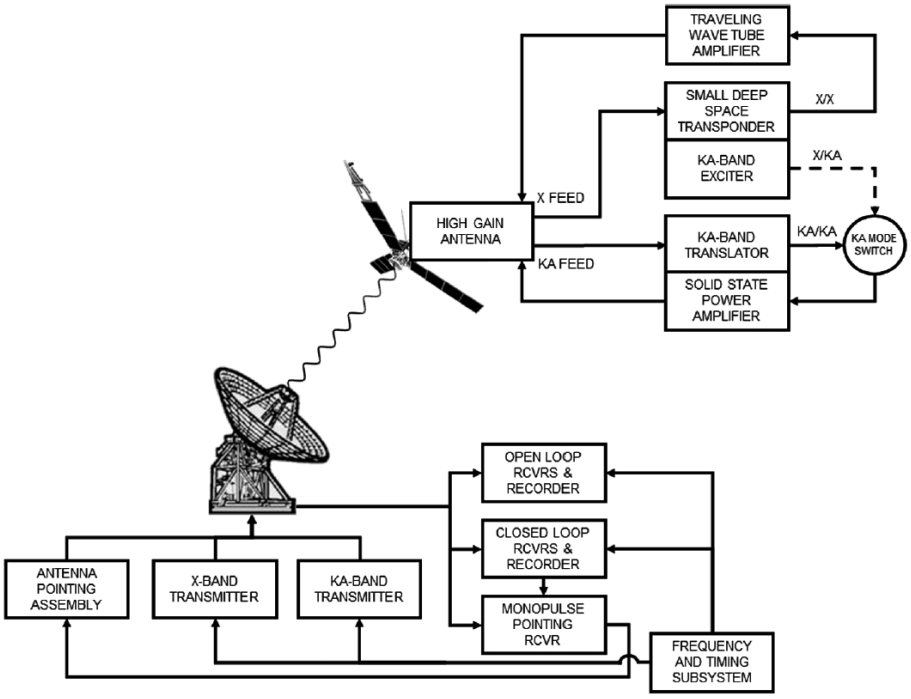

Figure 3.6: Diagram of the Juno gravity science instrumentation on the Juno spacecraft and at the Goldstone DSCC, courtesy of [Asmar et al., 2017].

3.3.2 The Acquisition Campaign

The acquisition campaign of radiometric data was carried out between December 2020 and June 2021. During this time, SDSA recorded the downlink signal of the Juno spacecraft at X-band in a three-way configuration, which was possible thanks to the uplink provided by the Madrid Deep Space Complex. The main objective of the acquisition campaign was to provide nominal values for the station performance and compare different operational settings of the antenna subsystems. The result of this investigation would provide information on the optimal antenna configuration for future involvement in deep space missions of the ground station, particularly regarding the frequency stability of telecommunication links, which can be a strict requirement for radio science investigations. As the same radiometric data was recorded at the Madrid complex and used to perform orbit determination of the Juno spacecraft, the acquisition campaign provided the possibility of identifying noise sources common to both signal paths and isolating the station's contribution to the uncertainties in the tracking accuracy.

Starting in December 2020, SDSA started acquiring radiometric data from the Juno spacecraft during its transmission of telemetry for navigation data. The interest of SDSA was in the pure sinusoidal tones (i.e. no telemetry) transmitted for navigation purposes. In particular, the focus of the acquisition campaign was on the downlink signals transmitted when Juno was far from its closest approach to Jupiter. In fact, differently from the gravity science experiment, the objective of the acquisition was not to perform estimations on the gravity field of Jupiter, but to evaluate the quality of orbit determination when using SDSA as an ancillary tracking station, with a primary station from DSN providing the baseline to the tracking accuracy. In consideration of the differential performance of SDSA to be computed when using different subsystem configurations, Table 3.2 reports the three antenna configurations investigated. Antenna mechanical noise is a known contributor to the tracking accuracy [Notaro et al., 2020], and part of it is caused by the vibration of the structure when moving parts are involved. To investigate this phenomenon in SDSA, the pointing direction update frequency and the employment of the active surfaces were investigated during different passes. SDSA is based on the DISCOS control software [Orlati et al., 2016], and in consideration of a downlink frequency of 8.5 GHz and the main reflector diameter of 64 m, the half-power beamwidth (**HPBW!**) can be approximately estimated at 0.04 deg. In consideration of this and the relatively small change in the angular position of Juno during tracking activities, the control software is nominally set to update the pointing schedule with a frequency of 60 seconds. This way, the signal remains in the HPBW of the antenna and mechanical movements are minimized. To evaluate possible noise additions to the observables, this effect was investigated by employing an alternative configuration, with the pointing being updated every 23 seconds. This value was chosen to avoid using a submultiple of the original update frequency and inadvertently creating harmonics at the nominal update frequency, when analyzing the stability of the observables. The second alternative configuration investigated (i.e. number 3) was aimed at evaluating the effect of the active surfaces on the quality of tracking activities. As already introduced, thermal and gravity deformations can reduce the quality

of the transmission link, and a lower SNR introduces more uncertainty in the estimation of the Doppler observables. On the contrary, the effect of changing the attitude of the panels of the main reflector on the quality of the downlink signal is unknown. In particular, no information is known on the mechanical noise introduced by the continuous movement of the panels, which is mapped to a look-up table according to the antenna elevation to compensate gravitational deformations. To minimize the negative effect of not employing active compensations of the panels of the main reflectors, these were positioned as a function of the mean antenna elevation during the tracking arc. Table 3.3 summarizes the tracking passes acquired with SDSA. Overall, the acquisition campaign consisted in 23 arcs with different durations and antenna configurations, defined over 17 passes of the Juno spacecraft. During the data downlink, both the closed-loop and open-loop chains were active. While the tracking durations were longer than the duration reported, some of the I&Q samples have been ignored during the computation of the results due to their unreliability. In particular, tracking epochs with an elevation lower than a defined value (15 deg) were not considered in the orbit determination procedure due to the difficulty in estimating the atmospheric delay introduced by the transmission path. Also, some of the passes did not provide sufficient data to perform an analysis due to the impossibility to match the availability of the SDSA to the two-way transmission of the Juno spacecraft. One-way data was not used, as it is characterized by a higher frequency instability due to the on-board USO.

Table 3.2: Overview of the different antenna configurations tested.

Configuration Number & Name	Number of Passes	Overall Duration	Description
1 Nominal	12	18:55:21	Optics compensation is active when changing elevation, pointing direction updated every 60 seconds
2 Quick Schedule	2	5:45:50	Optics compensation is active when changing elevation, pointing direction updated every 23 seconds
3 Locked Optics	4	10:33:36	Optics compensation is non-active when changing elevation, pointing direction updated every 60 seconds

Table 3.3: Overview of the data acquired during the acquisition campaign.

Arc Number	Date	DOY	Configuration	Net Duration
1	04/12/2020	2020 – 339	Nominal	01:39:11
2	05/02/2021	2021 – 036	Nominal	03:03:15
3	25/02/2021	2021 – 056	Nominal	02:15:00
4	27/02/2021	2021 – 058	Nominal	04:28:28
5	01/03/2021	2021 – 060	Nominal	04:29:38
6	13/03/2021	2021 – 072	Nominal	04:38:00
7	07/04/2021	2021 - 097	Nominal	00:00:00
8	12/04/2021	2021 – 102	Nominal	05:03:57
9	22/04/2021	2021 – 112	Nominal	01:00:03
10	22/04/2021	2021 – 112	Quick Schedule	01:18:43
11	30/04/2021	2021 – 120	Nominal	00:19.15
12	30/04/2021	2021 – 120	Locked Optics	02:54:25
13	04/05/2021	2021 – 124	Nominal	00:00:00
14	06/05/2021	2021 – 126	Nominal	00:26:39
15	06/05/2021	2021 – 126	Locked Optics	02:52:08
16	08/05/2021	2021 – 128	Nominal	03:49:14
17	08/05/2021	2021 – 128	Locked Optics	01:23:16
18	21/05/2021	2021 – 141	Nominal	00:00:00
19	08/06/2021	2021 – 159	Nominal	00:00:00
20	10/06/2021	2021 – 161	Locked Optics	00:55:52
21	10/06/2021	2021 – 161	Nominal	00:27:53
22	16/06/2021	2021 – 167	Nominal	00:00:00
23	16/06/2021	2021 – 167	Quick Schedule	04:27:26

3.3.3 Observables Generation

As previously defined, the closed-loop segment of the receiver estimates the amplitude, phase, and frequency of the downlink signal directly. The output of this segment is therefore directly the observables to be compared to the ones computed with the dynamical model of the spacecraft and the Solar System. The open-loop receiver, on the contrary, records raw I&Q data that need to be pre-processed. This pre-processing consists of the generation of the Doppler observables associated with the residual frequency using the developed estimation algorithms, and the compensation of the rotation of the Juno spacecraft [Marini, 1971]. The sky frequency is computed from the residual frequency in consideration of the down-conversion steps in the receiver by knowing the reference frequency of the local oscillator and mixers involved.

Orbit determination is performed at different count times. Usual values are 1 second and 60 seconds. The first value emulates the output rate of the DSN closed-loop receivers, while the second one filters most of the thermal noise (which affects the quality of the observables at low count times). The observables are generated through the routine described in subsection 2.3. In consideration of the limitations on the integration time and

coherency between the closed-loop and open-loop segments of the receiver, all observables have been generated with an integration time of 1 second. The required count time was then obtained through averaging of the observables to obtain one average frequency every 60 seconds.

3.3.4 Orbit Determination Setup

The orbit determination of the Juno spacecraft was performed using JPL's toolkit MONTE. As defined in section 1.2, the accuracy of the orbit determination depends on the quality of the dynamical model used to integrate the trajectory of the spacecraft. In consideration of the uncertainties in the characteristics of SDSA, the solve-for parameter employed are defined in Table 3.4. The dynamical model was developed starting from the one used for the gravity science experiment of Juno, in consideration of its demonstrated high fidelity in describing the dynamics of the Juno spacecraft. The initial state of the spacecraft and its attitude during every pass were recovered from the navigation solutions from JPL.

Table 3.4: Solve-for parameters of the filter used for the multi-arc OD procedure.

Solve-for Parameters	Type
State of the spacecraft	Local
SRP Scale	Local
Troposphere zenith dry delay	Local
Troposphere zenith wet delay	Local
Impulse burns	Local
Three-way clock bias	Local
Station position	Global

As previously defined, local parameters are estimated each arc and can have different values. On the contrary, global parameters are estimated with a lower a-posteriori uncertainty by using the multi-arc strategy, as defined in section 1.2. With regard to the consider parameters, these include the ephemerides of the Jupiter system, the Earth orientation parameters, Earth tides, spacecraft geometry, etc.

3.3.5 Media Calibration

Calibration of ionospheric and tropospheric delays was performed in collaboration with JPL. The total atmospheric delay introduced is obtained from three contributions:

- Ionospheric delay.
- Tropospheric wet delay.
- Tropospheric dry delay.

Ionospheric delays are computed by measuring the instantaneous delays through dual frequency GPS measurements, and the contribution to the total delay is then fitted using

polynomial curves. Tropospheric delays, on the contrary, require both statistical models and local measurements to be accurately calibrated. Calibrations are usually based on statistical models to estimate the seasonal contribution to the dry delay. Differences from the seasonal model are then computed using thermal and barometric measurements at the station location. To perform the estimation and calibration of the dry and wet delays introduced by the local troposphere at the SDSA site, the atmosphere monitoring system of the SRT was employed [Buffa et al., 2016]. In particular, the weather metrology system of the station was used to record the local thermodynamic parameters. These were then used to create standard format files (RINEX) to be sent to the DSN calibration and modeling services, which provided an estimation of the zenith total delay due to the troposphere [Slobin and Pham, 2010]. This delay must then be mapped in the pointing direction of the antenna to estimate the total path delay.

3.3.6 Radiometric Measurements

Table 3.5 shows an overview of the tracking passes and the RMS of the residuals after the OD procedure. The results were obtained by considering only the Two-way tracking configuration at elevations higher than 15 degrees. This choice was performed due to the unreliability in the estimation of the tropospheric total delay at low elevations, due to the length of the signal path inside of the atmosphere. Arcs 7 and 22 were not used in the orbit determination setup as only One-way Doppler observables were available. Residuals from arcs 13 and 18 were not reliable to provide an OD estimation due to errors in the metadata that prevented the dynamical model to converge to a solution. As no ancillary information was available to recover the measurement information, these arcs were ignored in the computation of the multi-arc solution. Arc 19 was acquired during Juno's closest approach to Jupiter (PJ 34). The current capabilities of SDSA do not include Doppler pre-steering of the downlink bandwidth. In consideration of this, the received residual frequency is simply the sky frequency minus a constant offset. As the perijoves are characterized by high accelerations, arc 19 consisted of very high-frequency rates (over 170 Hz/s at the closest approach). This made the analysis of this arc possible but incoherent with the other passes, since the boundaries on the integration time would make the observable generations noisier than usual. Therefore, it was decided not to use the Doppler measurements from this pass in the analysis.

Table 3.5: Residuals RMS from the tracking campaign. NA defines arcs where the metric is not available because of insufficient data.

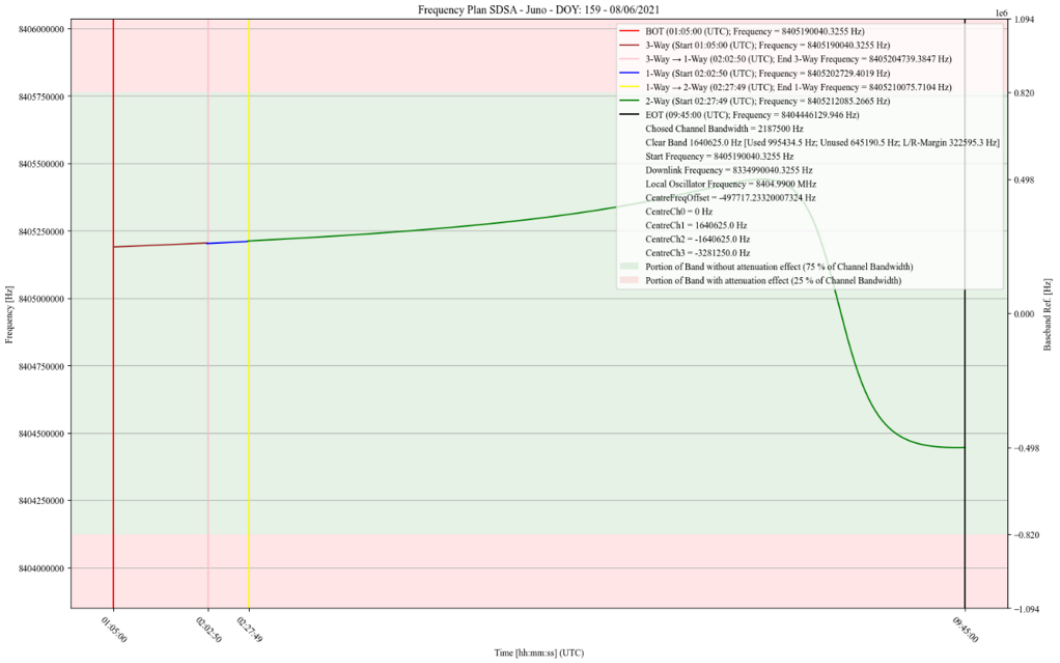

Figure 3.7: Predicted downlink frequency during PJ 34, as seen from SDSA.

Arc Number	Date	OL RMS (mm/s)	CL RMS (mm/s)
1	04/12/2020	SDSA: 0.078 DSS-55: 0.057	SDSA: 0.072 DSS-55: 0.057
2	05/02/2021	SDSA: 0.800 DSS-54: 0.869	SDSA: 0.787 DSS-54: 0.869
3	25/02/2021	SDSA: 0.080 DSS-55: 0.082	SDSA: 0.075 DSS-55: 0.082
4	27/02/2021	SDSA: 0.072 DSS-55: 0.078	SDSA: 0.067 DSS-55: 0.071
5	01/03/2021	SDSA: 0.155 DSS-65: 0.139	SDSA: 0.135 DSS-65: 0.132
6	13/03/2021	SDSA: 0.082 DSS-63: 0.044	SDSA: 0.082 DSS-63: 0.042
7	07/04/2021	NA	NA
8	12/04/2021	SDSA: 0.072 DSS-63: 0.032	SDSA: 0.030 DSS-63: 0.021
9	22/04/2021	SDSA: 0.037 DSS-55: 0.033	SDSA: 0.027 DSS-55: 0.025
10	22/04/2021	SDSA: 0.040 DSS-55: 0.029	SDSA: 0.028 DSS-55: 0.018
11	30/04/2021	SDSA: 0.069 DSS-55: 0.051	SDSA: 0.066 DSS-55: 0.052
12	30/04/2021	SDSA: 0.010 DSS-55: 0.094	SDSA: 0.094 DSS-55: 0.085
13	04/05/2021	NA	NA
14	06/05/2021	SDSA: 0.050 DSS-54: 0.030	SDSA: 0.027 DSS-54: 0.017
15	06/05/2021	SDSA: 0.047 DSS-54: 0.038	SDSA: 0.022 DSS-54: 0.017
16	08/05/2021	SDSA: 0.061 DSS-55: 0.041	SDSA: 0.043 DSS-55: 0.019
17	08/05/2021	SDSA: 0.097 DSS-55: 0.042	SDSA: 0.098 DSS-55: 0.034
18	21/05/2021	NA	NA
19	08/06/2021	NA	NA
20	10/06/2021	SDSA: 0.032 DSS-55: 0.030	SDSA: 0.024 DSS-55: 0.019
21	10/06/2021	SDSA: 0.040 DSS-55: 0.029	SDSA: 0.031 DSS-55: 0.022
22	16/06/2021	NA	NA
23	16/06/2021	SDSA: 0.066 DSS-55: 0.075	SDSA: 0.061 DSS-55: 0.068

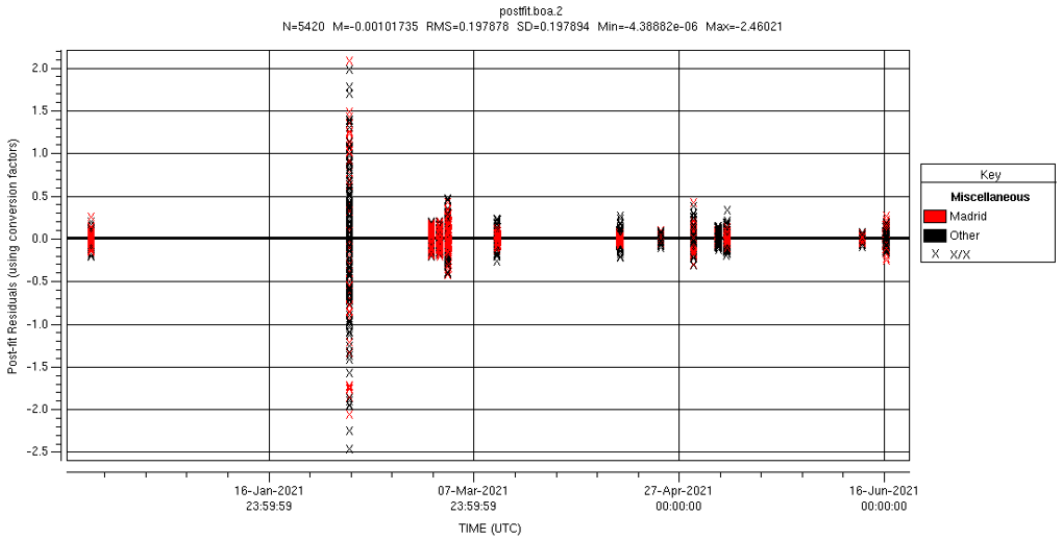

Figure 3.8: Residuals of the Doppler measurements acquired during the acquisition campaign.

Fig. 3.8 shows an overview of the OD residual of the acquisition campaign, with the single arcs highlighted in Fig. 3.10 and Fig. 3.11. As expected, all arcs have a comparable RMS, with pass-by-pass variations justified by the variability in the weather conditions. The only exception is provided by arc 2, as the Sun-Earth-Probe (SEP) angle was low with respect to standard navigation passes, making the phase scintillation due to solar plasma the main noise contribution, and increasing the RMS of the residuals of one order of magnitude for both stations.

Fig. 3.9 shows the spectrogram extracted from the open-loop data recorded during arcs 9 and 10. The residual frequency follows the expected trend of a sky frequency from deep space, except for the discontinuity caused by the sweeping of the uplink frequency to switch from a One-way to a Two-way transmission. The black-out in the measurements is caused by a stop in the acquisition to change the antenna configuration from nominal to a “locked” configuration.

Fig. 3.12 provides a global characterization of the differential tracking performance of SDSA with respect to the Madrid complex stations: the RMS of both stations is reported for the closed-loop and open-loop data with a count time of 60 seconds. Only arcs when SDSA was using a nominal configuration are considered. To perform a direct comparison between the stations, the average ratio between the RMS at the two stations has been computed. This ratio is about 1.3 for both types of data, which means that by considering Madrid’s complex accuracy as the baseline for tracking, the accuracy of SDSA is approximately 77% of the other deep space stations.

The effect of noise sources on the stability of the residuals can be evaluated through the Allan standard deviation. To this end, the residuals of SDSA and the DSN stations have been analyzed at different integration times to estimate the noise sources that affect the tracking accuracy mostly. Fig. 3.13, Fig. 3.14, and Fig. 3.15 show the computed average overlapping Allan standard deviation of the Doppler residuals of the different tracking configurations, together with the 25th and 75th percentiles. Discontinuities can be observed at high integration times due to the different number of residuals available during different

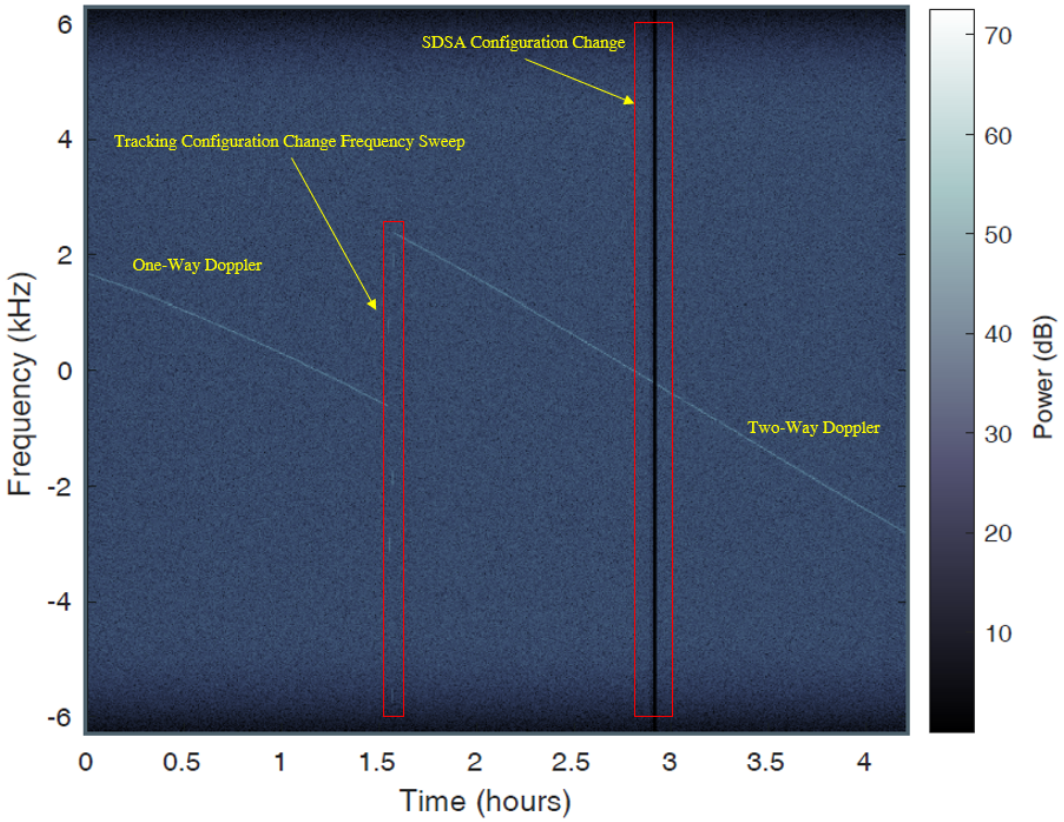

Figure 3.9: Spectrogram of the open-loop measurements from arcs 9 and 10.

tracking arcs. As visible from 3.15, the configuration with the deactivated surface control seems to provide the worst performance, especially at medium-high integration times. This can be expected by the change in the signal path, and therefore station delays, caused by the slow changes in elevation during tracking activities and gravity deformations of the structure. However, since the number of trackings is limited with this configuration, no definitive conclusion can be drawn. Fig. 3.14 shows the configuration with a more frequent tracking schedule update. In this case, the Allan deviation at high integration times has a slope similar to that expected from tropospheric noise, and a smaller uncertainty band, suggesting more stable residuals can be achieved when employing this configuration rather than the nominal one. Even for this case, more passes would be required to achieve more reliable results.

Overall, this preliminary investigation on the stability of the residuals of radiometric measurements acquired with SDSA suggests the active compensation does not introduce mechanical noise to the tracking accuracy at a detectable level, while the deformations caused by pointing at low elevations affect the stability of the observables visibly. In consideration of this, future investigations should focus on the validation of the performance when tracking using the other two configurations.

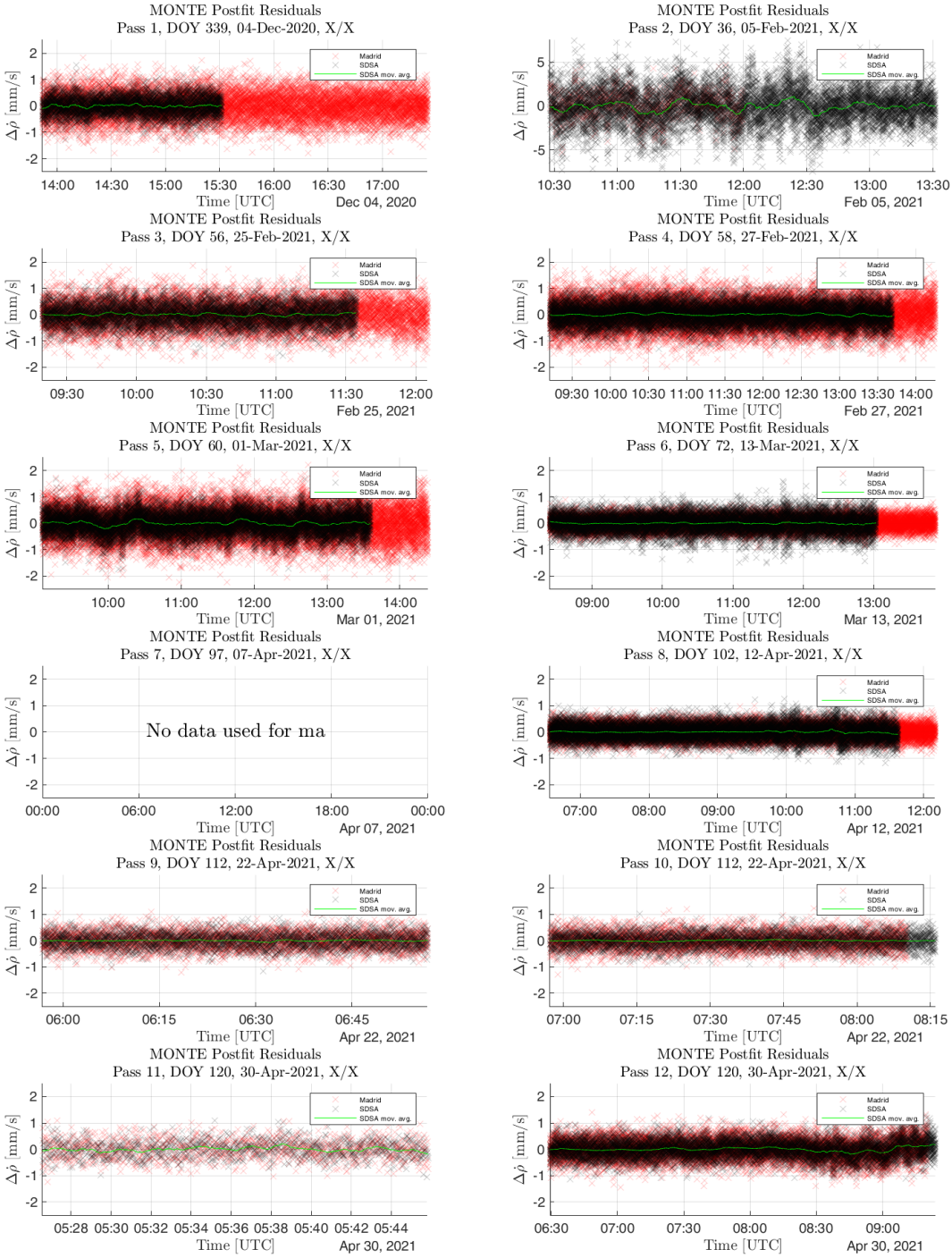

Figure 3.10: Post-fit multi-arc residuals (arcs 1-12).

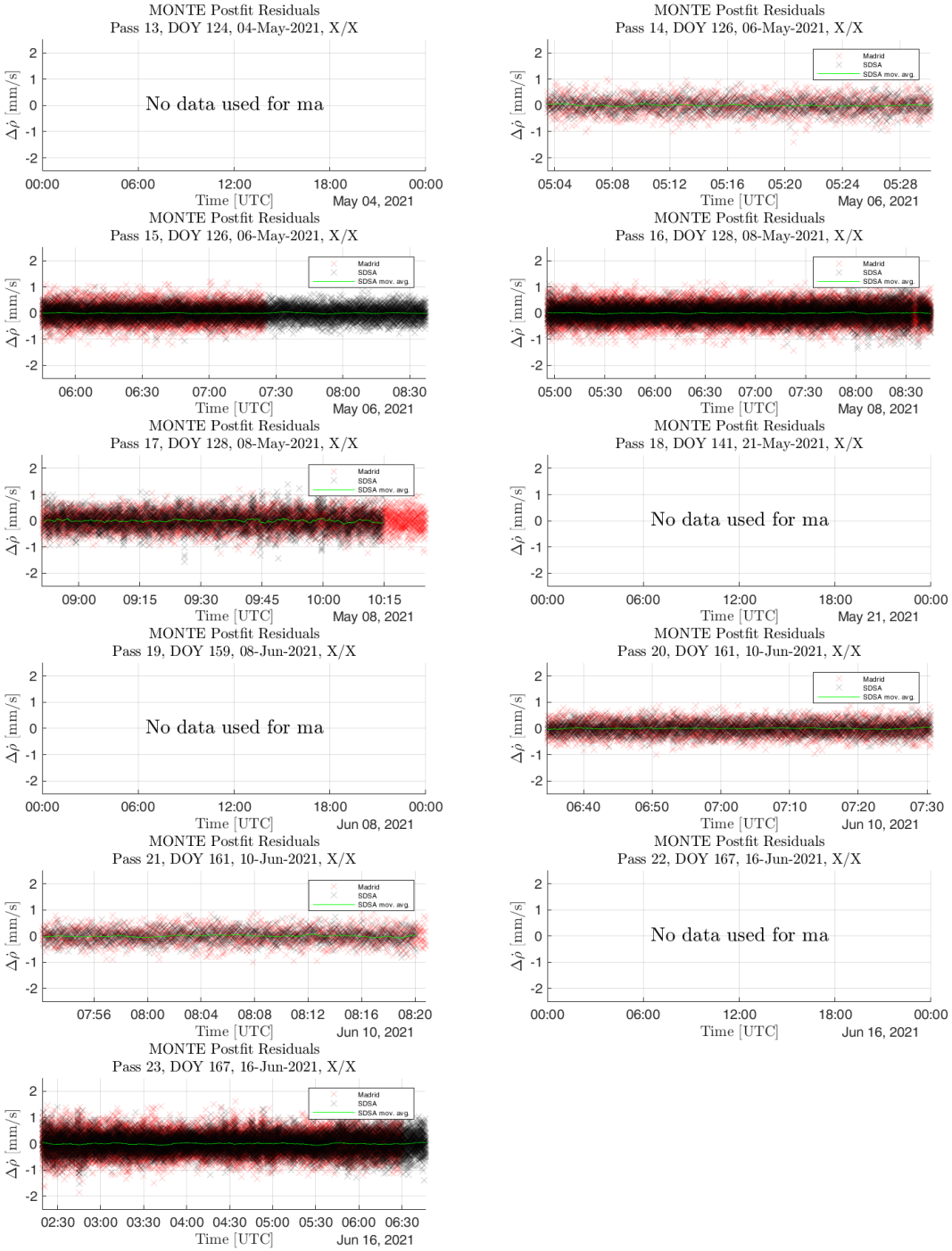

Figure 3.11: Post-fit multi-arc residuals (arcs 13-23).

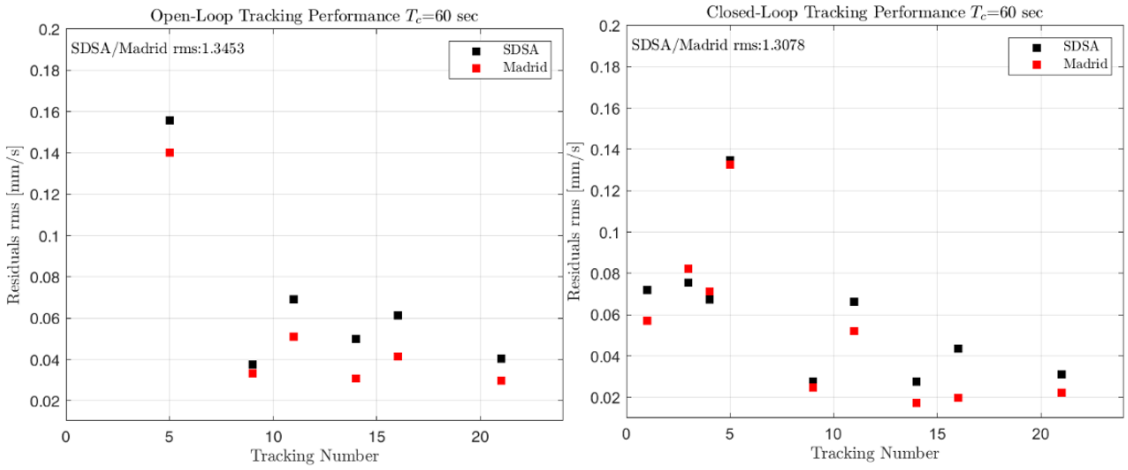

Figure 3.12: RMS of Open-Loop and Closed-Loop residuals at SDSA and Madrid DSS.

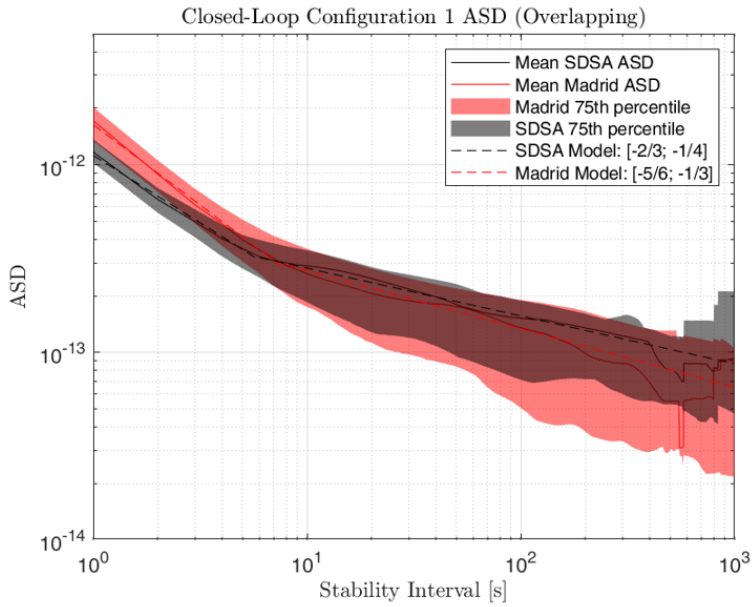

Figure 3.13: Allan deviation of the frequency residuals and uncertainties bands for SDSA configuration 1 during radiometric tracking. 12 passes, 18:55:21 hours of radiometric data.

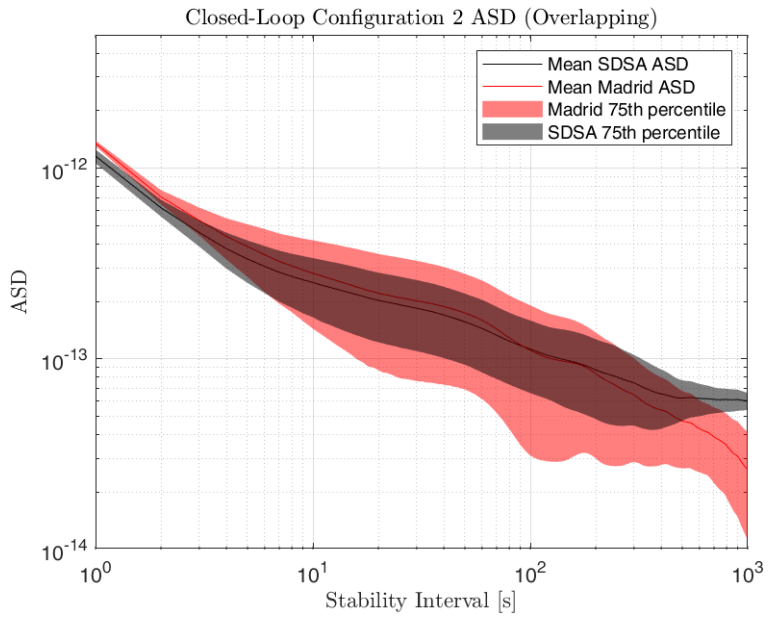

Figure 3.14: Allan deviation of the frequency residuals and uncertainties bands for SDSA configuration 1 during radiometric tracking. 2 passes, 5:45:50 hours of radiometric data.

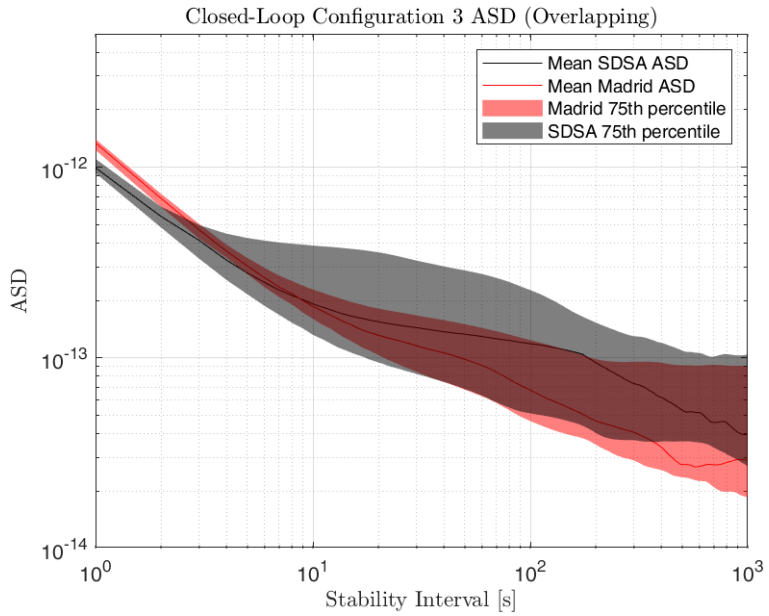

Figure 3.15: Allan deviation of the frequency residuals and uncertainties bands for SDSA configuration 3 during radiometric tracking. 4 passes, 10:33:36 hours of radiometric data.

3.3.7 Antenna Position Estimation

As the antenna coordinates have not been estimated through systematic tracking of spacecraft, this parameter was chosen to be considered as a solve-for parameter, in order to exploit these new measurements to improve the accuracy of the SDSA position estimation. Results on the estimation of the station coordinates are available in [Sanna et al., 2014] and [Petrov, 2017]. The first was obtained by GNSS measurements, and the second by using the SRT to perform VLBI radio-astronomy investigations. Both a-priori values have been used to perform different OD runs, with and without the tropospheric delays as solve-for parameters.

While both coordinates provide accurate results, experimental data seem to be more in agreement with Sanna's work. Fig. 17 shows the error ellipse in the longitude and cylindrical radius coordinate components of SDSA. In particular, the Z coordinate is not shown, as Doppler measurements do not have any information content that can improve the estimation of this coordinate, due to the nature of the measurements themselves. As can be seen, when estimating the local troposphere (as an internal parameter), the uncertainty on the station position increases. This is expected, as the variations in the measurements due to noise are justified by the increased uncertainty in the dynamical mode. Either way, the new position estimation (see Table 7) and covariance are coherent with the a-priori information, suggesting a current and improved estimation. The a-propri uncertainty considered was 3 m in all directions (cartesian coordinates). This was greatly reduced with the newly acquired data, except the one related to the Z coordinate. This is due to the fact that the Z component is insensitive to Doppler measurements.

Table 3.6: Baseline, estimated, and a-posteriori uncertainty in the SDSA position coordinates.

Coordinate	Baseline [km]	Estimated [km]	A-posteriori Sigma [km]
SDSA Cylindrical Radius	4.9292139e+03	4.9292131e+03	2.1378e-04
SDSA Longitude	9.2451485e+00	9.2451452e+00	8.2208e-06
SDSA Z	4.0351361e+03	4.0351361e+03	3.0000e-03

3.3.8 Media Calibrations Investigation

With the purpose of moving towards working with SDSA independently from other partners, additional resources were invested in testing the appropriateness of developing in-house calibrations for the tropospheric delays. In particular, these were generated starting from the weather monitoring system of SDSA and sent to e-GEOS, an ASI/Telespazio company dedicated to the processing of Earth Observation and Geospatial Information data. After generating the RINEX files associated to the station's location and atmospheric parameters, Saastamoinen's model was employed to estimate the Zenith Hydrostatic Delay (ZHD) and the Zenith Wet Delay (ZWD), which contribute to the total delay (ZTD) to be estimated.

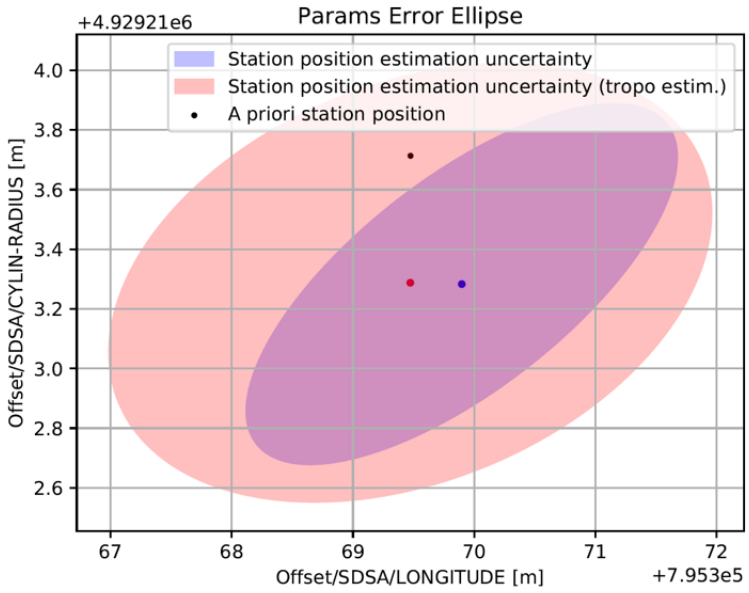

Figure 3.16: A-priori, estimated, and a-posteriori error ellipse of the SDSA position coordinates.

$$\mathrm{ZHD}(lat, h, p_s) = 10^{-6} \frac{k_1 R_d}{g_m(lat, h)} p_s \tag{3.1}$$

$$\mathrm{ZWD}(lat, h, e_s, T_{ms}, \lambda) = 10^{-6} \frac{R_d}{g_m(lat, h)} \frac{k_2}{\lambda + 1} \frac{e_s}{T_{ms}} \tag{3.2}$$

Where lat is the latitude of the location, h its height above sea level, p_s and e_s the air total pressure and water vapour pressure at earth surface, T_{ms} the mean temperature of the water vapour above the surface, and λ the vapour pressure decrease factor. The other variables in the equations are physical constants, and are defined in [Martellucci, 2012]. The gravity acceleration at the mass center of air is then defined as:

$$g_m(lat, h) = 9.784(1 - 0.00266cos(2lat) - 0.00028h) \tag{3.3}$$

With these, an independent ZTD was computed, and then fed to the OD program to map it in the pointing direction of the antenna. Fig. 3.17 shows the residuals at SDSA (60 seconds count time) for the first arc (04/12/2020) obtained using the calibrations provided by JPL and those developed independently. The quality of the residuals is very similar with a RMS of 0.072071 mm/s for the DSN calibrations, and 0.071965 mm/s for the one computed with ASI. Generally, the tropospheric delays are modelled as trigonometric polynomials that fit the computed delays. As the exact model and computation of the ZTD at the DSN division is not known, it is safe to assume the very small differences in the residuals are caused by a variation in the processing routines.

3.3.9 Deep Space Tracking Error Budget

Different radio science applications require the evaluation of the radiometric measurements at different integration times. In consideration of this, a general error budget for

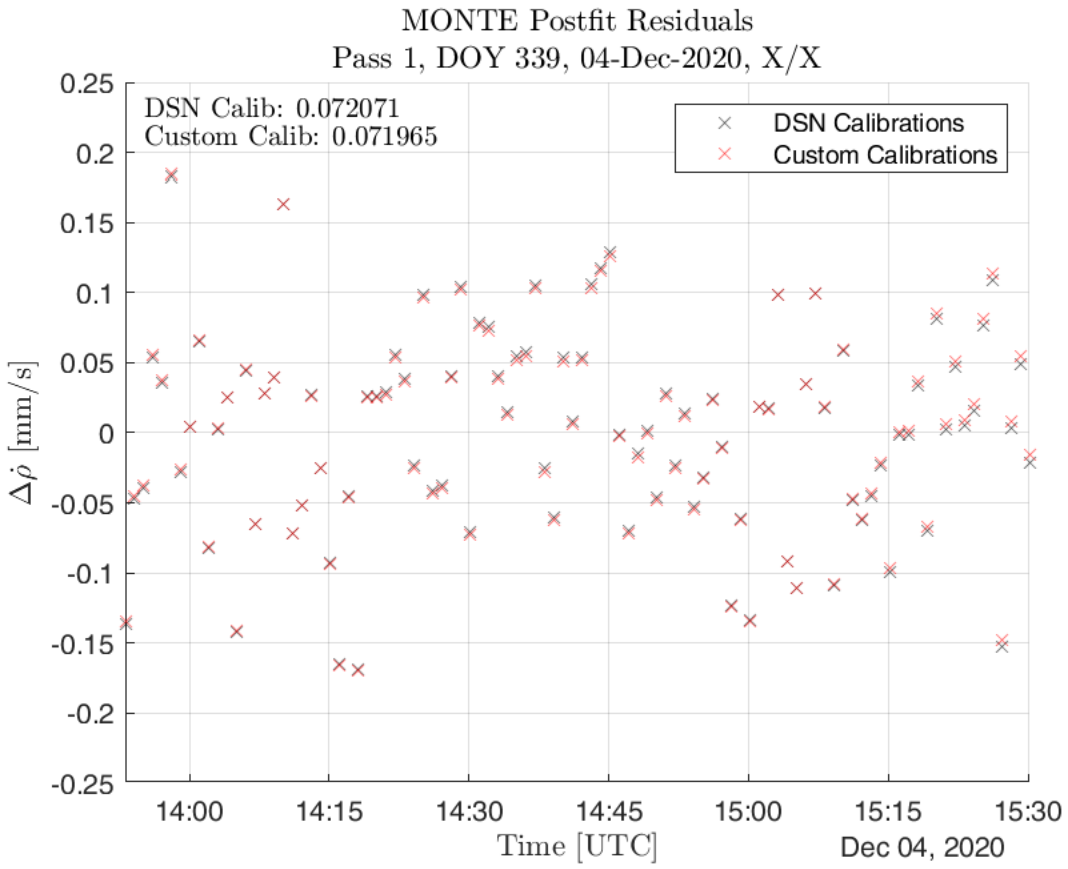

Figure 3.17: OD post-fit residuals using DSN or custom tropospheric delay calibrations.

deep space tracking with SDSA must be developed to include the effect of noises at different averaging times. The main noise sources when dealing with deep space signals are described in section 1.2. Here, a model to predict the accuracy of tracking is presented and discussed.

As previously defined, the frequency stability of signals is defined using the Allan deviation. By employing a dynamical model to fit the observed measurements, the obtained residuals are centered around the zero, and have a variance proportional to the intensity of uncalibrated random noise. As the Allan deviation is computed at higher integration times, the effects of high-frequency noise sources are reduced, to the point that slow-varying effects become predominant. In particular, low integration times ($\tau \leq$10 seconds) are dominated by thermal noise, medium integration times (10$\leq \tau \leq$500) are dominated by the noise introduced by tropospheric delays, and high integration times $\tau \geq$500 s highlight the effect of solar plasma. In consideration of the various noise sources, the following contributions have been modelled and analyzed to develop an error budget when tracking with SDSA, based on the elements analysed in [Iess, 2012].

- Wet troposphere: the frequency shift caused by this noise source is modelled as a constant value, plus a sinusoid term with period of 1 year. The model is developed for a station in the northern hemisphere, and the phase of the sinusoid must be shifted by 180 degrees for a receiver in the southern one. The time is defined in seconds past J2000, and the model is valid for a Two-way transmission.

$$\sigma_{tropo}(\tau = 60) = \alpha + \beta sin(\omega t + \phi) \begin{cases} \alpha = 6.5 \times 10^{-14} \\ \beta = 3.5 \times 10^{-14} \\ \omega = 1.99\, rad/s \\ \phi = -1.37\, rad \end{cases} \tag{3.4}$$

- Plasma: plasma noise model include both interplanetary and ionospheric plasma. This noise contribution is defined as a function of the SEP angle, and in general needs to be corrected (i.e. amplified) for missions in the inner Solar System.

$$\sigma_{tropo}(\tau = 60) = \begin{cases} 1.76 \times 10^{-14} sin(\text{SEP})^{-1.98} + 6.25 \times 10^{-14} sin(\text{SEP})^{0.06}\ 0^\circ \leq \text{SEP} \leq 90^\circ \\ (1.76 \times 10^{-14} + 6.25 \times 10^{-14}) sin(\text{SEP})^{1.05}\ 90^\circ \leq \text{SEP} \leq 170^\circ \\ 1.27 \times 10^{-14}\ 170^\circ \leq \text{SEP} \leq 180^\circ \end{cases} \tag{3.5}$$

- On-board spacecraft transponder: this noise contribution depends on the on-board transponder, and is affected by the radio system design. The contribution is estimated through ground tests, and for this model, an interpolated model of the Allan deviation of the Juno transponder was employed, as reported in Table 3.7.
- Ground station: the contribution to the Allan deviation of residuals from the ground station can be modelled as a constant value, as it does not change with time. This value encompasses all contributions, from thermal and gravity deformations to electronics and vibrations due to the pointing control law. Due to the multiple contributions, the value of this has to be empirically estimated.

Table 3.7: Allan standard deviation of the Juno deep space transponder.

τ [s]	σ_y
1	3×10^{-13}
10	2.8×10^{-14}
100	3×10^{-15}
1000	4.6×10^{-16}

All contributions are modelled as an Allan deviation, and their values are taken from previous studies on Doppler tracking error budget [Iess et al., 2014]. The Allan deviation at an arbitrary integration time τ_1 (e.g. 60 seconds) can be mapped to a different integration time τ_2 by using Eq. 3.6.

$$\sigma_y(\tau_2) = \sigma_y(\tau_1)\sqrt{\frac{\tau_1}{\tau_2}} \tag{3.6}$$

The final model is defined in Eq. 3.7. Due to the nature of the Allan deviation, the addition of different contributions must be performed in terms of the Allan variance (i.e. Allan deviation squared).

$$\sigma_y^2 = \sigma_{stn}^2 + \sigma_{plasma}^2 + \sigma_{sc}^2 + \sigma_{tropo}^2 \tag{3.7}$$

With σ_y^2 the Allan variance of the residuals, and the station, plasma, spacecraft, and troposphere Allan variances, in order. This way, the experimental Allan deviation of the residuals can be used to isolate one or more of the other contributions, if not known.

For the validation of the performance of SDSA, the solve-for variable in Eq. 3.7 is the station contribution to the Allan variance. To estimate it, Eq. 3.7 is reordered to isolate the Allan deviation introduced by the station.

$$\sigma_{stn} = \sqrt{\sigma_y^2 - \left(\sigma_{plasma}^2 + \sigma_{sc}^2 + \sigma_{tropo}^2\right)} \tag{3.8}$$

Fig. 3.18 reports the error budget for SDSA at a 60 seconds integration time with its contributing parameters and the experimental Allan deviation of the residuals. In particular, Eq. 3.8 is valid for every arc characterized by its own residuals, and therefore a single estimation of the station Allan is provided by averaging the multiple estimations. In consideration of the variability of experimental data, the argument of the root in right-hand term of Eq. 3.8 can be negative. This condition suggests that the single pass was characterized by a statistically favorable link quality. In these cases, as the contribution to the residuals Allan cannot be negative, it was set to 0. In consideration of this, the estimation proposed defines a conservative result, as the contribution of the favorable tracking conditions was reduced. Overall, as the noise models employed are based on statistical averages and moments, the experimental dispersion visible in Fig. 3.18 was expected, as it follows the same trend seen in the development of the doppler error budget developed for the Cassini mission [Iess et al., 2014].

Finally, Fig. 3.19 shows the estimated station Allan deviation in a range of integration times from 1 to 1000. In consideration of the experimental variability of the station contribution, the 25th and 75th percentiles of the estimations at each integration time are reported for SDSA and the Madrid stations. Additionally, a log-linear piece-wise best-fit model for the station Allan deviation is presented for both stations.

Using the parametric models developed and shown in 3.19, it's also possible to present a differential performance evaluation of the station when employed in Doppler tracking. With respect to Table 9, the station contribution to the residuals noise at 60 seconds (as seen in section 3.3.6) can be confirmed, with a ratio between 1.09 and 1.43.

Table 3.8: Allan standard deviation of station contributions at different integration times.

Station	$\tau = 1$	$\tau = 10$	$\tau = 100$	$\tau = 1000$
SDSA	5.28×10^{-13}	2.57×10^{-13}	1.25×10^{-13}	6.12×10^{-14}
Madrid	1.50×10^{-12}	2.20×10^{-13}	8.77×10^{-14}	8.77×10^{-14}
Ratio	0.35	1.09	1.43	0.69

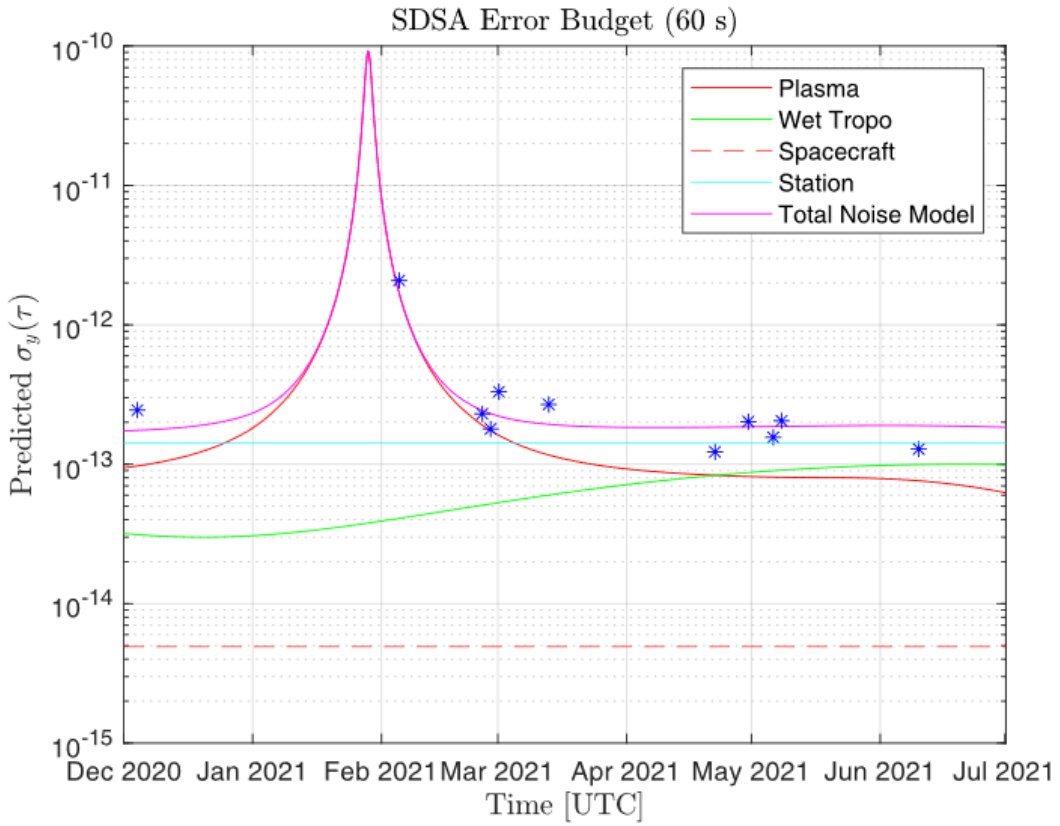

Figure 3.18: SDSA error budget and single contributions at a 60 seconds integration time.

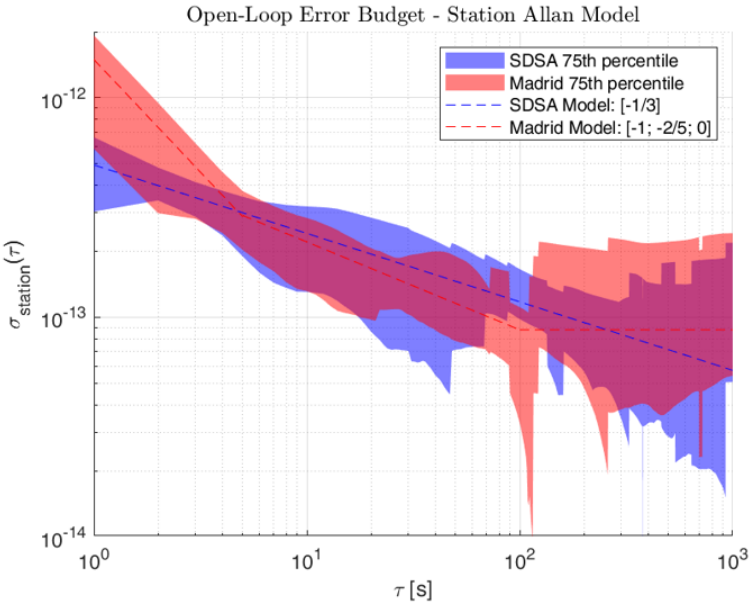

Figure 3.19: Estimated station Allan deviations.

3.3.10 Antenna Gain and Noise Contribution

With the open-loop receiver of SDSA, post-processing of data was possible. This way, it's been possible to evaluate the P_c/N_0 of the downlink signals. As reported in Fig. 3.20, this values averages around 39.5 dBHz, when considering all the tracking passes. Fig. 3.21 reports an example of the P_c/N_0 during the tracking of 25/02/2021: the black line defines

the quality of all the signal that was received, and the blue line of the part of the signal that was used to compute the observables. The results are coherent with another independent analysis performed by ASI on-site [Valente et al., 2022], confirming an average antenna gain around 72 dBi and a system temperature of 56.5 K.

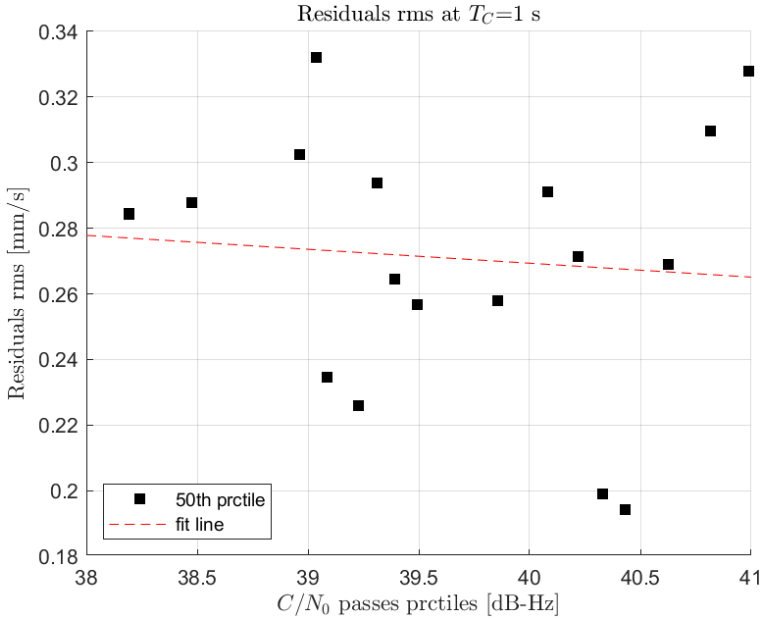

Figure 3.20: RMS of the residuals as function of the average P_c/N_0 of the passes.

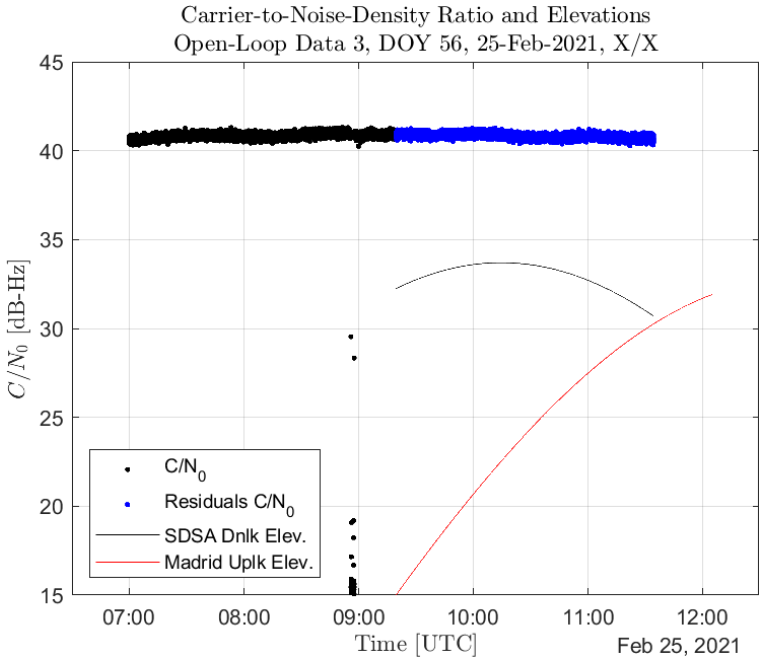

Figure 3.21: P_c/N_0 and antennas elevation for tracking arc 10.

Chapter 4

The DSS-17 Characterization and Subsystems Design

Contents

The DSN affiliated node DSS-17 is a ground station employing DSN and custom hardware located in Kentucky, USA. The 21-m diameter dish is operated and maintained by the team of the Morehead State University (MSU). The conversion of this antenna originally dedicated to radio-astronomy started in 2014 with the beginning of a partnership between JPL and the university. The goal of this collaboration is to demonstrate the feasibility of enabling tracking capabilities for already existing ground stations. In particular, with the hardware support from the DSN, the transition to a sensitive and accurate tracking station was feasible in a short timeframe: in 2021, the team at MSU passed the Operational Readiness Review, officially making the station the affiliated node DSS-17 of the DSN [Malphrus et al., 2018]. While being a case study for the technology transfer of know-how from the DSN to externally-managed stations, DSS-17 also started reducing the high demand for mission support from the DSN by performing tracking activities for the CAPSTONE mission, starting August 2022.

4.1 Complex Architecture

The receiving part of DSS-17 is an Azimuth/Elevation parabolic antenna located on the hills above the city of Morehead. Fig. 4.1 outlines the mechanical structure and main subsystems of the dish. Differently from the antennas on which DSN stations usually rely on, DSS-17 does not employ a BWG configuration, but instead has a front feed configuration. As the ground station supports TM downlink and TC uplink in both S-band

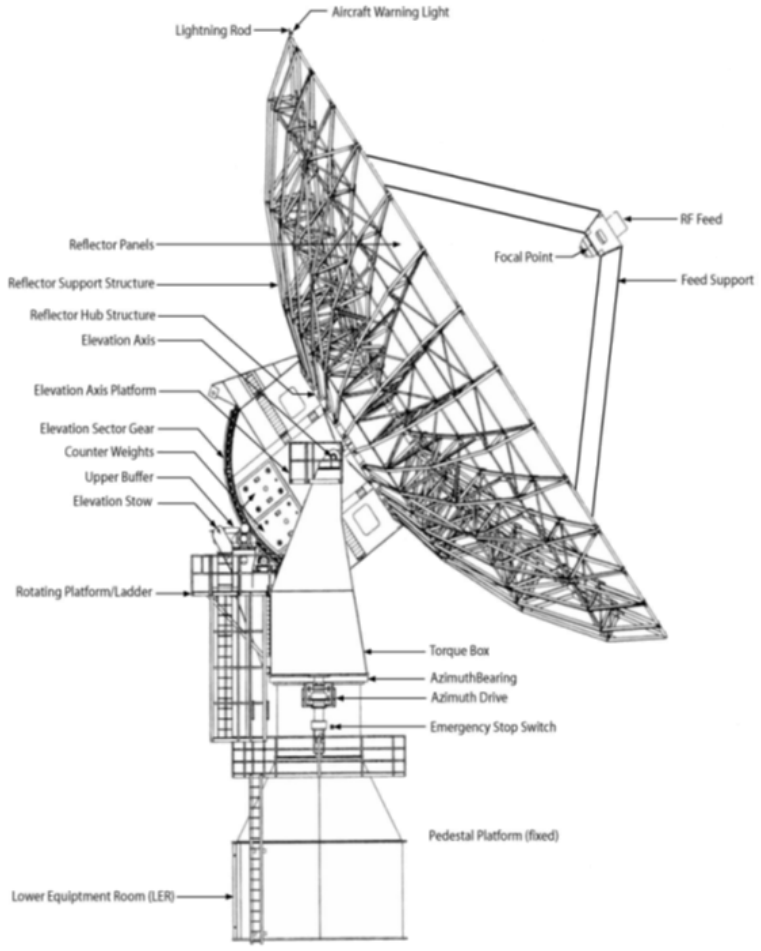

Figure 4.1: Schematics of the DSS-17 21-m dish [Malphrus et al., 2018].

and X-band, the feed requires to be switched manually when changing the configuration of transmission, instead of changing the path of the radio-frequency signal with a beam waveguide. The antenna has a pointing velocity greater than 3.0 deg/sec and 1.6 deg/sec for the azimuth and elevation components, respectively, and a pointing accuracy of 0.005 deg (rms). The surface tolerance of the primary reflector is less than 0.020" (rms), and the estimated aperture efficiencies of 0.653 and 0.564 at L-band and Ku-band are coherent with the expected performance of antennas when employing with a front feed configuration [Malphrus et al., 2018, Lehpamer, 2010].

As the signal is acquired at the radio-frequency feed, it is transmitted to the Lower Equipment Room (LER) where it is pre-processed before being transmitted to the Mission Operation Center (MOC). This processing includes amplification through an LNA and the mixing down to an IF of around 300 MHz. The physical transmission to the MOC is then performed through optical fiber.

Fig. 4.2 outlines the system architecture currently employed at DSS-17. The MOC interfaces with the antenna through the Deep Space Operation Center (DSOC) except for commanding, as telecommands are directly transmitted to the Uplink (UPL). Both telemetry and radiometric data are first transmitted to the Telemetry Tracking Delivery (TTD) at DSOC before being relayed to the MOC. The digitalization, estimation of the

residual signal phase, and TM demodulation is performed in the DSN DTT.

[Chang, 2015]. With regard to hardware, DSS-17 employs both DSN-supplied instrumentation and COTS equipment, allowing customization of the receiving architecture without sacrificing the high performance provided by the DSN equipment. Table 4.1 describes the current performance metrics of DSS-17 when operating in X-band.

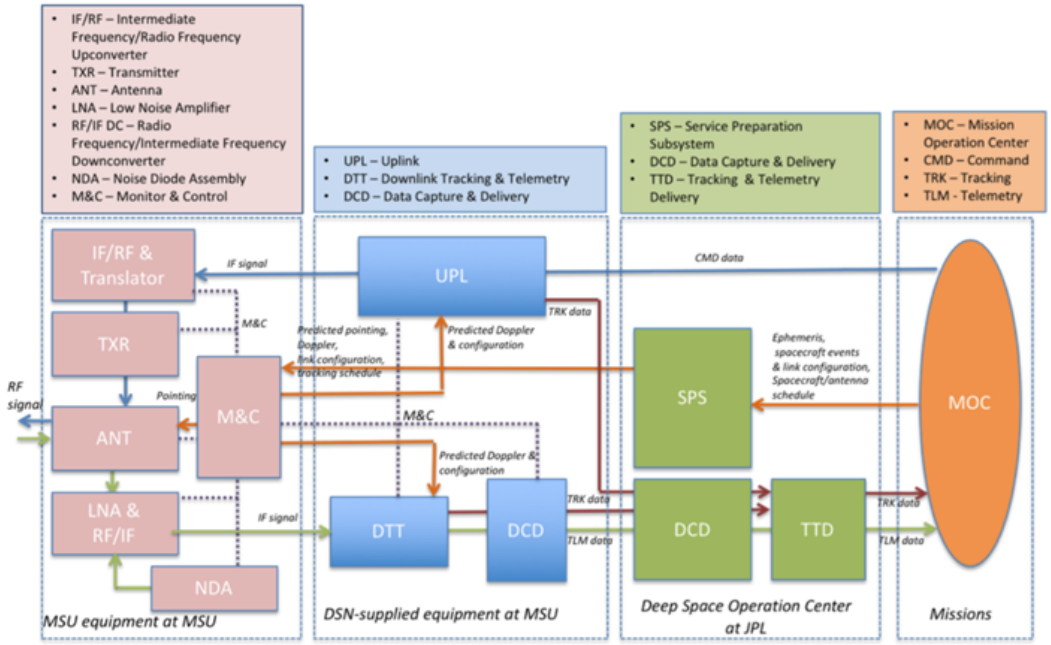

Figure 4.2: System architecture at DSS-17 [Malphrus et al., 2018].

Future developments to improve the ground station capabilities include the implementation of a secondary 12-m antenna. This secondary receiver will support near space missions, providing the station the capability of tracking multiple spacecraft simultaneously and further reducing the load on the DSN scheduling and mission support.

The tracking performance of DSS-17 has been recently evaluated through radiometric tracking of the STEREO-A, DART, and CAPSTONE missions in two-way and three-way configurations. As the antenna delay contributes to measurements errors, these were previously calibrated with an over air link testing able to simulate the spacecraft-antenna link. Delay measurements suggest a ranging accuracy of ± 0.3 m at X-band, with a ± 1 ns delay variation. Appropriate calibration of delays in the system also contributes to an increased quality of the Doppler residuals.

3-way Doppler tracking of the DART and STEREO-A missions was characterized by different accuracies: a 0.09 Hz (3.17 mm/s) rms for STEREO-A and a 0.02 (0.70 mm/s) Hz rms for DART, while the DSN reported a rms of 0.01 Hz (0.35 mm/s). According to the testing methods, the reasons behind this discrepancy in tracking accuracy is given by two factors:

- The link SNR at DSS-17 was lower than that of other DSN stations, due to a higher system temperature and smaller aperture.
- DSS-17 does not employ weather measurements systems to record the required in-

formation to perform media calibration when computing the received frequency, as was done for the DSN link.

Table 4.1: DSS-17 Performance Metrics [Malphrus et al., 2018]

Performance Measure	**Performance Value**
X-band Uplink Range	7.145 – 7.235 GHz
X-band Downlink Range	8.350 – 8.500 GHz
LNA Noise Temperature	20 K
System Temperature Tsys	90 K
Antenna Gain	62.7 dBi (@8.4 GHz)
System Noise Spectral Density	-178 dBm/Hz
G/T at 5° Elevation	42.0 dBi/K
Time Standard	H-MASER (1ns/day)
EIRP	91.4 dBW (nominal)
HPBW	0.1150 deg
SLE Compliant	Yes
CCSDS Capable	Yes
Forward Error Coding	Reed Solomon/Convolutional, Turbo, Low Density Parity Check
Radiometric	Angle, Doppler, Sequential Tone and PN Ranging (2-Way and 3-Way)
Ranging Precision	+/-1 range unit (0.94 ns) 1 m (1 sigma Accuracy)

4.2 DSS-17 Tracking Performance Analysis

Since July 2022, DSS-17 has been performing radiometric tracking of the CAPSTONE mission. The Cislunar Autonomous Positioning System Technology Operations and Navigation Experiment (CAPSTONE) has the main objective of paving the way for future cislunar operations and navigation activities, but one of its secondary objectives is to assist the radiometric calibration of DSS-17, in order to improve its tracking performance when supporting deep space activities [Thompson and Rosen, 2022]. In particular, the station has not been previously used for precise radiometric tracking, and therefore its characteristics have not been experimentally validated. The most important of these is the station position, which affects the dynamics of the receiver and the Doppler measurements from satellites. As performed for SDSA, to improve the knowledge on a station characteristics and its differential tracking performance, concurrent three-way radiometric measurements should be used. Since DSS-17 is equipped with an X-band transponder, most of its tracking activities are performed in a Two-way configuration, with the station providing both the uplink and downlink. Given this situation, a preliminary investigative analysis of the tracking performance of DSS-17 has been performed. This consisted in the development of a simplified dynamical model to provide a preliminary evaluation of the limitations in

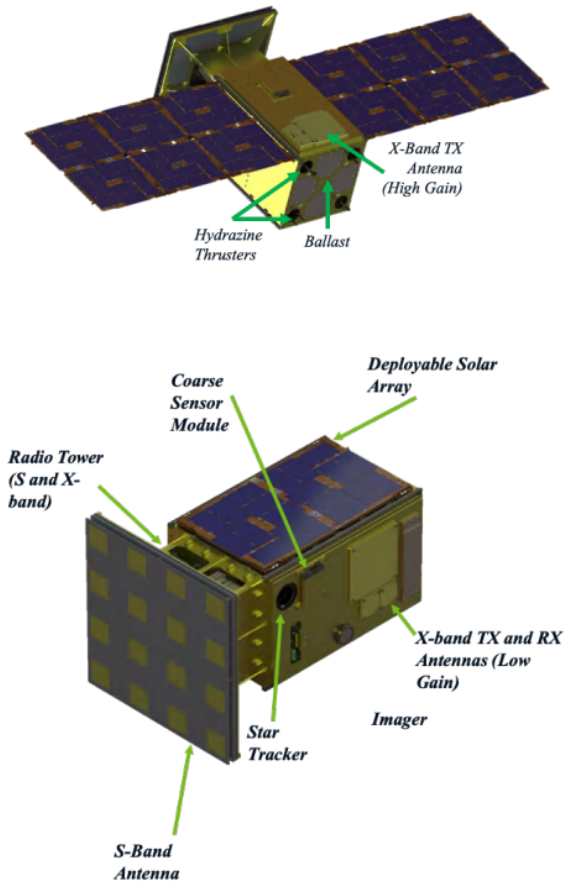

Figure 4.3: CAPSTONE spacecraft, courtesy of [Gardner et al., 2022].

the station's tracking accuracy. In particular, with the measurements available, the following limitations precluded the definition of an accurate dynamical model and systematic analysis of the tracking performance of the station:

- No raw data post-processing: Tracking accuracy is strongly dependent on the algorithm employed to generate the radiometric observables. Closed-loop receivers usually employ systems such as PLLs to process radiometric measurements. The result is a direct estimation of the phase difference of the residual signal, which provides no information on the noise levels at the front end and possibility in performing in-depth analysis of the radiometric data. Additionally, these systems are based on configuration parameters (e.g. loop bandwidth) that can change from station to station, making it difficult to perform direct a comparison between different receivers tracking at the same time.

- No tropospheric or ionospheric calibrations: As previously introduced, DSS-17 has not yet implemented weather monitoring systems or systems to estimate atmospheric delays on satellite links. In consideration of this limitation, only a seasonal statistical model can be employed to estimate the delay on the Doppler measurements, providing only rough accuracy to the dynamical model.

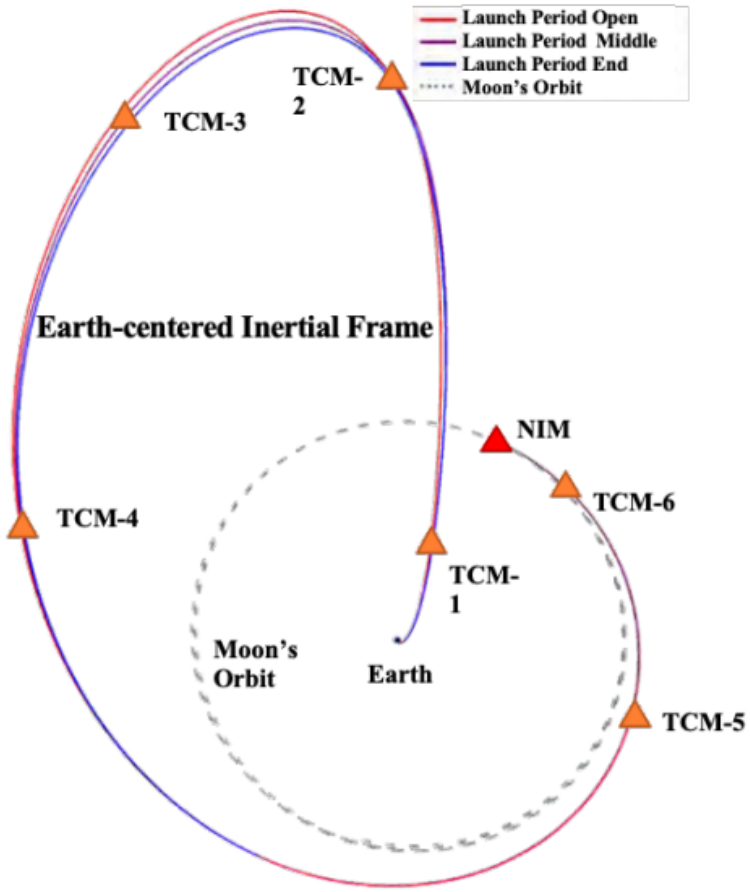

Figure 4.4: CAPSTONE spacecraft preliminary trajectory in the Earth-Centered EME 2000 frame, courtesy of [Gardner et al., 2022].

- Limited and ramped Three-way measurements: As most of the tracking activities are performed solely by DSS-17 the three-way radiometric observables are limited, making it difficult to perform orbit determination using data from multiple stations, and therefore improve the confidence on the position of DSS-17 and on its tracking performance. Additionally, three-way tracking activities require details on the ramped uplink signals required to make CAPSTONE's transponder lock onto the uplink carrier. As these data are not publicly available and ramps information cannote be recovered, the use of three-way measurements is prevented in the OD routine.

- Limited information on the state of the spacecraft: While information such as the spacecraft mass and geometry can be inferred, the dynamical state of CAPSTONE (e.g. current mass, maneuvers, attitude, state at the initial epoch) needs to be estimated or predicted from the mission phase. Predicted trajectories can be used to provide an initial state estimation to propagate, but as the mission evolves it's possible unplanned desaturation and/or orbit correction maneuvers are employed, changing the real state of the spacecraft from the predicted one, greatly increasing the uncertainties in the OD solution.

In consideration of the limitations described, a dynamical model was developed to investigate the performance of DSS-17 during early flight phases. In particular, the attitude

of the spacecraft was assumed to be fixed when transmitting, as expected to guarantee the correct pointing of the spacecraft directional antenna. With regard to the state of the spacecraft, this was recovered from the NASA/JPL Horizons On-Line Ephemeris System [Giorgini and Group, 2023]. For the filter, the following solve-for parameters were used:

- State of the spacecraft.
- SRP Scale.
- Troposphere zenith dry delay bias.
- Troposphere zenith wet delay bias.
- Ionosphere model daytime coefficient.
- Ionosphere model nighttime coefficient.

Given the deviation of the preliminary trajectory from the effective one due to operations, OD procedures were only possible on the first days of tracking, when the a-priori state of the spacecraft would be close enough to the effective one to allow for the linearization or the problem. Fig. 4.5 shows the residuals of the passes of CAPSTONE tracked with DSS-17 for two of the first days of operations (July 08, 2022, and July 10, 2022). Table 4.2 summarizes the root-mean-square of the single-arc analyses performed, with a count-time of 60 seconds. In consideration of the activities of the CAPSTONE being performed relatively close to the Moon-Earth system, the effects of the mission geometry on the tracking accuracy (e.g. SEP angle) can be considered negligible, and are therefore not analyzed.

Table 4.2: RMS of the residuals of DSS-17 tracking activities.

Tracking pass date	RMS [mm/s]
July 8, 2022	0.072
July 10, 2022	0.102

The mismodelling of tropospheric and ionospheric delays is visible especially when tracking at low elevations. To evaluate residual effects on the post-fit data, different cut-off antenna elevations were then used to only use Doppler measurements with small delay contributions from the atmosphere. Fig. 4.6 show the 1-second residuals for the tracking pass of July 08, 2022. As the cut-off elevation increases from 15 to 45 degrees, less Doppler measurements are available, but the residuals with a higher spread are removed from the analysis, making the residuals more stable in time.

Figs. 4.7 and 4.8 highlight the estimated Allan deviations of the residuals of the pass of July 08, 2022 with and without atmospheric delay estimations, respectively. As the number of measurements per pass is generally limited, oscillations at high integration times are expected. In consideration of the unavailability of precise atmospheric calibrations, the trend that is seen in the Allan deviations is as expected, especially at integration times

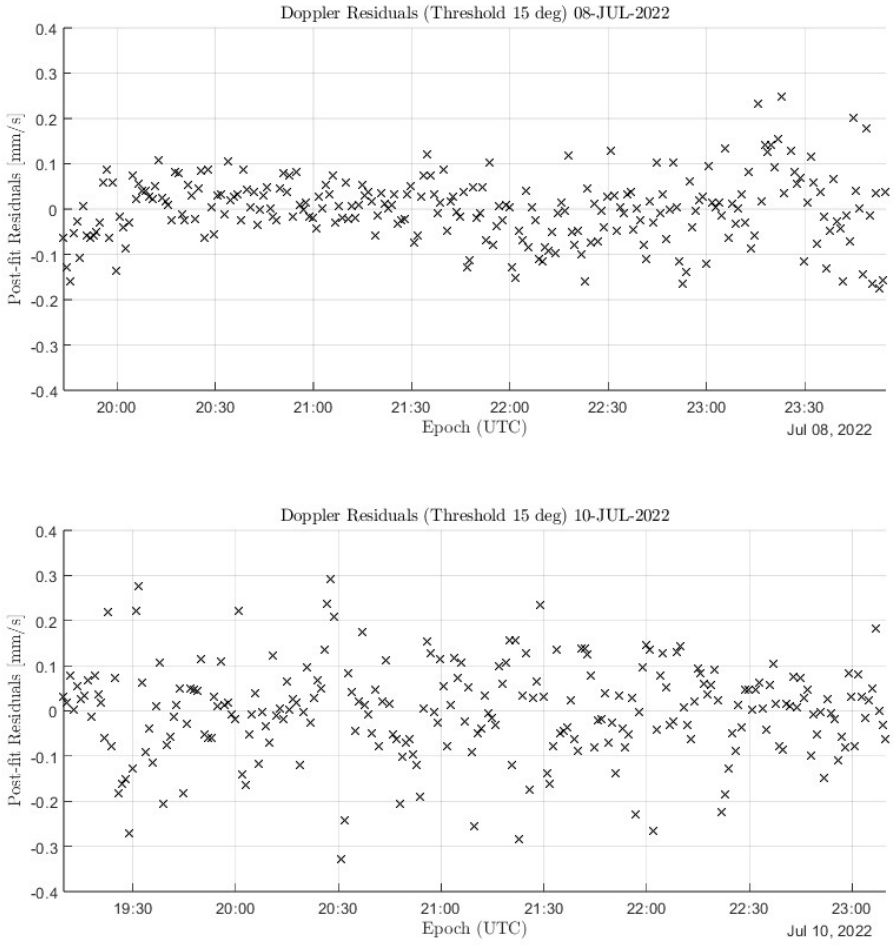

Figure 4.5: Residuals of the orbit determination procedure on the CAPSTONE Two-way Doppler measurements (60 seconds integration time).

higher than 10 seconds. The analysis of the frequency stability of the residuals is of great interest to characterize the performance of DSS-17. In particular, from this analysis it is possible to evaluate the goodness of future improvements at the stations to favour more accurate radiometric tracking. As is visible from the slope of the Allan deviation, the contribution of thermal noise is in the same order of magnitude of tropospheric noise even at low integration times. Given this, tropospheric noise can be considered the instability source affecting the residuals the most even at low integration times, therefore posing a lower limit on the tracking accuracy achievable when using this ground station. In particular, further improvements in the antenna noise figure are not expected to improve quality of tracking activities as long as atmospheric delay correction models are not available at the station.

In consideration of the results from the orbit determination of CAPSTONE using the radiometric measurements available, the average accuracy of radiometric tracking using DSS-17 can be preliminarly estimated at around 0.188 mm/s and 0.087 mm/s (1-sigma) at 1 and 60 seconds integration time, respectively. The difference in the tracking ac-

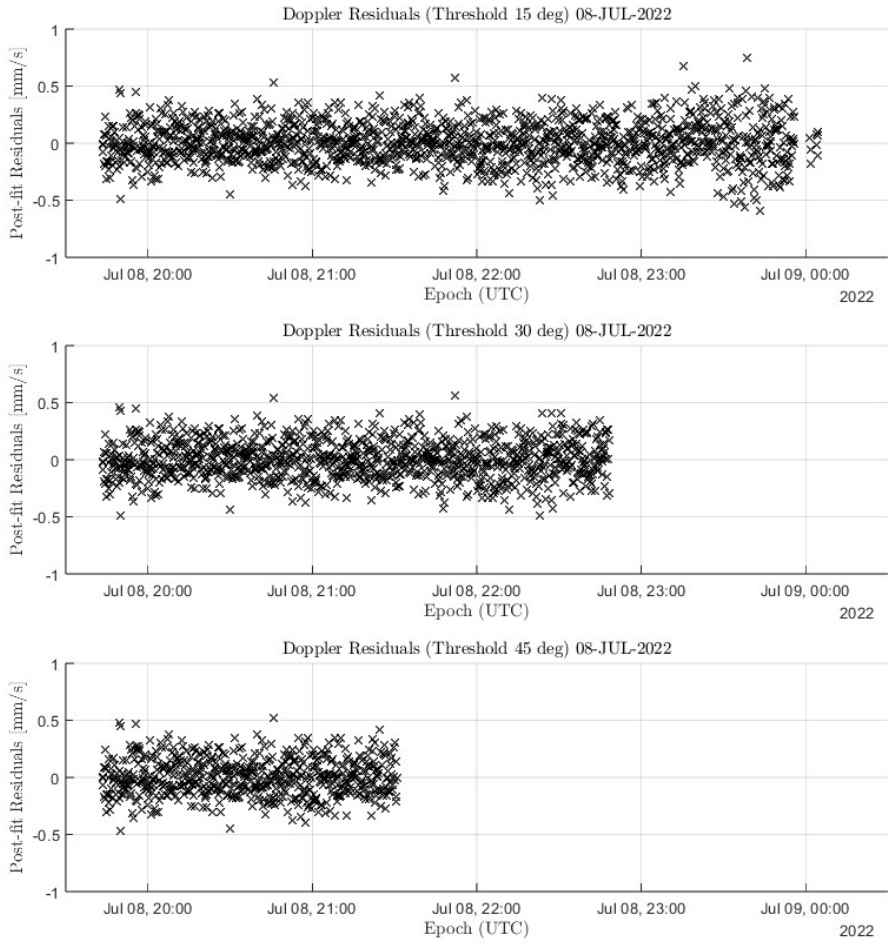

Figure 4.6: Residuals of the orbit determination procedure on the CAPSTONE Two-way Doppler measurements of July 08, 2022 when using different cut-off elevations.

curacy with respect to the DART and STERO-A missions, as reported by Pham, can be justified by a much lower distance, and therefore increased quality of the spacecraft-station transmission link. In addition, the results can be preliminary compared to those of [Thompson and Rosen, 2022], which reports the navigation results of CAPSTONE. There, a dynamical model without estimating the atmospheric delays is used, with the delays computed on a per-pass basis using data from nearby NOAA weather stations. The reported average 1σ noise from the navigation activities is 0.0058 Hz at a 10 seconds count time. In comparison, orbit determination procedures on the two processed passes is 0.0053 Hz at the same count time, showing coherent results.

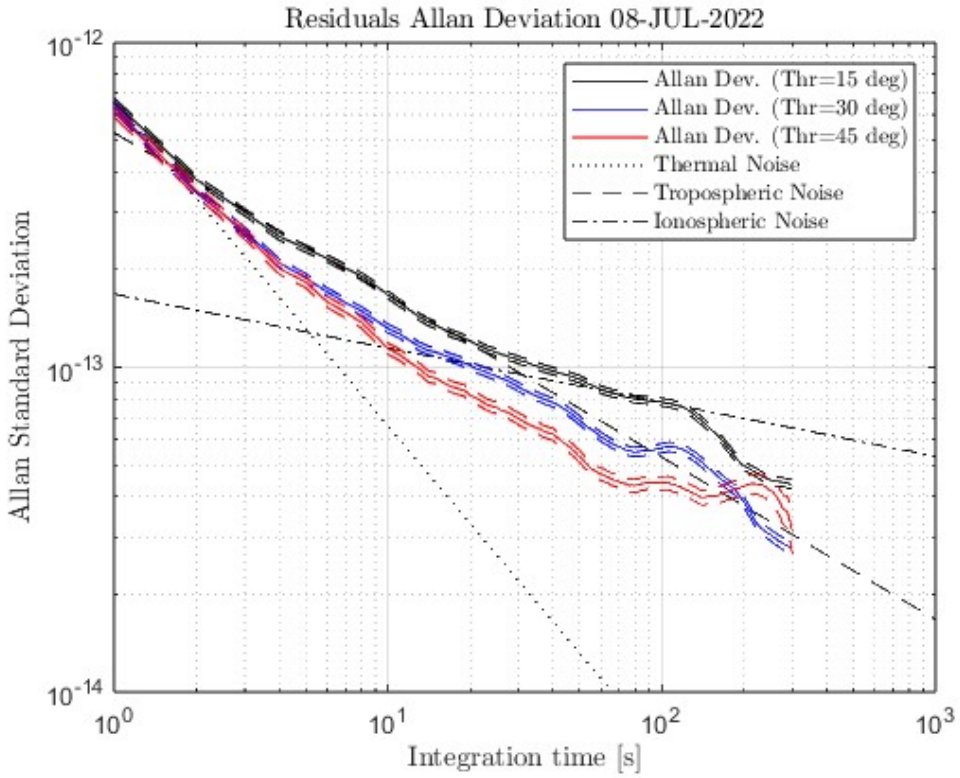

Figure 4.7: Allan deviation of the orbit determination residuals and noise models (July 08, 2022) with media delay estimations.

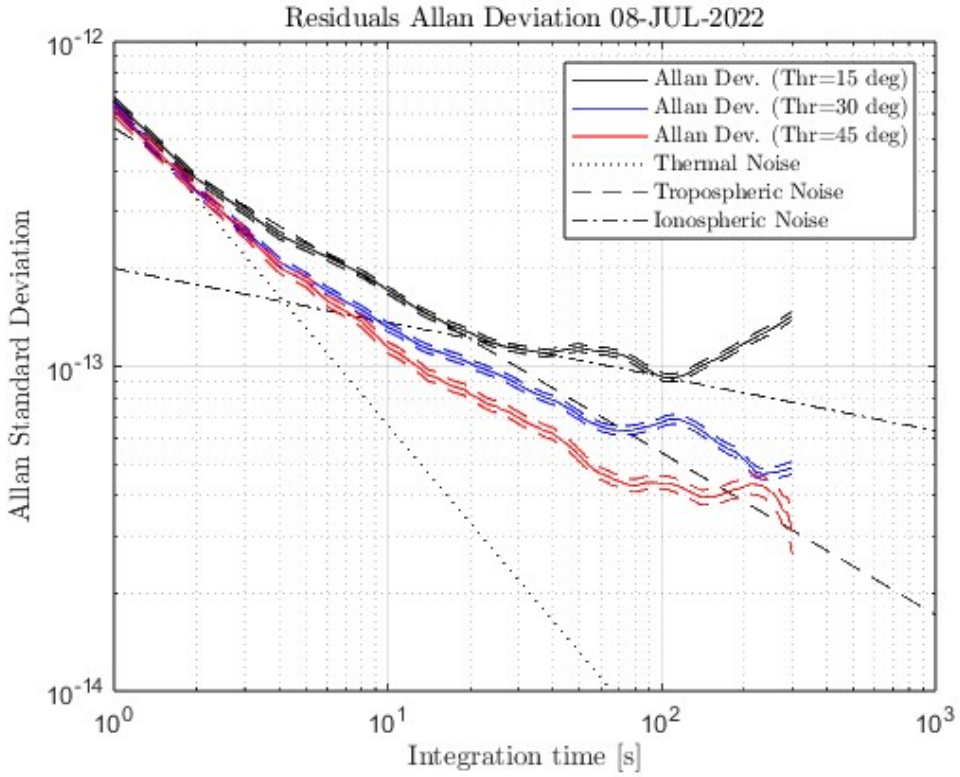

Figure 4.8: Allan deviation of the orbit determination residuals and noise models (July 08, 2022) without media delay estimations.

4.3 The Open-Loop Receiver Design

As described in section 4.1, DSS-17 currently only has the capability of acquiring closed-loop signals through the DSN DTT. The DTT extracts the carrier phase with a digital PLL and performs TM demodulation when required [Chang, 2015]. By tracking the phase of the IF signal, it is then possible to recover the sky frequency by knowing the settings of the mixer and performing navigation activities.

Closed-loop acquisitions are ideal for tracking operations in nominal conditions, but can create a loss of data when there are fluctuations in the signal power, or unexpected frequency variations are present [Thornton and Border, 2003, Buccino et al., 2018, Buccino et al., 2022]. In this context, the employment of open-loop receivers (OLR) for data recording and successive processing is preferred. The digitalization of the analog signal at the IF is performed inside of the DTT, but no signal recording is carried out. In consideration of this, no post-processing can be performed with the current hardware configuration of DSS-17.

While extensively used, PLLs have drawbacks when employed in carrier-tracking, especially when an uncompensated Doppler effect is present, which usually happens in radio science experiments during acquisition, or during the initial spacecraft operations when an initial acquisition is required. Even though the parameters of a PLL can be set before starting to receive data, the carrier synchronization (or lock) of the PLL requires some time. Therefore, this system is not ideal for tracking under non-nominal conditions or when variability in the signal is expected. Additionally, to perform some remote sensing investigations, the ability to post-process data and perform a spectral analysis is a requirement. Examples of these investigations are heliophysics experiments [Morabito et al., 2003], atmospheric occultations [Tyler et al., 1989], or planetary surface analysis [Simpson et al., 2011].

In this context, the tracking activities of DSS-17 have been supported by designing a flexible and modular open-loop interface that can be easily disconnected and reconnected to the acquisition chain, in order to avoid any alteration of the downlink signal when only the DTT is required for operations. The designed OLR is based on a Software-Defined Radio (SDR), in consideration of the advantages of having a reconfigurable and flexible interface. An SDR is a system where the analog processing of signals, which is usually performed via hardware, is instead performed through software, thanks to the processing power of a workstation to which the SDR is connected. As SDR can be reconfigured and updated, the employment of an SDR makes the design more cost-efficient, and provides downsizing of the overall system. On the contrary, traditional radios rely on complex hardware and fixed designs, require experience with analog systems and can be subjected to degradation with the aging of the components [Maheshwarappa and Bridges, 2014]. Given the possibility of creating adaptive communication systems, SDRs have also been adopted by satellites, with the first fully SDR commercial satellite launched in 2021 [Abbas and Asami, 2021]. This translates to the possibility of upgrading the transmission capabilities of the space segment mid-mission, bringing forward the necessity of having a similarly flexible receiver on the ground. Given the flexibility of this archi-

tecture, there are already multiple ground stations operating with SDR-based receivers [Mladenov et al., 2020, Summers et al., 2018, Hitefield et al., 2016, Simpsona, 2019].

With respect to Fig. 4.2, Fig. 4.9 presents schematically the components and the information flow through the OLR prototype. Being located after the LNA & RF/IF block, the OLR works with an IF signal after it is split and sent in two parallel paths by an Active Multicoupler (AMC). When the OLR is connected, a second amplification after the LNA in the antenna is performed by an Amplifier (AMP) to satisfy the sensitivity of the Software-Defined Radio (SDR) employed. Inside this final component, the analog signal is digitalized and passed to the processor, which in turn performs the final steps of digital processing and stores the received data. At the same time, the signal is transmitted to the DTT for usual processing. On the contrary, when the OLR is not employed, it can be disconnected, and the original signal transmitted without losses to the DTT.

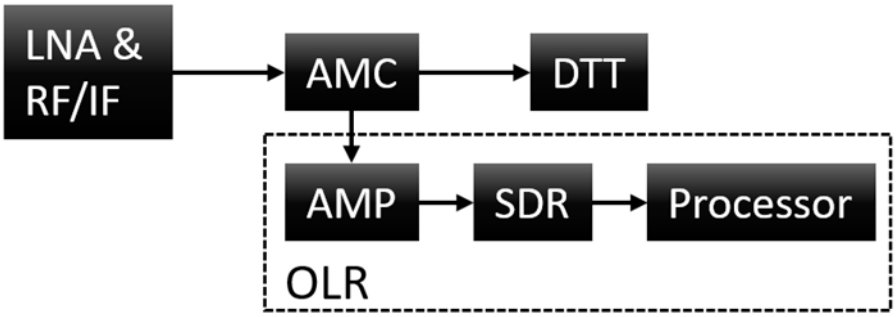

Figure 4.9: Functional architecture of the proposed open-loop interface.

4.3.1 Preliminary Design

The design of the open-loop interface was performed in consideration of making it an additional capability to the station, and therefore keeping the possibility of using the DTT as a stand-alone system. The components selected for the open-loop interface, therefore, make it possible to process the received signal without interfering with the one received at the DTT. The AMC implemented is the MCA202M from Stridsberg Engineering. As the signal power is divided and sent through two different acquisition chains in parallel, both of the receivers would see half of the original power. Without an active compensation, as implemented by the AMC, both the DTT and the SDR would receive a signal with a power 3.01 dB lower than the original one, in consideration of the halving caused by dividing the signal. This negative effect is reduced by the amplification in the AMC, which can generate a net amplification of up to +2 dB. In consideration of the band-pass filtering at the IF, the AMC was chosen in the VHF/UHF range, as shown in Table 4.3. The choice of the most appropriate SDR depends on what activities should be performed by the receiver. Given the flexibility of the software implementation, SDR can easily implement demodulators to receiver TM, and even transmit TC if they have a full-duplex architecture. For the implementation at DSS-17, these features are not required, since the current architecture employed is capable of managing both TM and TC. Similarly to other open-loop receivers, the objective of this subsystem is to select one or more channels

Figure 4.10: Active Multicoupler MCA202M.

inside of a pre-defined bandwidth to record and store what is received for later digital processing.

Table 4.3: MCA202M RF properties

Frequency Range	25 MHz to 1 GHz
Nominal Impedance	50 ohm
Port-To-Port Isolation (min)	22 dB
Return Loss (all ports)	>20 dB
P1dB	17 dBm
3OIP	32 dBm
Coupler Gain/Loss	+2 dB to -1 dB

Fig. 4.11 shows the conceptual steps in the signal acquisition and recording of data using DSN's Radio Science Receiver, which was the starting point for designing the software-based processing steps of the OLR to be developed. Current DSN open-loop recordings capabilities for radio science applications consist in up to 4 channels with bandwidths between 1 kHz and 16 MHz, and at a depth of up to 32-bit per sample (16-bit in-phase and 16-bit quadrature) [Asmar et al., 2014]. As the digitized signals are at the IF (about 300 MHz), every open-loop recorder must implement strategies to perform filtering and decimation. The simplest implementation of an OLR in fact is to receive the IF analog signal and to perform digitalization and successive decimations, or under-sampling, of the signal. With regard to the required bandwidth, this will be strongly dependent on the precision of the predicted orbit: for a precise Doppler pre-steering of the uplink signal, the residual frequency after mixing the downlink leg with the reference signal would be around 0 Hz.

With these considerations, the selected component for the preliminary design was the HackRF One (Great Scott Gadgets). This low-cost SDR has an operating frequency from

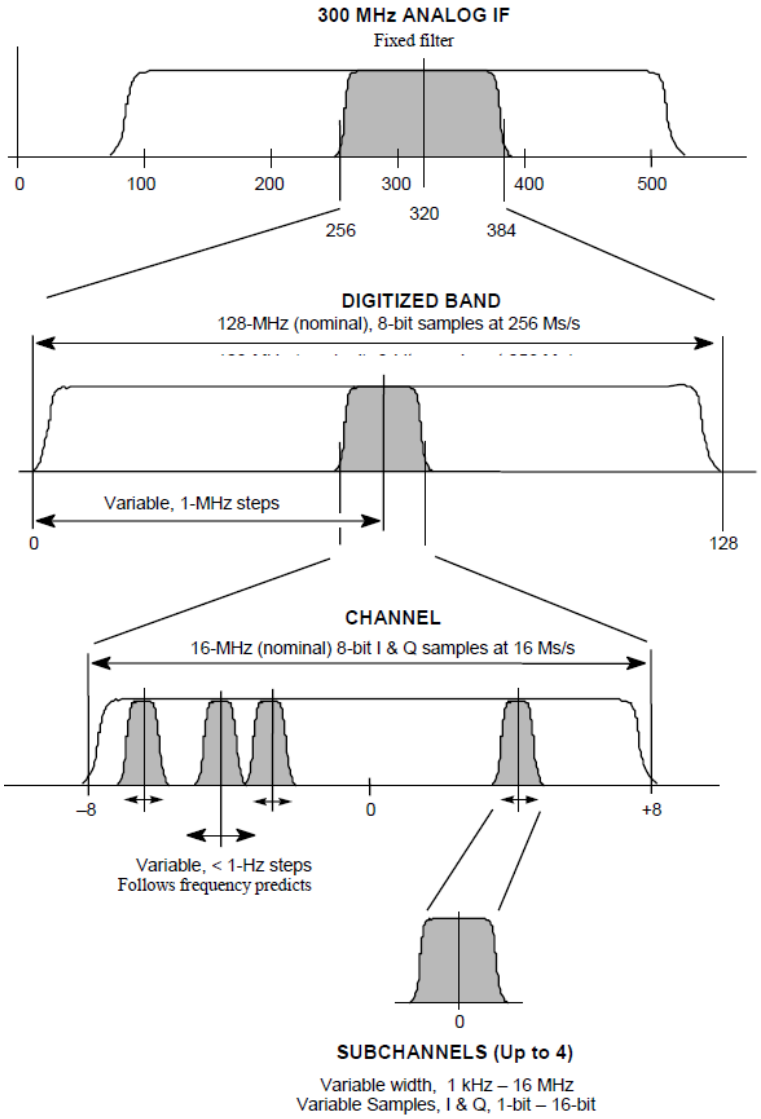

Figure 4.11: Radio Science Receiver Recording Steps.

1 MHz to 6 GHz, a half-duplex architecture, and can record up to 20 Msps at 16-bit (8-bit in-phase and 8-bit quadrature components). This translates into a maximum data-rate of 320 Mbps, which can be supported by both USB and SATA interfaces. The main concern when choosing the most appropriate SDR, since the downlink signals are very weak, is the sensitivity of the receiver. Tests performed in [Perotoni and dos Santos, 2021] report the noise floor of the HackRF one ranging from -83 dBm to -70 dBm in the interval 0-2000 MHz at different bandwidths. The variability is expected, as oversampling reduces the Signal-to-Quantization-Noise Ratio (SQNR), and the results are in accordance to the dependency of the SQNR on the number of bits N, the sampling frequency f_s, and the bandwidth B, as defined in Eq. 4.1 [**?**].

$$\text{SQNR} = 6.02N + 1.76 + 10\log_{10}\frac{f_s}{2B} \tag{4.1}$$

Finally, the AMP in the acquisition chain depends on the link budget of the spacecraft

to be tracked, and on the SDR employed. During the tracking of deep space missions, such as CAPSTONE, the front-end was reported to receive variable powers, from -150 dBm to -100 dBm. In consideration of the presence of an LNA before the down-conversion to IF, and the acquisitions at the DTT, the nominal values considered for the design procedures were between -100 dBm and -50 dBm when entering the OLR chain. This range was then compared to the sensitivity of the chosen SDR to guarantee a sufficient margin during tracking activities. For correct signal detection, the difference between the signal power and the noise floor must be at least 10-15 dB, but a higher SNR improves the accuracy in the generation of the radiometric observables [Togni et al., 2021], therefore the AMP was chosen to provide a gain of 30-40 dB. This gain can then be finely tuned by the analog amplifier of the HackRF One to avoid saturation. In fact, it must be noted that too much input power to the receiver could create distortions and spurious frequencies [Handel and Zetterberg, 2009], and therefore it is not possible to arbitrarily increase the gain before the SDR.

Fig. 4.12 shows the processing algorithm of the raw data acquired by the SDR developed using GNU Radio companion. While only one recording channel with a bandwidth of 10 MHz is setup, the versatility of SDR makes it possible to extend this recording capability to multiple channels. The proposed processing algorithm consists in the acquisition of data at the highest sampling rate possible to minimize the signal-to-quantization-noise. The effective recording bandwidth is then obtained by appropriate mixing and filtering. Each channel (one, in this example) is accompanied by a supporting sub-channel with an offset in frequency. This choice is made in consideration of some SDR (including the HackRF) having a DC spike at the reference frequency used to down-convert the received signal. By applying a band pass filter on the receiving channel and moving the support channel by a known value, it is then possible to filter this spike in both of them, and recover the data from the supporting channel when it is filtered in the main one. Finally, the flexibility of a software implementation makes it possible to dynamically change the center frequency at which the receiver is operating. This makes the open-loop receiver a complementary subsystem to the DTT closed-loop receiver currently employed at DSS-17, as it can support initial detection and acquisition of the downlink frequency by changing its center frequency to observe the whole pass band of the RF receiver. By using a HackRF as SDR, the current maximum bandwidth is limited to 20 MHz, while the down-converted IF from the front end has a range of 100 Mhz, which can be observed in a matter of seconds thanks to the features of software-defined receivers.

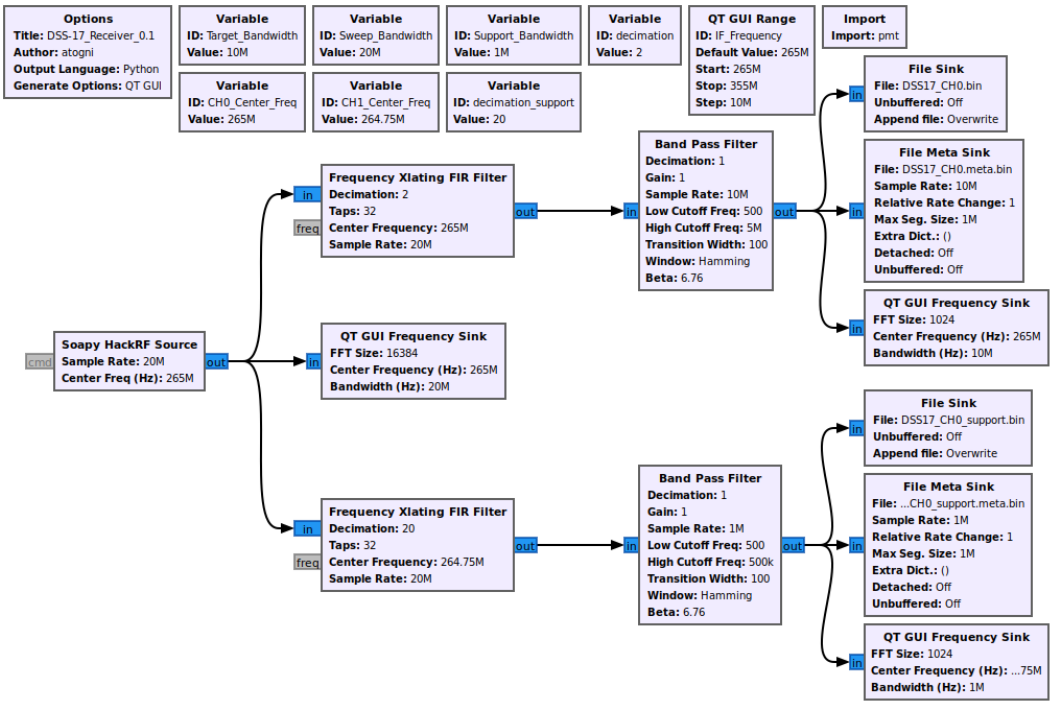

Figure 4.12: Raw measurements processing algorithm of the open-loop receiver, as developed with GNU Radio companion.

4.3.2 Testing Activities

Before the installation of the OLR in the DSS-17 acquisition, the selected components were tested singularly and together to validate the theoretical considerations and estimate the predicted losses during tracking activities.

The HackRF One was tested to validate the numbers reported in [Perotoni and dos Santos, 2021] and to verify its sensitivity. To do so, an X-band signal generator was used to simulate a signal at 1 GHz. While performing an analysis far from the expected IF of around 300 MHz is not ideal, the results could be used as a reference to evaluate at which power level signals can be detected, and when spurious frequencies start to appear due to saturation in the receiver. The analysis was performed by generating a signal with a power ranging from -110 dBm to 0 dBm with a 10 dB step, which was the available resolution of the generator. While the threshold of 0 dBm was identified in consideration of the maximum input power allowed by the HackRF One, given the strong deviations from linearity after a signal power of -50 dBm (see Fig. 4.13) the test was interrupted at a power level of -20 dBm.

Once started, the digital acquisition would record a ramped signal at 20 Msps with a variation in power of 10 dB every 15-20 seconds. The signal was then filtered and under-sampled to record a bandwidth of 20 kHz. Given these durations, it was possible to perform multiple estimations of the signal power and the noise floor through spectral analysis, averaging multiple estimations at each power level and obtaining a more accurate estimation. The focus on spectral analysis is given by the availability and widespread employment of Doppler observables in radiometric tracking. Additionally, the OLR can be

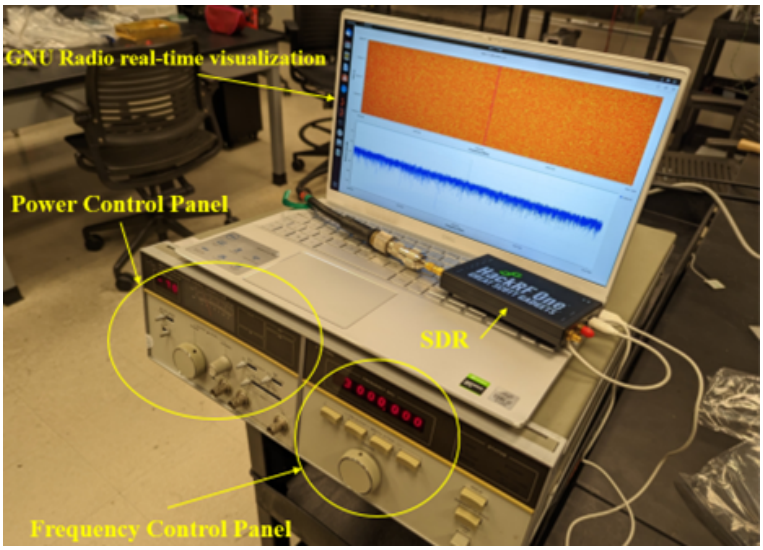

Figure 4.13: Experimental setup for SDR sensitivity testing.

used independently from the DTT, but both share the same initial acquisition procedures: while the OLR records the signal in the I&Q form to perform successive spectral analysis, the PLL in the DTT requires to be initialized before acquiring the carrier and performing tracking activities. In this context, the OLR can act as an extension of the DTT by performing real-time spectral analysis in a wider bandwidth (up to 20 MHz) than the one available at the DTT, to support carrier acquisition and provide an increase in performance when doing initial acquisitions of spacecraft. The power and noise floor estimations were performed using the algorithm described in [Togni et al., 2021]. By performing an accurate frequency estimation, the algorithm can provide a precise estimation of the noise floor as well, through the implementation of the DFT.

While not being concerned with the absolute value of the noise floor estimated through the SNR, the objective of the analysis was to evaluate the range of input power for which the peak is detectable and increases linearly when performing spectral analysis. The lower and upper values of this interval would provide the sensitivity of the receiver and the input power for which spurious frequencies start to appear. The algorithm employed estimates the frequency and power of a monocomponent signal, and the noise floor of its power spectrum. Since this method can be tuned to observe a smaller bandwidth than the one available, the effect of non-linear distortions (see Fig. 4.14) could be filtered. Nevertheless, due to the saturation of the receiver, P_c/N_0 deviations from a linear increase of the P_c/N_0 with the input power can still be appreciated. In other words, the leakage of power to other frequency components due to the saturation of the receiver is detected as a deviation of the SNR from linearity. Fig. **??** shows examples of estimated amplitude spectra at input powers of -80 dBm and -20 dBm. At the lower input power, the signal is easily detectable, with an estimated P_c/N_0 of around 31 dBHz, and therefore guaranteeing an appropriate margin for tracking and the accurate generation of Doppler observables. At the -20 dBm level, the observables P_c/N_0 is approximately 49 dBHz. Since the noise floor was only estimated around the frequency signal, the non-linear distortions due to saturation do not

directly affect the estimation by contributing to the noise power estimation, but the power at the signal frequency cannot increase further, therefore the deviation from the expected linear P_c/N_0 increase is justified, and is shown in Fig. 4.15.

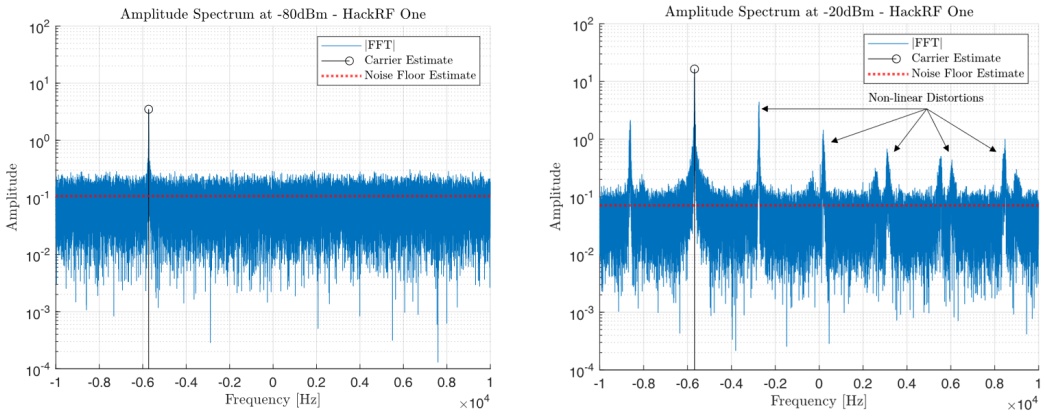

Figure 4.14: Computed spectra from the signal generator at different input power.

Fig. 4.15 shows the result of the sensitivity analysis performed. The estimated linearity of the estimated P_c/N_0, given variable input power, ranges from -100 dBm to -60 dBm. Even though the power resolution was limited, multiple estimations at the same input power values were considered to increase the confidence in the model. When the input power is lower, due to the statistical nature of noise, the estimation algorithm saturates at approximately 10 dBHz when estimating the signal power over the noise floor and the signal is not detectable. Over 60 dBm the estimated SNR does not increase linearly, and decreases as the input power keeps increasing. This suggests the leakage is greater than the increase in the recorded power, and therefore the SDR does not perform nominally.

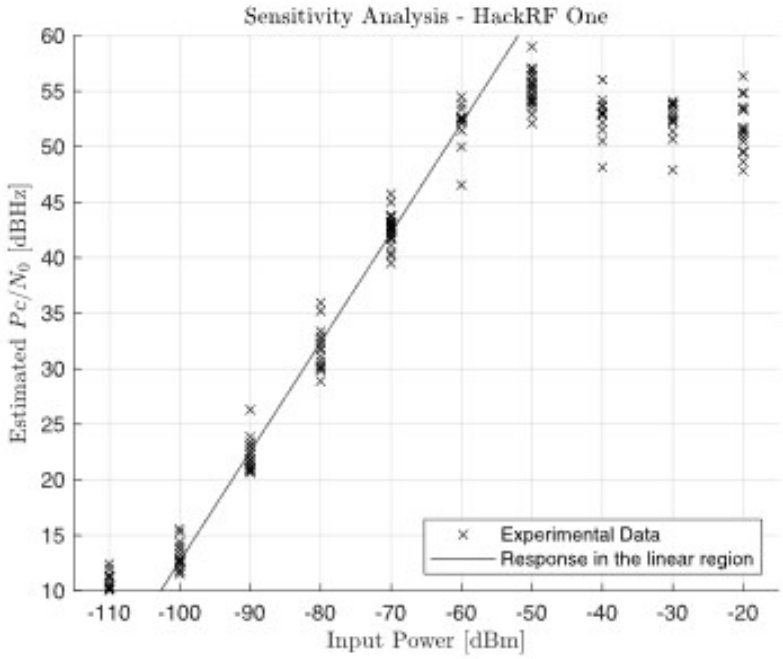

Figure 4.15: Experimental P_c/N_0 as the input power to the receiver changes dynamically.

After testing the sensitivity of the SDR, the AMC and the acquisition chain were tested. To do so, the HackRF One was configured for transmission, with the AMC connected to a spectrum analyzer. By keeping a constant transmission gain and changing the transmission frequency, it was possible to characterize the gain effectively provided by the AMC in the range of frequencies covered by the IF band-pass filter. Table 4.4 reports the results of the tests, when using the AMC together with coaxial RF cables.

Table 4.4: Experimental transmission gains.

	275 MHz	**300 MHz**	**325 MHz**
P1	2.9 dB	2.9 dB	2.4 dB
P2	2.9 dB	2.9 dB	2.4 dB

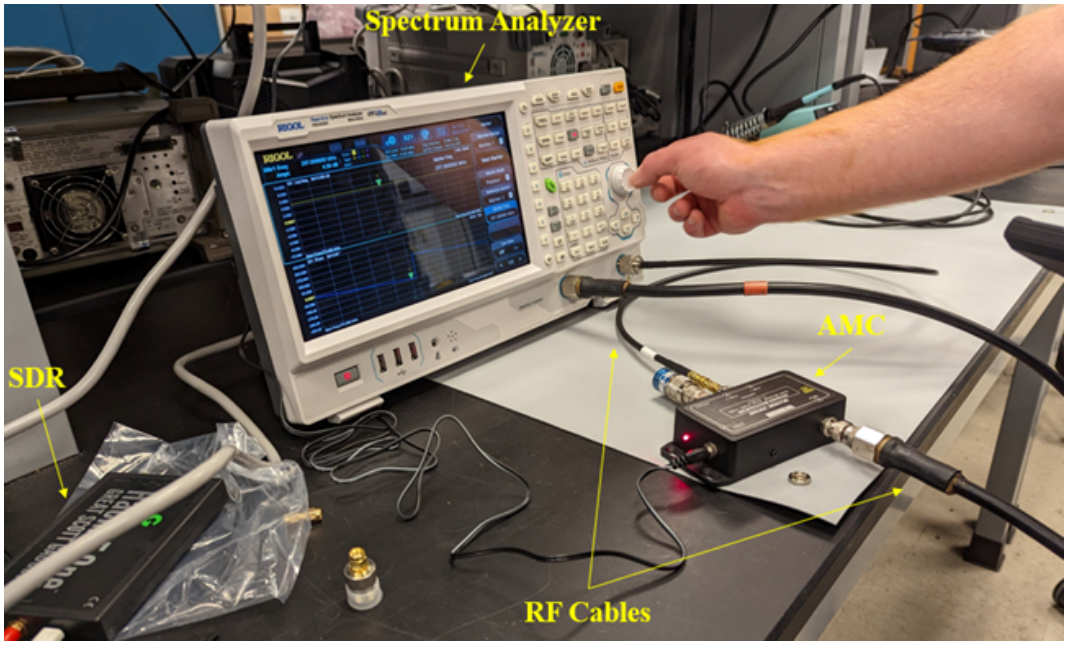

Figure 4.16: Experimental setup, spectrum analyzer and transmission components.

In particular, the experimental gains of the AMC were computed by considering a reference signal at different frequencies, and by considering the difference in the SNR obtained at the spectrum analyzer with and without the AMC. Fig. 4.17 shows the schematics of the experimental setup. The results in Table 4.4 come from the computation of the difference between the baseline transmission path L0-L2-L3, and the transmitted signals after amplification from the two AMC ports, L0-L2-P1-L3, and L0-L2-P2-L3.

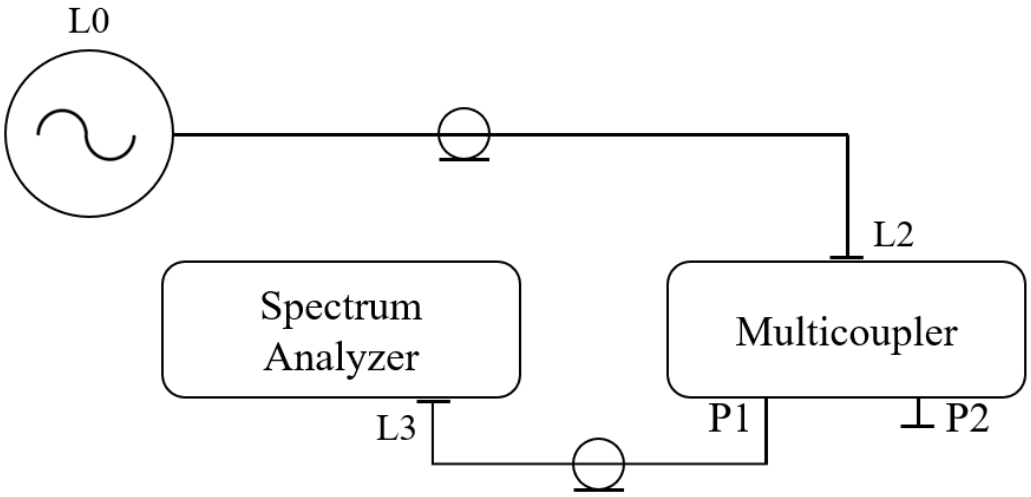

Figure 4.17: Experimental setup, schematics.

Chapter 5

Conclusions and Future Research Directions

The work presented in this dissertation revolves around three main research topics, which contextualize the complexity of defining a clear methodology to evaluate the performance of ground segments in support of radio science experiments, from signal acquisition and processing, to the computation of the noise sources affecting the link and isolation of antenna contributions after performing the orbit determination routines. As ground stations provide the common infrastructure for navigation activities, and operations generally involve multiple ground complexes, the definition of a technical framework to evaluate and compare tracking performance is a timely and crucial problem for radio science activities involving spacecrafts. To address this complexity, the following three research directions taken are described and discussed:

- Development of accurate processing routines for radiometric observables generation: open-loop receivers allow the most flexibility in radio science applications, but only provide raw data. To maximize the scientific return of radiometric measurements, a general-purpose DSP algorithm was developed and completely characterized in terms of accuracy of estimation. In consideration of the limited literature results available on signal detection thresholds, these are also evaluated analytically and experimentally to generate detection maps and models to predict the correctness of frequency estimation and generation of Doppler observables when dealing with radiometric measurements. The definition of a standard pipeline for the conversion of the recorded antenna voltages makes it possible to avoid the introduction of processing noise when dealing with measurements from open-loop receivers, and define standard best-practices. This is valid especially for transmissions with a relatively low-power carrier and with variable residual frequencies, where the proper definition of the processing parameters can greatly affect the accuracy of tracking activities. To achieve this characterization, effort has been put in the development of a simulator of random and non-stationary signals. With this tool it's then been possible to perform a statistical investigation on the accuracy and performance of the developed algorithm for Doppler radiometric tracking. Simulations show the devel-

oped estimator is unbiased and competitive with existing methods, asymptotically reaching the theoretical minimum variance of frequency estimation. Additionally, quantitative investigations on the detection of weak signals in radiometric tracking generated best-fit models to predict outliers and the applicability of FFT-based signal acquisition methods, which are used widely in tracking operations. Given its validated performance through simulation, the developed algorithm is currently employed for radio science investigations, but future improvements could focus on a differential performance characterization with respect to other methods employed in radio tracking, such as PLL, which are instead limited by phase estimation bounds. Additionally, the employment of windowing functions to effectively increase the frequency estimation accuracy at high count times is yet to be fully characterized, but could improve the quality of frequency estimations, and therefore of Doppler observables in tracking activities.

- Characterization of the radiometric performance of DSS-69: the state-of-the-art radio-telescope of SDSA is an important infrastructure that can benefit deep space missions by supporting the tracking activities of the DSN and others. The design of a standardised methodology for station performance evaluation in deep space tracking is critical, in consideration of the current trend of expansion of space missions. Only limited studies have been conducted on techniques to validate the accuracy in radiometric of deep space stations, relying mostly on single-subsystem analyses. In particular, no direct and systematic comparison between the tracking accuracy of different stations is usually performed in support of their performance characterization. With this work, by extending the analysis of validated models for error sources in deep space tracking activities to account for unknown station contributions, it's possible to quantify the ground stations performance and provide insights on the stability and quality of the transmission links. To characterize the tracking performance of the SDSA complex, 3-way data from the Juno spacecraft orbiting Jupiter have been used. To this end, the differential tracking performance of SDSA and Madrid's DSN complex stations has been processed using multiple passes and a multi-arc strategy. The observables generated through the processing of the data were used to compute Doppler residuals through the Caltech/JPL's orbit determination toolkit MONTE. From the residuals, characteristic metrics about the downlink frequency stability were extracted to provide information on the capabilities of SDSA, such as the RMS and Allan Variance of the residuals and noise contributions. Different hardware configurations and tracking strategies have been tested in order to evaluate the effect of the active surface compensation as well as the goodness of the tracking accuracy. Unfortunately, the measurement campaign was prematurely stopped due to an antenna extraordinary maintenance and only a rough accuracy in data analysis was achieved. While further data acquisition is required to characterise the non-nominal configurations described above, the results and metrics provided for the nominal configuration show that the performance of SDSA is appropriate for deep space tracking and to support radio science experiments in the Solar System.

- Development of subsystems and analysis of radiometric data with DSS-17: DSS-17, one of the new assets of DSN, is currently involved in the radiometric tracking of deep space missions. Its performance has been preliminary characterized by performing orbit determination on deep space spacecraft (DART, STEREO-A) in parallel to other DSN stations, but no analysis on error sources has been performed on spacecraft operating in the cislunar space, especially in consideration of the planned involvement of DSS-17 for future Artemis missions. As expected by its smaller reflector and higher system temperature, the tracking accuracy of the station is estimated to be lower than other BWG DSN antennas. In this context, an investigative analysis on the performance of the station has been performed using some of the available radiometric measurements from the CAPSTONE mission. Currently, no local atmospheric delay calibrations are available, and results confirm this is in fact the limiting factor in tracking and navigation accuracy, even at count times where thermal noise should be the dominant error source. Further investigations should refine the modelling of the station and the local atmosphere to develop more accurate dynamical models. The employment of Three-way measurements would also greatly improve the confidence on the station's position and internal delays. In addition, an improvement in the receiving capabilities of DSS-17 would make it possible to perform a direct comparison between radiometric measurements received from other stations using the same processing pipeline. To this end, the design of a modular open-loop receiver was performed, identifying the most appropriate components to add this capabilities to DSS-17 without affecting the quality of the data received by the DTT. As the station involvement in tracking activities for the DSN did not make it possible to test the receiver when inserted in the acquisition chain, further activities should focus on validating the acquisition algorithms developed using real radiometric data, as well as identifying specialized hardware to ensure no artifacts and clock instabilities are present in the open-loop acquisition chain. Once its performance has been validated, the modularity and flexibility of chosen design make it possible to replicate it at other stations, making SDR-based open-loop receivers easily available at multiple stations involved in deep space tracking.

List of Figures

List of Tables

Bibliography

[Abbas and Asami, 2021] Abbas, Y. M. and Asami, K. (2021). Design of software-defined radio-based adaptable packet communication system for small satellites. Aerospace, 8(6):159.

[Asmar et al., 2005] Asmar, S., Armstrong, J., Iess, L., and Tortora, P. (2005). Spacecraft doppler tracking: Noise budget and accuracy achievable in precision radio science observations. Radio Science, 40(2):1–9.

[Asmar et al., 2014] Asmar, S., French, R., Marouf, E., Schinder, P., Armstrong, J., Tortora, P., Iess, L., Anabtawi, A., Kliore, A., Parisi, M., et al. (2014). Cassini radio science user's guide.

[Asmar, 2022] Asmar, S. W. (2022). Radio science techniques for deep space exploration. John Wiley & Sons.

[Asmar et al., 2017] Asmar, S. W., Bolton, S. J., Buccino, D. R., Cornish, T. P., Folkner, W. M., Formaro, R., Iess, L., Jongeling, A. P., Lewis, D. K., Mittskus, A. P., et al. (2017). The juno gravity science instrument. Space Science Reviews, 213:205–218.

[Athley, 2002] Athley, F. (2002). Performance analysis of doa estimation in the threshold region. In 2002 IEEE International Conference on Acoustics, Speech, and Signal Processing, volume 3, pages III–3017. IEEE.

[Bertotti et al., 1993] Bertotti, B., Comoretto, G., and Iess, L. (1993). Doppler tracking of spacecraft with multi-frequency links. Astronomy and Astrophysics (ISSN 0004-6361), vol. 269, no. 1-2, p. 608-616., 269:608–616.

[Best, 2007] Best, R. E. (2007). Phase-locked loops: design, simulation, and applications. McGraw-Hill Education.

[Boashash, 1992a] Boashash, B. (1992a). Estimating and interpreting the instantaneous frequency of a signal. i. fundamentals. Proceedings of the IEEE, 80(4):520–538.

[Boashash, 1992b] Boashash, B. (1992b). Estimating and interpreting the instantaneous frequency of a signal. ii. algorithms and applications. Proceedings of the IEEE, 80(4):540–568.

[Boashash, 2015] Boashash, B. (2015). Time-frequency signal analysis and processing: a comprehensive reference. Academic press.

[Bolton et al., 2017] Bolton, S., Lunine, J., Stevenson, D., Connerney, J., Levin, S., Owen, T., Bagenal, F., Gautier, D., Ingersoll, A., Orton, G., et al. (2017). The juno mission. Space Science Reviews, 213:5–37.

[Brent, 2013] Brent, R. P. (2013). Algorithms for minimization without derivatives. Courier Corporation.

[Buccino, 2021] Buccino, D. (2021). Olr processing and frequency resolution. unpublished.

[Buccino et al., 2022] Buccino, D., Border, J. S., Folkner, W. M., Kahan, D., and Le Maistre, S. (2022). Low-snr doppler data processing for the insight radio science experiment. Remote Sensing, 14(8):1924.

[Buccino et al., 2021] Buccino, D., Kahan, D., Parisi, M., Paik, M., Barbinis, E., Yang, O., Park, R., Tanner, A., Bryant, S., and Jongeling, A. (2021). Performance of earth troposphere calibration measurements with the advanced water vapor radiometer for the juno gravity science investigation. Radio Science, 56(12):e2021RS007387.

[Buccino et al., 2018] Buccino, D. R., Kahan, D. S., Yang, O., and Oudrhiri, K. (2018). Extraction of doppler observables from open-loop recordings for the juno radio science investigation. In 2018 United States National Committee of URSI National Radio Science Meeting (USNC-URSI NRSM), pages 1–2. IEEE.

[Buffa et al., 2016] Buffa, F., Bolli, P., Sanna, G., and Serra, G. (2016). An atmosphere monitoring system for the sardinia radio telescope. Measurement Science and Technology, 28(1):014004.

[Candan, 2011] Candan, C. (2011). A method for fine resolution frequency estimation from three dft samples. IEEE Signal processing letters, 18(6):351–354.

[Candan, 2015] Candan, Ç. (2015). Fine resolution frequency estimation from three dft samples: Case of windowed data. Signal Processing, 114:245–250.

[Chang, 2015] Chang, C. (2015). Dsn telecommunications link design handbook. DSN Document, 373(810–005).

[Chen et al., 2020] Chen, Y., Ko, A. H. C., Tam, W. S., Kok, C. W., and So, H. C. (2020). Non-iterative and accurate frequency estimation of a single cisoid using two dft coefficients. Digital Signal Processing, 98:102652.

[Curkendal and McReynolds, 1969] Curkendal, D. and McReynolds, S. (1969). A simplified approach for determining the information content of radio tracking data. Journal of Spacecraft and Rockets, 6(5):520–525.

[Curtis, 2013] Curtis, H. (2013). Orbital mechanics for engineering students. Butterworth-Heinemann.

[Doody, 2011] Doody, D. (2011). Basics of Space Flight: Black and White Edition. Blüroof Press.

[Durante et al., 2020] Durante, D., Parisi, M., Serra, D., Zannoni, M., Notaro, V., Racioppa, P., Buccino, D., Lari, G., Gomez Casajus, L., Iess, L., et al. (2020). Jupiter's gravity field halfway through the juno mission. Geophysical Research Letters, 47(4):e2019GL086572.

[ESA, 2015] ESA (2015). Network map. [Online; accessed January 26, 2023].

[Fa et al., 2015] Fa, W., Zhu, M.-H., Liu, T., and Plescia, J. B. (2015). Regolith stratigraphy at the chang'e-3 landing site as seen by lunar penetrating radar. Geophysical Research Letters, 42(23):10–179.

[Fan and Qi, 2018] Fan, L. and Qi, G. (2018). Frequency estimator of sinusoid based on interpolation of three dft spectral lines. Signal Processing, 144:52–60.

[Fan et al., 2015] Fan, L., Qi, G., and He, W. (2015). A new frequency estimator of sinusoid based on interpolated fft. In 11th International Conference on Wireless Communications, Networking and Mobile Computing (WiCOM 2015), pages 1–5. IET.

[Fan et al., 2021] Fan, L., Qi, G., Liu, J., Jin, J., Liu, L., and Xing, J. (2021). Frequency estimator of sinusoid by interpolated dft method based on maximum sidelobe decay windows. Signal Processing, 186:108125.

[Forster et al., 2004] Forster, P., Larzabal, P., and Boyer, E. (2004). Threshold performance analysis of maximum likelihood doa estimation. IEEE Transactions on Signal Processing, 52(11):3183–3191.

[Gabor, 1946] Gabor, D. (1946). Theory of communication. part 1: The analysis of information. Journal of the Institution of Electrical Engineers-part III: radio and communication engineering, 93(26):429–441.

[Gardner, 2005] Gardner, F. M. (2005). Phaselock techniques. John Wiley & Sons.

[Gardner et al., 2022] Gardner, T., Cheetham, B., Parker, J., Forsman, A., Kayser, E., Thompson, M., Ott, C., DeMoudt, L., Bolliger, M., Kam, A., et al. (2022). Capstone: A summary of flight operations to date in the cislunar environment.

[Giorgini and Group, 2023] Giorgini, J. and Group, J. S. S. D. (2023). Nasa/jpl horizons on-line ephemeris system.

[Gurfil, 2006] Gurfil, P. (2006). Modern astrodynamics. Elsevier.

[Haan and Ferreira, 2006] Haan, L. and Ferreira, A. (2006). Extreme value theory: an introduction, volume 3. Springer.

[Handel and Zetterberg, 2009] Handel, P. and Zetterberg, P. (2009). Receiver i/q imbalance: Tone test, sensitivity analysis, and the universal software radio peripheral. IEEE Transactions on Instrumentation and Measurement, 59(3):704–714.

[Hitefield et al., 2016] Hitefield, S., Leffke, Z., Fowler, M., and McGwier, R. W. (2016). System overview of the virginia tech ground station. In 2016 IEEE Aerospace Conference, pages 1–13. IEEE.

[Iess, 2012] Iess, L. (27/03/2012). Technical note 3 error budget formulas. Technical report, Università di Roma Sapienza, ALMA Space, British Aerospace, Thales Alenia Space.

[Iess et al., 2014] Iess, L., Di Benedetto, M., James, N., Mercolino, M., Simone, L., and Tortora, P. (2014). Astra: Interdisciplinary study on enhancement of the end-to-end accuracy for spacecraft tracking techniques. Acta Astronautica, 94(2):699–707.

[Iess et al., 2007] Iess, L., Rappaport, N. J., Tortora, P., Lunine, J., Armstrong, J. W., Asmar, S. W., Somenzi, L., and Zingoni, F. (2007). Gravity field and interior of rhea from cassini data analysis. Icarus, 190(2):585–593.

[IFMS, 2010] IFMS, T. (2010). Ifms users' manual.

[Imbriale, 2005] Imbriale, W. A. (2005). Large antennas of the deep space network. John Wiley & Sons.

[Jacobs et al., 2015] Jacobs, C. S., Lead, T., and Kroger, P. (2015). X-band radio source catalog. DSN Telecommunications Link Design Handbook, pages 810–005.

[Jongeling and Navarro, 2019] Jongeling, A. and Navarro, R. (2019). A common platform for dsn receiver development. In 2019 IEEE Aerospace Conference, pages 1–8. IEEE.

[Katayama et al., 1992] Katayama, M., Ogawa, A., and Morinaga, N. (1992). Carrier synchronization under doppler shift of the nongeostationary satellite communication systems. In [Proceedings] Singapore ICCS/ISITA92, pages 466–470. IEEE.

[Kotz and Nadarajah, 2000] Kotz, S. and Nadarajah, S. (2000). Extreme value distributions: theory and applications. world scientific.

[Lehpamer, 2010] Lehpamer, H. (2010). Microwave transmission networks: planning, design, and deployment. McGraw-Hill Education.

[Li et al., 2021] Li, R., Xuan, J., and Shi, T. (2021). Frequency estimation based on symmetric discrete fourier transform. Mechanical Systems and Signal Processing, 160:107911.

[Liu et al., 2022] Liu, N., Fan, L., Wu, H., Jin, J., Xing, J., and Liu, Z. (2022). Dft-based frequency estimation of multiple sinusoids. IEEE Access, 10:40230–40236.

[Lucresi et al., 2016] Lucresi, I., Di Carlofelice, A., and Tognolatti, P. (2016). Sdr-based system for satellite ranging measurements. IEEE Aerospace and Electronic Systems Magazine, 31(1):8–13.

[Maheshwarappa and Bridges, 2014] Maheshwarappa, M. R. and Bridges, C. P. (2014). Software defined radios for small satellites. In 2014 NASA/ESA Conference on Adaptive Hardware and Systems (AHS), pages 172–179. IEEE.

[Mai, 2017] Mai, T. (2017). Space communication and navigation (scan) network sites. [Online; accessed January 26, 2023].

[Malphrus et al., 2018] Malphrus, B., Kruth, J., Pham, T., and Wyatt, E. (2018). Enabling university-operated tracking and communications for deep space smallsat missions. In CubeSat Developers' Workshop, pages 1–21.

[Manghi et al., 2021] Manghi, R. L., Zannoni, M., Tortora, P., Martellucci, A., De Vicente, J., Villalvilla, J., Mercolino, M., Maschwitz, G., and Rose, T. (2021). Performance characterization of esa's tropospheric delay calibration system for advanced radio science experiments. Radio Science, 56(10):1–14.

[Marini, 1971] Marini, J. W. (1971). The effect of satellite spin on two-way doppler rangerate measurements. IEEE Transactions on Aerospace and Electronic Systems, (2):316–320.

[Martellucci, 2012] Martellucci, A. (2012). Galileo reference troposphere model for the user receiver. ESA-APPNG-ReF/00621-AM v2, 7.

[Milani and Gronchi, 2010] Milani, A. and Gronchi, G. (2010). Theory of orbit determination. Cambridge University Press.

[Mladenov et al., 2020] Mladenov, T., Fischer, B., and Evans, D. (2020). Esa's ops-sat mission: Powered by gnu radio. In Proceedings of the GNU Radio Conference, volume 5.

[Modenini and Ripani, 2022] Modenini, A. and Ripani, B. (2022). A tutorial on the tt&c for space missions.

[Montenbruck et al., 2002] Montenbruck, O., Gill, E., and Lutze, F. (2002). Satellite orbits: models, methods, and applications. Appl. Mech. Rev., 55(2):B27–B28.

[Morabito et al., 2003] Morabito, D. D., Shambayati, S., Finley, S., and Fort, D. (2003). The cassini may 2000 solar conjunction. IEEE Transactions on Antennas and Propagation, 51(2):201–219.

[Mou et al., 2021] Mou, Z.-L., Tu, Y.-Q., Chen, P., and Wang, K. (2021). Accurate frequency estimation of multiple complex and real sinusoids based on iterative interpolation. Digital Signal Processing, 117:103173.

[Moyer, 2005] Moyer, T. D. (2005). Formulation for observed and computed values of Deep Space Network data types for navigation. John Wiley & Sons.

[Nakata et al., 2021] Nakata, H., Nozaki, K., Oki, Y., Hosokawa, K., Hashimoto, K. K., Kikuchi, T., Sakai, J., Tomizawa, I., and Saita, S. (2021). Software-defined radio-based hf doppler receiving system. Earth, Planets and Space, 73:1–16.

[NASA/JPL-Caltech/SwRI, 2021] NASA/JPL-Caltech/SwRI (2021). Juno extended mission. [Online; accessed January 28, 2023].

[Notaro et al., 2020] Notaro, V., Iess, L., Armstrong, J. W., and Asmar, S. W. (2020). Reducing doppler noise with multi-station tracking: The cassini test case. Acta Astronautica, 173:45–52.

[Orlati et al., 2016] Orlati, A., Bartolini, M., Buttu, M., Fara, A., Migoni, C., Poppi, S., and Righini, S. (2016). Status report of the srt radiotelescope control software: the discos project. In Software and Cyberinfrastructure for Astronomy IV, volume 9913, pages 388–399. SPIE.

[O'Dea and Kinman, 2019] O'Dea, A. and Kinman, P. (2019). Doppler tracking. In DSN Telecommunications Link Design Handbook, volume 202, pages 810–005. Rev. C. Jet Propulsion Laboratory.

[Perotoni and dos Santos, 2021] Perotoni, M. B. and dos Santos, K. M. (2021). Sdr-based spectrum analyzer based in open-source gnu radio. Journal of Microwaves, Optoelectronics and Electromagnetic Applications, 20:542–555.

[Petrov, 2017] Petrov, L. (2017). Results of the first geodetic vlbi experiment with sardinia station.

[Pham, 2022] Pham, T. e. A. (2022). Radiometric validation of morehead state university ground station. presented at 2022 9th International Workshop on Tracking, Telemetry and Command Systems for Space Applications.

[Pham et al., 2022] Pham, T. T., Malphrus, B., Wyatt, E. J., Kruth, J., Hart, C., and Mattle, E. (2022). Efforts and lessons learned in making the morehead state university's 21-m ground station operational for nasa lunar missions support.

[Prabhu, 2014] Prabhu, K. M. (2014). Window functions and their applications in signal processing. Taylor & Francis.

[Putland and Boashash, 2000] Putland, G. R. and Boashash, B. (2000). Can a signal be both monocomponent and multicomponent? In Third Australasian Workshop on Signal Processing Applications (WoSPA 2000), pages 14–15.

[Quinn, 2009] Quinn, B. G. (2009). Recent advances in rapid frequency estimation. Digital Signal Processing, 19(6):942–948.

[Quinn and Kootsookos, 1994] Quinn, B. G. and Kootsookos, P. J. (1994). Threshold behavior of the maximum likelihood estimator of frequency. IEEE Transactions on Signal Processing, 42(11):3291–3294.

[Rife and Boorstyn, 1974] Rife, D. and Boorstyn, R. (1974). Single tone parameter estimation from discrete-time observations. IEEE Transactions on information theory, 20(5):591–598.

[Riley and Howe, 2008] Riley, W. J. and Howe, D. A. (2008). Handbook of frequency stability analysis.

[Saastamoinen, 1972] Saastamoinen, J. (1972). Atmospheric correction for the troposphere and stratosphere in radio ranging satellites. The use of artificial satellites for geodesy, 15:247–251.

[Sanna et al., 2014] Sanna, G., Buffa, F., Deiana, G. L., and Migoni, C. (2014). Stima speditiva delle coordinate di srt.

[Sansò and Rummel, 1989] Sansò, F. and Rummel, R. (1989). Theory of satellite geodesy and gravity field determination.

[Schutz et al., 2004] Schutz, B., Tapley, B., and Born, G. H. (2004). Statistical orbit determination. Elsevier.

[Serbes, 2018] Serbes, A. (2018). Fast and efficient sinusoidal frequency estimation by using the dft coefficients. IEEE Transactions on Communications, 67(3):2333–2342.

[Serbes, 2021] Serbes, A. (2021). Fast and efficient estimation of frequencies. IEEE Transactions on Communications, 69(6):4054–4066.

[Serbes and Qaraqe, 2022] Serbes, A. and Qaraqe, K. A. (2022). Threshold regions in frequency estimation. IEEE Transactions on Aerospace and Electronic Systems, 58(5):4850–4856.

[Simpson, 1993] Simpson, R. A. (1993). Spacecraft studies of planetary surfaces using bistatic radar. IEEE Transactions on Geoscience and Remote Sensing, 31(2):465–482.

[Simpson et al., 2011] Simpson, R. A., Tyler, G. L., Pätzold, M., Häusler, B., Asmar, S. W., and Sultan-Salem, A. K. (2011). Polarization in bistatic radar probing of planetary surfaces: application to mars express data. Proceedings of the IEEE, 99(5):858–874.

[Simpsona, 2019] Simpsona, C. (2019). Ground station and infrastructure development at the university of alabama, tuscaloosa christopher simpsona, andrew burjeka, william pattona, edward g. hackett jr. b, and charles o'neillc.

[Slobin and Pham, 2010] Slobin, S. D. and Pham, T. (2010). 34-m bwg stations telecommunications interfaces,". DSN Telecommunications Link Design Handbook, pages 810–005.

[Smith et al., 2017] Smith, J., Drain, T., Bhaskaran, S., and Martin-Mur, T. (2017). Monte for orbit determination.

[Smith et al., 1997] Smith, S. W. et al. (1997). The scientist and engineer's guide to digital signal processing.

[So et al., 1999] So, H., Chan, Y., Ma, Q., and Ching, k. P. (1999). Comparison of various periodograms for sinusoid detection and frequency estimation. IEEE Transactions on Aerospace and Electronic Systems, 35(3):945–952.

[Steinhardt and Bretherton, 1985] Steinhardt, A. and Bretherton, C. (1985). Thresholds in frequency estimation. In ICASSP'85. IEEE International Conference on Acoustics, Speech, and Signal Processing, volume 10, pages 1273–1276. IEEE.

[Summers et al., 2018] Summers, T., Schmandt, J., Cheung, E., Gentry, C., and Chen, Y. (2018). Cost effective, flexible ground architecture using software defined radio and gnu radio.

[Tai, 2019] Tai, W. (2019). Dsn frequency transitions from l- to ka-band. unpublished.

[Tapley and Ingram, 1973] Tapley, B. and Ingram, D. (1973). Orbit determination in the presence of unmodeled accelerations. IEEE Transactions on Automatic Control, 18(4):369–373.

[Thompson and Rosen, 2022] Thompson, M. R. and Rosen, M. (2022). Utilization and validation of dss-17 on the capstone lunar mission.

[Thomson et al., 2007] Thomson, F. S., Marouf, E. A., Tyler, G. L., French, R. G., and Rappoport, N. J. (2007). Periodic microstructure in saturn's rings a and b. Geophysical Research Letters, 34(24).

[Thornton and Border, 2003] Thornton, C. L. and Border, J. S. (2003). Radiometric tracking techniques for deep-space navigation. John Wiley & Sons.

[Togni et al., 2021] Togni, A., Zannoni, M., Casajús, L. G., and Tortora, P. (2021). An fft-based method for doppler observables estimation in deep space tracking. In 2021 IEEE 8th International Workshop on Metrology for AeroSpace (MetroAeroSpace), pages 294–299. IEEE.

[Tortora et al., 2004] Tortora, P., Iess, L., Bordi, J., Ekelund, J., and Roth, D. (2004). Precise cassini navigation during solar conjunctions through multifrequency plasma calibrations. Journal of guidance, Control, and Dynamics, 27(2):251–257.

[Tyler et al., 2009] Tyler, G., Linscott, I., Bird, M., Hinson, D., Strobel, D., Pńtzold, M., Summers, M., and Sivaramakrishnan, K. (2009). The new horizons radio science experiment (rex). New Horizons: Reconnaissance of the Pluto-Charon System and the Kuiper Belt, pages 217–259.

[Tyler et al., 1989] Tyler, G., Sweetnam, D., Anderson, J., Borutzki, S., Campbell, J., Eshleman, V., Gresh, D., Gurrola, E., Hinson, D., Kawashima, N., et al. (1989). Voyager radio science observations of neptune and triton. Science, 246(4936):1466–1473.

[Valente et al., 2019] Valente, G., Iacolina, M., Viviano, S., Saba, A., Serra, G., Parca, G., Impresario, G., D'Amore, G., Asmar, S., Montisci, G., et al. (2019). Sardinia deep space antenna: Current program status and results. In Proc. 70th Int. Astron. Congr.(IAC), pages 21–25.

[Valente et al., 2022] Valente, G., Iacolina, M. N., Ghiani, R., Saba, A., Serra, G., Urru, E., Montisci, G., Mulas, S., Asmar, S. W., Pham, T. T., et al. (2022). The sardinia space communication asset: Performance of the sardinia deep space antenna x-band downlink capability. IEEE Access, 10:64525–64534.

[Vallado, 2001] Vallado, D. A. (2001). Fundamentals of astrodynamics and applications, volume 12. Springer Science & Business Media.

[Vallado, 2005] Vallado, D. A. (2005). An analysis of state vector propagation using differing flight dynamics programs. In Paper AAS 05-199 presented at the AAS/AIAA Space Flight Mechanics Conference. Copper Mountain, CO.

[Vetter, 1994] Vetter, J. R. (1994). The evolution of earth gravitational models used in astrodynamics. Johns Hopkins APL Technical Digest, 15(4):319–335.

[Wood, 2008] Wood, L. J. (2008). The evolution of deep space navigation: 1962-1989.